

Synthesis of modified lithium iron phosphate and its electrochemical properties

Jere Leinonen

Master's thesis

Degree program of chemistry

University of Oulu

2023

ABBREVIATIONS

<i>Abbreviation</i>	<i>Meaning</i>
ALD	atomic layer deposition
BMS	battery management system
BOL	beginning of life
CE	coulombic efficiency
CE	counter electrode
C-rate	charging rate
CV	cyclic voltammetry
DOD	depth of discharge
DRC	Democratic Republic of Congo
ECM	equivalent circuit model
EDL	electric double layer
EIS	electrochemical impedance spectroscopy
EOL	end of life
EV	electric vehicle
HCP	hexagonal close-packed
IR-loss	internal resistance induced loss of potential
LCO	LiCoO_2
LCP	LiCoPO_4
LFP	LiFePO_4
LFP/C	carbon coated LiFePO_4
LIB	lithium-ion battery
LMP	LiMnPO_4
LxFP	Li_xFePO_4 , x = doped element
NCA	$\text{LiNi}_x\text{Co}_y\text{Al}_z\text{O}_2$
NMC	$\text{LiNi}_x\text{Mn}_y\text{Co}_z\text{O}_2$
PEG	polyethylene glycol
PVDF	polyvinylidene fluoride
RE	reference electrode
SCE	saturated calomel electrode
SEI	solid electrolyte interface
SOC	state of charge
WE	working electrode
XPS	X-ray photoelectron spectroscopy
XRD	X-ray diffraction

TABLE OF CONTENTS

1 INTRODUCTION	5
2 LITHIUM-ION CELLS AND BATTERIES	6
2.1 General	6
2.2 Lithium-ion cells	7
3 OPERATION OF LITHIUM-ION CELL AND QUALITIES OF GOOD CATHODE	9
3.1 Cell potential, interfaces, electrical double layer, and reaction rate	9
3.2 Lithium iron phosphate and characteristics of a good cathode	13
4 ELECTROCHEMICAL ANALYSIS OF LITHIUM IRON PHOSPHATE	14
4.1 Basic terminology	14
4.2 Nernst equation and Coulombic efficiency	15
4.3 Two-, three- and four-electrode systems	16
4.4 Cyclic voltammetry	18
4.5 Equivalent circuits and electrochemical impedance spectroscopy	21
5 THE OLIVINE CRYSTAL STRUCTURE OF LITHIUM IRON PHOSPHATE	26
5.1 Basic crystal geometry	26
5.2 The crystal structure of lithium iron phosphate	33
6 SYNTHESIS OF DOPED LITHIUM IRON PHOSPHATE	37
6.1 Solid state synthesis	37
6.1.1 Mechano-chemical activation	38
6.1.2 Carbothermal reduction	39
6.1.3 Microwave heating	40
6.2 Solution based synthesis	41
6.2.1 Hydrothermal synthesis	41
6.2.2 Sol-gel synthesis	42
6.2.3 Spray pyrolysis and spray technologies	43
6.2.4 Co-precipitation	44
6.3 Novel and rare synthesis methods	44
7 DOPING LITHIUM IRON PHOSPHATE	45
7.1 Introduction to doping and modifications	45
7.2 Alkali metal doping	48
7.2.1 Sodium	48
7.2.2 Potassium	49
7.3 Alkaline metal doping	50
7.3.1 Magnesium	50
7.3.2 Calcium	50

7.4 Transition metal doping	51
7.4.1 Titanium	51
7.4.2 Vanadium	53
7.4.3 Chromium	54
7.4.4 Manganese	54
7.4.5 Cobalt	55
7.4.6 Nickel	56
7.4.7 Copper	57
7.4.8 Zinc	57
7.4.9 Niobium	57
7.4.10 Molybdenum	58
7.4.11 Ruthenium	58
7.4.12 Rhodium	59
7.4.13 Palladium	59
7.4.14 Tungsten	59
7.5 Post-transition metals	60
7.5.1 Aluminium	60
7.5.2 Indium	60
7.5.3 Tin	61
7.6 Metalloid doping	62
7.6.1 Boron	62
7.6.2 Silicon	62
7.6.3 Antimony	62
7.7 Nonmetal and halogen doping	63
7.7.1 Sulfur	63
7.7.2 Fluoride	63
7.7.4 Bromide	63
7.8 Rare earth element doping	64
7.8.1 Yttrium	64
7.8.2 Lanthanum	64
7.8.3 Cerium	64
7.8.4 Neodymium	65
7.8.5 Samarium	65
7.8.6 Europium	66
7.8.7 Gadolinium	66
7.8.8 Dysprosium	66

7.8.9 Holmium	66
7.8.10 Erbium	67
7.8.11 Ytterbium	67
7.9 Co-doping	68
7.9.1 Cerium and lanthanum	68
7.9.2 Niobium and titanium	68
7.9.3 Fluorine and vanadium.....	68
7.9.4 Cobalt and zirconium	69
7.9.5 Sodium and chlorine.....	69
8 WHICH DOPANTS ARE THE BEST?	70
9 SUMMARY	77
10 REFERENCES	78

1 INTRODUCTION

Lithium-ion batteries (LIBs) are used to power portable electronic devices and electric vehicles (EVs). Cobalt has been an essential element on popular cathode active materials of LIBs since the commercialization of LiCoO_2 (LCO) by Sony in 1991.^{1,2} However, most cobalt reserves and processing facilities are in Democratic Republic of Congo (DRC) and China. This creates geopolitical risks and restricts supply expansion. On top of that, child labour is used to mine cobalt in DRC. Consequently, cobalt free and low-cobalt materials should be and are developed and used for commercial applications. One of the common cobalt free materials used today is lithium iron phosphate,¹ also known as LiFePO_4 (LFP). LFP was identified as a cathode material for LIBs by Padhi, Nanjundaswamy, and Goodenough in 1997.³ Main advantages of LFP are its flat voltage profile, low cost, abundant material supply,⁴ environmental friendliness (nontoxic and cobalt free),³ and thermal stability.⁵ The downsides include relatively low theoretical capacity, low energy density, low electronic conductivity, and low ionic diffusivity.⁴

This study focuses on synthesis of modified LFP and its electrochemical properties. Common and novel synthesis methods are reviewed shortly. Especially, performance increasing modifications are reviewed. These include coating, control of particle size and particle morphology, and doping in which ions are used to replace atoms in LFP.⁶ Effects of the modifications are discussed through the paper with most time spent on doping and comparison of the effects induced by doping with different elements. In the end the dopants are ranked according to their effects on performance, price, and sustainability of a battery.

To understand the modifications and their effect on electrochemical performance the structure of the material must be studied and understood. Because of this a chapter to crystallography and structure of LFP is included. Similarly, some basic information about common electrochemical characterization techniques is included to help the reader understand the plots and values produced by them. These include cyclic voltammetry (CV), electrochemical impedance spectroscopy (EIS), electrode setups, and terminology.

2 LITHIUM-ION CELLS AND BATTERIES

2.1 General

In this Chapter, the different parts of batteries and cells and chemical and physical phenomena inside LIBs are reviewed.

A **cell** is the basic electrochemical unit. In a cell, **chemical energy is converted into electrical energy** making cell provide electricity. The cell consists of **electrodes, electrolyte, separators, container, and current collectors** (terminals). A **battery** on the other hand consists of one or more electrochemical cells in series/parallel, monitors, controls, and other ancillary components. Electrochemical cells/batteries can be identified either as **primary** (nonchargeable) or **secondary** (rechargeable).⁷

Anode also known as **negative electrode** is the electrode, which gives up electrons to the external circuit and is **oxidized** during cell discharge. **Cathode** also known as **positive electrode** is the **electrode**, which accepts electrons from the external circuit and is reduced during cell discharge. The **electrolyte**, also known as ionic conductor, provides medium for transfer of charge as ions inside the cell from cathode to anode. The electrolyte is usually liquid with dissolved salts, alkalis, or acids to provide ionic conductivity. The anode and cathode are separated from each other mechanically with **separator**. The separator is permeable by the electrolyte to maintain the ionic conductivity but prevents short-circuits as it doesn't pass electrons through, thus making the electrodes electronically separated.⁷ Common materials for LIBs are listed on Table 1 below.

Table 1. The most common materials used in LIB cells.

LIB cell component	Common materials	Ref
Cathode	LiCoO ₂ , LiFePO ₄ , LiNi _x Co _y Mn _z O ₂ , LiMn ₂ O ₄	8
Anode	graphite	8
Electrolyte solvent	ethylene carbonate, dimethyl carbonate	8
Electrolyte salt	LiPF ₆ , LiBF ₄	8,9
Cathode current collector	aluminum foil	9
Anode current collector	copper foil	9
Separator	polyethylene, polypropylene	10

2.2 Lithium-ion cells

Lithium-ion cells and batteries come in different shapes and sizes. Common shapes include cylindrical, prismatic, pouch, and coin.^{7,11} In Figure 1 a cylindrical cell is shown.

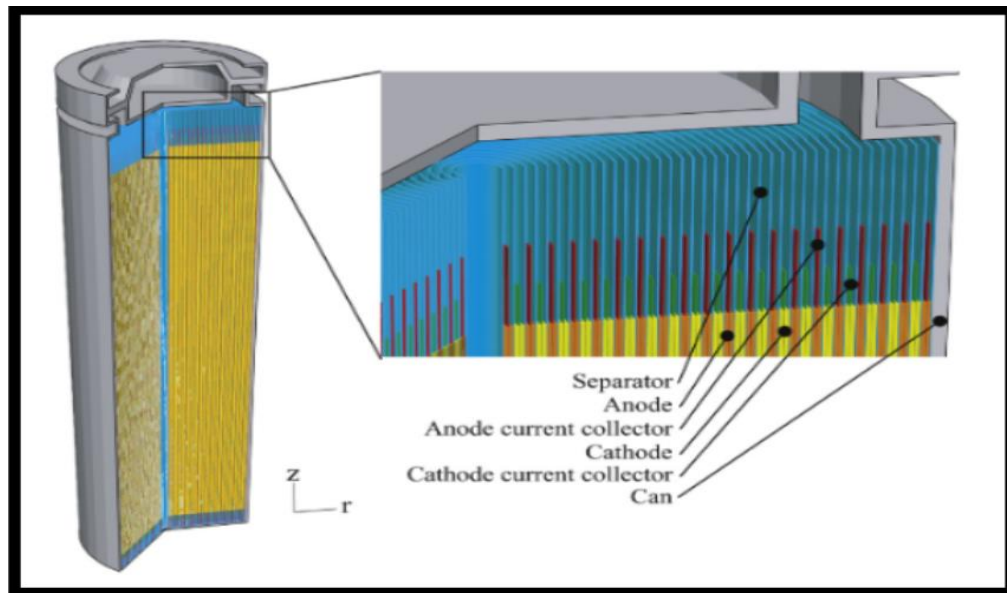


Figure 1. Illustration of cylindrical LIB by Jeon *et al.* reprinted with permission from ELSEVIER BV.¹²

Coin cells as shown in Figure 2 are commonly used in academic research as machine-made cells are produced in large patches which doesn't make sense for research.¹¹

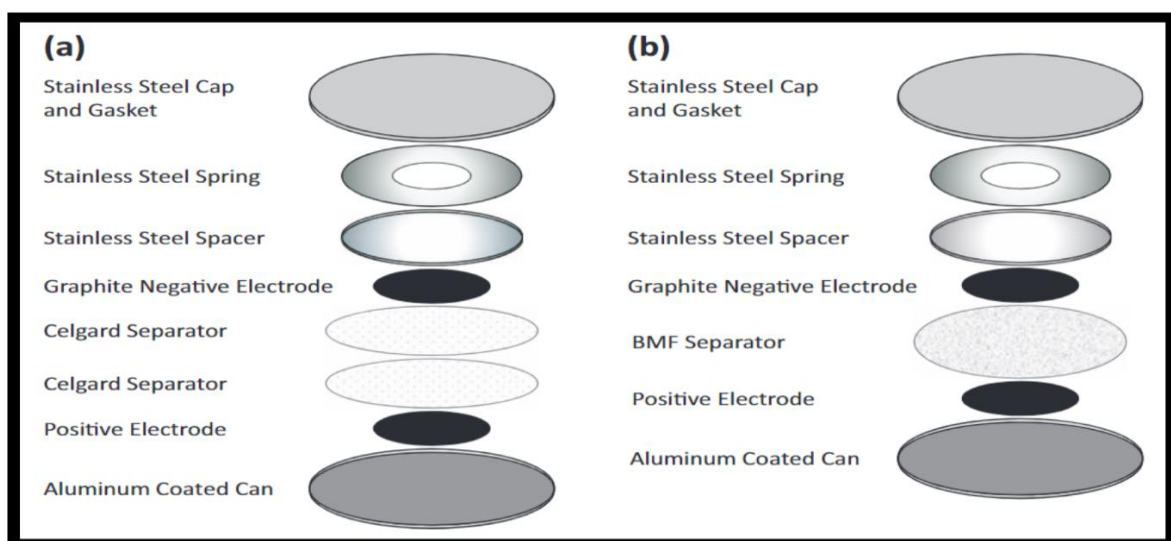


Figure 2. Parts of full cell coin cell with A) Two Celgard separators and B) with BMF separator as illustrated by Murray *et al.*¹¹

When cathodes are prepared in laboratory or for commercial applications other materials than the active materials are added. Common additives include **binder** such as polyvinylidene fluoride (PVDF) and different **conductive carbon** materials.¹⁰ The electrode preparation process is important for the performance of the cell. Modern electrode preparation methods such as 3D printing (Figure 3) are studied in research.¹³

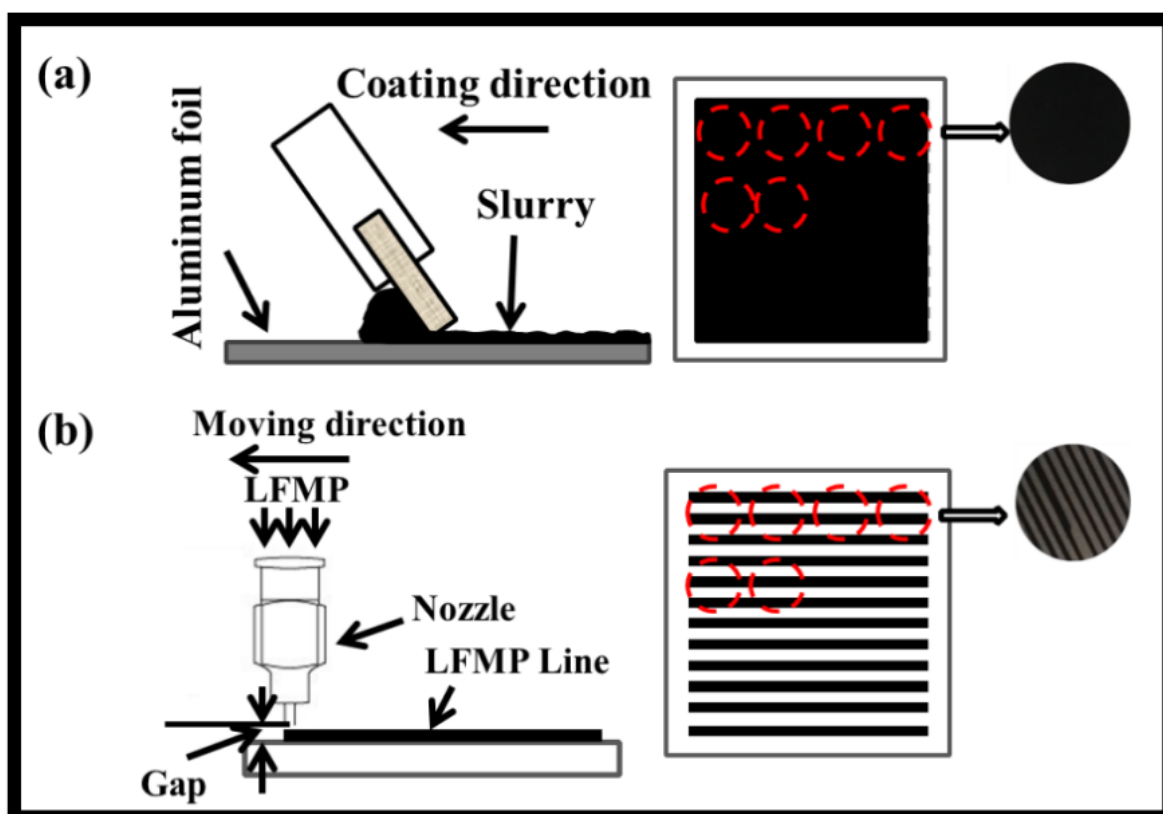


Figure 3. (a) Traditional electrode preparation process and (b) 3D printing electrode preparation as illustrated by Hu *et al.* reprinted with permission from John Wiley and Sons - Books.¹³

Although this study focuses on cathode, all the other parts of the battery or cell affect the overall performance. Many phenomena that doping may or may not affect, such as solid electrolyte interface (SEI) formation and possible electrolyte decomposition under higher operating voltages¹⁴ are not discussed in this paper but should be kept in mind.

3 OPERATION OF LITHIUM-ION CELL AND QUALITIES OF GOOD CATHODE

3.1 Cell potential, interfaces, electrical double layer, and reaction rate

Electric potential difference called **cell potential** exists between anode and cathode. It can be measured with high impedance voltmeter. Cell potential is the energy available to drive charge externally from one electrode to another. Inside the cell the potential transitions between phases occur almost entirely on the interfaces. The interphases have effect on the charge carriers in the cell and the magnitude of potential difference at the interface controls the direction and **rate of charge transfer**.¹⁵

Electrochemical reaction is heterogenic meaning it occurs on an interface between two phases, the electrode surface, and the electrolyte solution. In the bulk solution electroneutrality rule applies unlike close to the electrode surface where adsorption of ions or dipole molecules generates charge. This excess charge forms an electric field. The region where these charges are is called the **electric double layer (EDL)**. The double layer is also on the outer electrode surface as it also has electron deficiency or electron excess compared to the inner electrode. The EDL can be divided to inner Helmholtz layer (x_1) and outer Helmholtz layer (x_2). x marks the distance from the electrode surface to the layer. The inner Helmholtz layer consist of desolvated molecules or ions **specifically adsorbed** to the electrode surface. Specifically bound species have both electrostatic and chemical interaction with the surface. The solvated molecules forming the outer Helmholtz layer can't go as near the electrode surface because of the water molecules surrounding them. **Diffuse layer** forms after the outer Helmholtz layer. There subspecies move according to thermal motion and weakening electrostatic interaction.¹⁶

Total capacitance (C_{tdl}) of the layers can be calculated from experimental data. The solution is thought as dielectric medium which has a relative permittivity and this way the layers can be thought as similar to capacitors. The Helmholtz layers are thought as one layer called the inner layer that has capacitance (C_2). The diffusion layer has capacitance (C_d). The inner layer capacitance is thought to be connected in series with diffusion layer capacitance and together they form capacitance (C_{dl}). The specifically bound ions also contribute to capacitance (C^q) and are thought to be connected parallel with (C_{dl}).¹⁶

Equations (1) and (2) can be derived for C_{dl} and C_{tdl} .

$$\frac{1}{C_{dl}} = \left(\frac{\partial \sigma^m}{\partial \phi_0} \right)^{-1} = \frac{1}{C_2} + \frac{1}{C_d} = \left(\frac{x_2}{\epsilon_r \epsilon_0} \right) + \left(\frac{1}{(2\epsilon_r \epsilon_0 z^2 F^2) \cosh(zF\phi_2/2RT)} \right) \quad (1)$$

$$C_{tdl} = - \left(\frac{\partial q_d}{\partial \phi_0} \right) - \left(\frac{\partial q'}{\partial \phi_0} \right) = C_{dl} + C_{q'} \quad (2)$$

The total capacitance depends on the relative permittivity of the Helmholtz layer (ϵ_r), bulk solutions relative permittivity (ϵ_{rb}), bulk solutions concentration of ions (c_b), the distance from the electrode, the charge of the ions (z), and the potential on electrode surface (ϕ_0) which affects the potential on outer Helmholtz layer (ϕ_2). (q') is the inner layer charge and (q_d) is the diffuse layer charge. (F) is the Faraday constant (96485 C/mol), σ^m is the charge of the electrode, and (ϵ_0) is the permittivity of vacuum ($8.854 \cdot 10^{-12}$ F/m).¹⁶ EDL can be described with capacitors as shown in Figure 4.

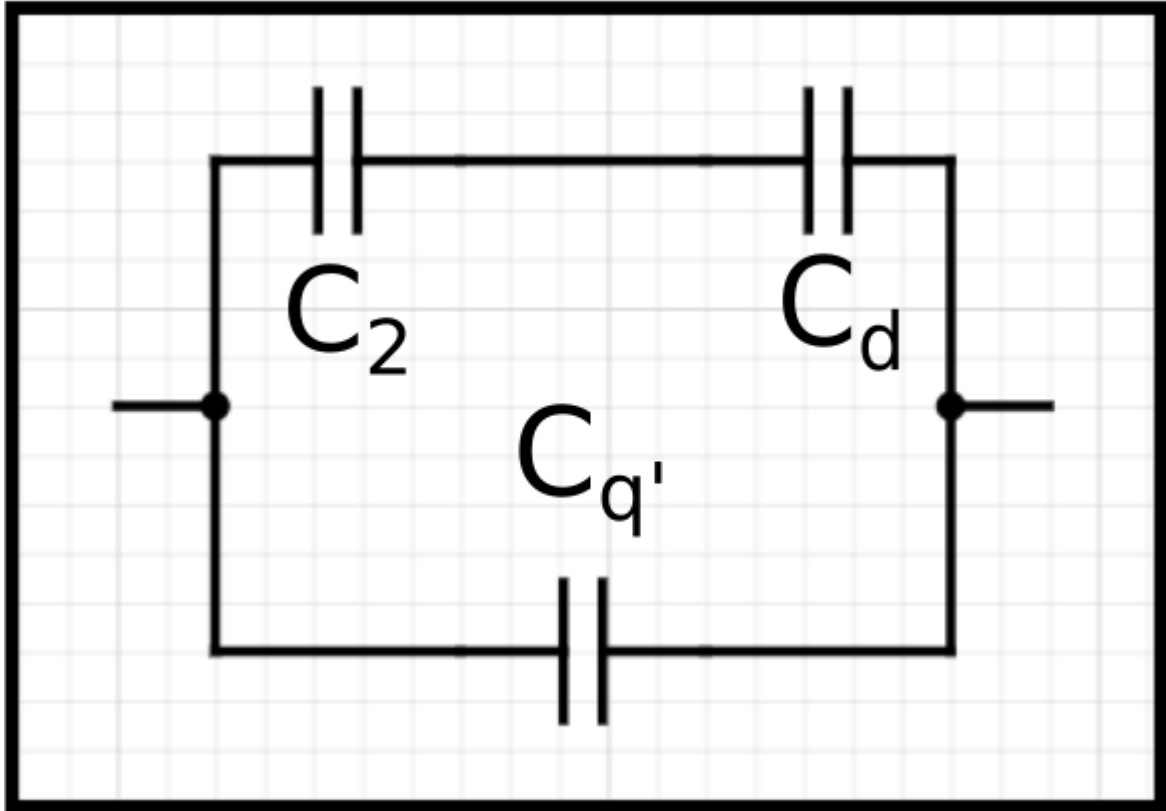


Figure 4. EDL equivalent circuit where C_2 is the inner layer capacitance, C_d is the diffusion layer capacitance, and $C_{q'}$ is the capacitance formed by specifically bound ions. This circuit could also be described as single capacitor C_{tdl} .

Figure 5 shows processes affecting general electrode reaction where (O) is reduced to (R) with (n) moles of electrons (e). Reaction speed is affected by the cell potential as the electron transfer (reaction 4 in Figure 4) at electrode surface and adsorption (reaction 3 in Figure 4) depend on potential. Higher cell potential should result in higher reaction speed. Chemical reactions' reaction speed depends on concentration of reactants, temperature, surface area and other factors. Mass transfer (reaction 1 in Figure 4) can be divided into **migration**, **convection**, and **diffusion**. Diffusion is the movement of a species that is affected by a gradient of **chemical potential** (concentration gradient).¹⁵

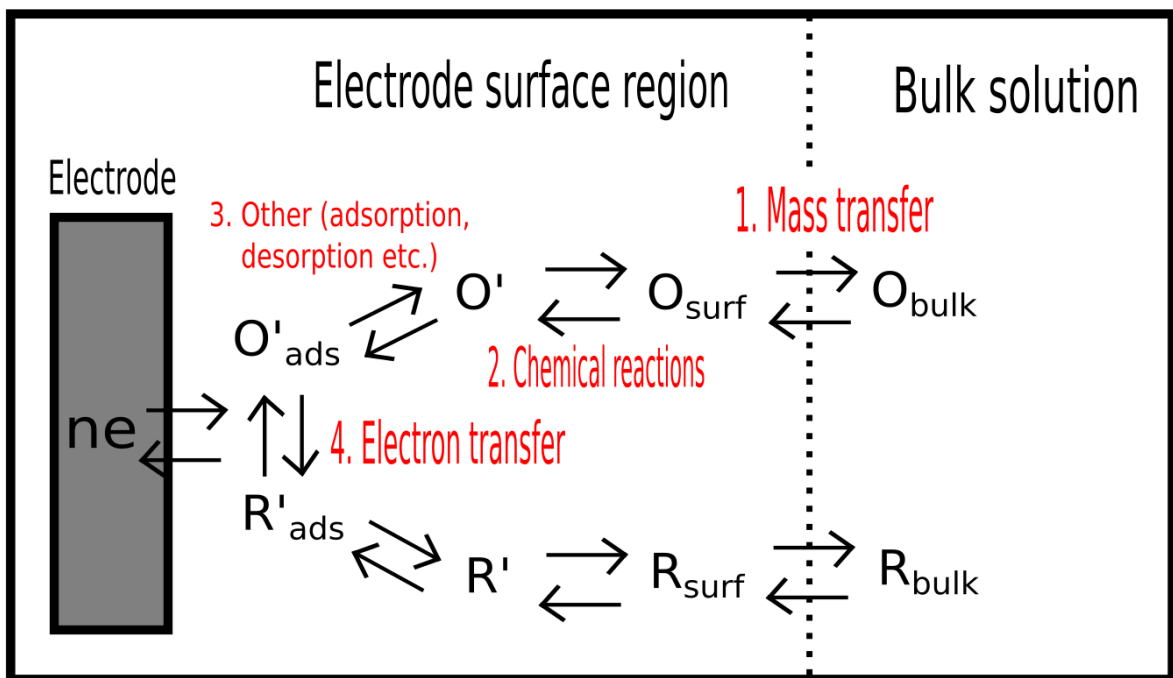


Figure 5. Different processes affecting the overall reaction speed of electrode reaction. Drawn by Jere Leinonen as shown in *Electrochemical methods* by Barry and Faulkner.¹⁵

The reaction rate of an electrode reaction can be described with Equation 3:

$$Rate = \frac{i}{nFA} = \frac{j}{nF}, \quad (3)$$

where (i) is the current, (n) is the stoichiometric number of electrons consumed in electrode reaction, (F) is the faraday constant, (A) is the area of the electrode, and (j) is current density.¹⁵ We can see that the reaction rate depends on current which can be described with Equation 4, also known as Ohm's law:

$$I = \frac{\phi}{R}, \quad (4)$$

where (I) is current, (ϕ) is potential, and (R) is resistance.¹⁷ The resistance of electrode reaction can be described with a series of resistances each associated with the component reactions discussed before.

The equilibrium potential (E_{eq}) of the cell is the potential when net current is zero. When electrode or cell potential (E) is different from equilibrium value, the electrode or cell is said to be **polarized**. **Overpotential (η)** is the measure of polarization and can be described with Equation 5,¹⁵

$$\eta = E - E_{eq}. \quad (5)$$

Overpotential drives the values of current density. The overpotential of electrode reaction can be described as a sum of component overpotentials associated with each reaction step (Figure 6). The reaction rate and the resistances correlate. The reaction rate will increase if resistance or impedance is lowered, and the reaction rate will go down if resistance or impedance is increased.¹⁵ Polarization is something to avoid when designing electrodes. **Ideal nonpolarizable electrode** would have reaction rate of infinity and no potential losses.¹⁶

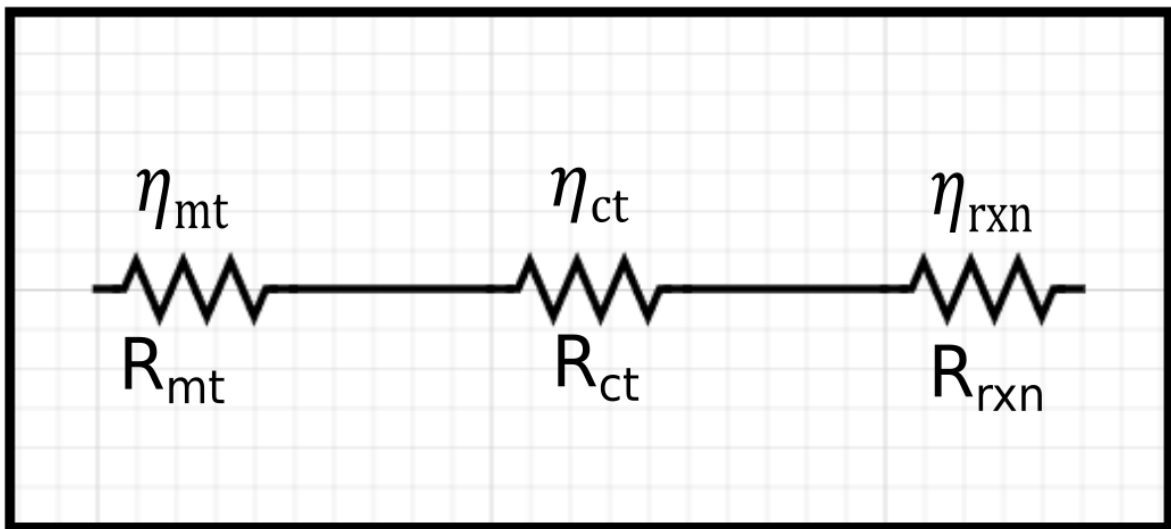


Figure 6. Resistances of mass-transfer (R_{mt}), charge-transfer (R_{ct}), preceding reaction resistance (R_{rxn}), and the associated overpotentials.¹⁵

3.2 Lithium iron phosphate and characteristics of a good cathode

The goal in lithium-ion battery cathode research is to find material that is **safe, easy to synthesize**, and **low cost** that also has **long cycle life, high energy density, high capacity**, and **high power density**. Long cycle life means that the cathode material is stable when lithium ions are intercalated and deintercalated repeatedly. High energy density means that the cathode material has high capacity and high potential with reference to Li/Li⁺ (lithium metal) reference electrode.¹⁸ This comes from the fact that **electric potential is the energy per unit charge**. This can be described with Equation 6.

$$\varphi = \frac{U}{q_0}, \quad (6)$$

where φ is potential [V], U is potential energy [J], and q_0 is (test) charge [C].¹⁷

High capacity means that the cathode can host high amount of lithium ions in a way that they can also be electrochemically removed from the structure reversibly. High power density means that the cathode material has a lot of power per volume.¹⁸ Now, power is the rate at which work is done. This means that high power density material is a material that can output high amount of work in short period of time. The work is done by the electric field that exerts a force to a charged particle in the electric field. This work can always be expressed in terms of electric potential energy.¹⁷ However, average voltage can also be expressed via average (output) voltage and average (output) current if either voltage or current is constant as shown by Equation 7.

$$P_{D(average)} = \frac{P_{av}}{V} = \frac{\Delta W}{Vt} = \frac{-\Delta U}{Vt} = \frac{I_o \varphi_o}{V}, \quad (7)$$

where $P_{D(average)}$ is the average power density [Wh/L] (commonly used unit with batteries), V is the volume of the electrode [m³], ΔW [J] is the work done by the electric field in time t [h], ΔU is the change in potential energy [J], I_o is the average output current [A], and φ_o is the average output potential [V].¹⁹ To achieve high power density the cathode material must have **high electronic conductivity** and **high lithium diffusion coefficient** which contribute to **high rate capacity** (current).¹⁸

4 ELECTROCHEMICAL ANALYSIS OF LITHIUM IRON PHOSPHATE

4.1 Basic terminology

To understand the electrochemical analysis methods we need to first know some fundamental concepts about electrochemistry and electromagnetism. We also need to know some terminology to know what is being talked about in the research papers. This chapter is dedicated to these basics.

State of Charge (SOC) is the battery capacity as a percentage of maximum capacity at a certain point. **C-rate** is the rate at which battery can charge or discharge from all of its energy or power. 1C-rate would mean that battery is recharged or discharged in 1h. If C-rate goes up the charge and discharge rate go up, for example 2C would mean that a battery is charged or discharged in 60 min / $2C = 30$ min. A 0.5C charge rate would mean a charging time of 60 min / $0.5 C = 120$ min. **A cycle** is process of discharging and charging a battery once. A cycle can be full or partial depending on application. **Beginning of Life (BOL)** values refer to the battery values when the battery is built and **end of life values (EOL)** refer to values when the maximum power and energy values have dropped to unsatisfactory levels for the consumer.²⁰ **Irreversible capacity** is the capacity lost during cycling of electrochemical cell and the main cause of this capacity loss is the SEI layer formation in LIBs which consumes Li^+ .²¹ Irreversible capacity losses are known as **capacity fade** and reversible capacity loss is known as **self-discharge**.²² **Depth of discharge (DOD)** is the percentage of the capacity that has been discharged from the maximum capacity. DOD can be thought as the percentage of the total energy that is cycled from the battery. Lowering DOD usually achieves greater cycle life and improves safety. **Specific energy (gravimetric energy density)**, defines battery capacity in weight (Wh/kg). **Volumetric energy density** defines battery capacity in volume (Wh/dm³). **Battery management system (BMS)** is the control system managing battery packs charging, discharging, temperature, balancing of the cells, and communications for example in an EV.²⁰

4.2 Nernst equation and Coulombic efficiency

Nernst equation (Equation 8) is maybe the most important equation in electrochemistry and can be written as

$$E_{cell} = E_{cell}^0 - \frac{RT}{nF} \ln K. \quad (8)$$

where F is the faraday constant (96485 C/mol),³⁰ R is the gas constant (8.314 J/K·mol),³⁰ n is the number of moles of electrons moved in the reaction,³⁰ T is temperature [K], E_{cell} is the cell potential [V] determined by the free energy of the cell reaction: $E_{cell} = -\Delta G/nF$,³⁰ K is the equilibrium constant determined by the activities (a_x) or the partial pressures (p_x) of the compounds involved in the cell reaction (Equation 9). This can be written as

$$K = \frac{a_{products} \text{ or } p_{products}}{a_{starting materials} \text{ or } p_{starting materials}}. \quad (9)$$

In ideal solutions concentrations can be used, and E_{cell}^0 is the standard cell potential [V],²³ determined by the standard free energy of the reaction: ΔG^0 .¹⁵ E_{cell}^0 can be calculated by summing the standard electrode potentials of the cell. Nernst equation is needed to understand any electrochemical system or analysis method. Nernst equation shows the connection between the activity, or concentration, of the ions and the cell potential.²⁴

Another important concept is **Coulombic efficiency (CE)** defined as the discharge capacity over charge capacity of a specific electrode:

$$CE = \frac{\text{Discharge capacity}}{\text{Charge capacity}} = \quad (10)$$

$$\frac{\text{Total number of Li}^+ \text{ back to cathode}}{\text{Total number of Li}^+ \text{ departing from cathode}} = \quad (11)$$

$$\frac{\text{Total number of e}^- \text{ back to cathode}}{\text{Total number of e}^- \text{ departing from cathode}} \quad (12)$$

In an ideal cell, where no side reactions happen, the flow of Li^+ or electrons is completely reversible and $CE = 100\%$. This of course doesn't happen in a real cell. If the side reaction is chemical then the electron loss and acceptance still happen on the electrode but are irreversible (e.g. electrolyte decomposition). If the side reaction are electrochemical then the electrons of the reactions may end up in the current collectors depending of reaction pathways. CE goes down in the first initial

cycles as electrons go to irreversible SEI layer formation after which CE stabilizes. The remaining capacity in a cell can be calculated as

$$\text{Capacity retention} = (CE)^n. \quad (13)$$

where n is the cycle number. This equation works reasonably well for LIBs, but not for other technologies.²⁵

4.3 Two-, three- and four-electrode systems

Three-electrode system (Figure 7) consists of **working electrode (WE)**, **reference electrode (RE)**, **counter electrode (CE)**, and **potentiostat**. Three-electrode system is used to measure the potential on just one half of the cell independently of the other. The reaction of interest happens on the WE and the other half-reaction happens on CE which allows current flow. RE acts as a stable reference point for voltage measurement between WE and RE. WE is made of known material with known geometry. Typical CE materials include platinum and graphite. Sometimes CE is called auxiliary electrode. Potentiostat can change or keep the voltage between WE and RE constant by adjusting the current flowing through CE to WE. It's also used to measure the voltage between WE and RE.^{15,16,24}

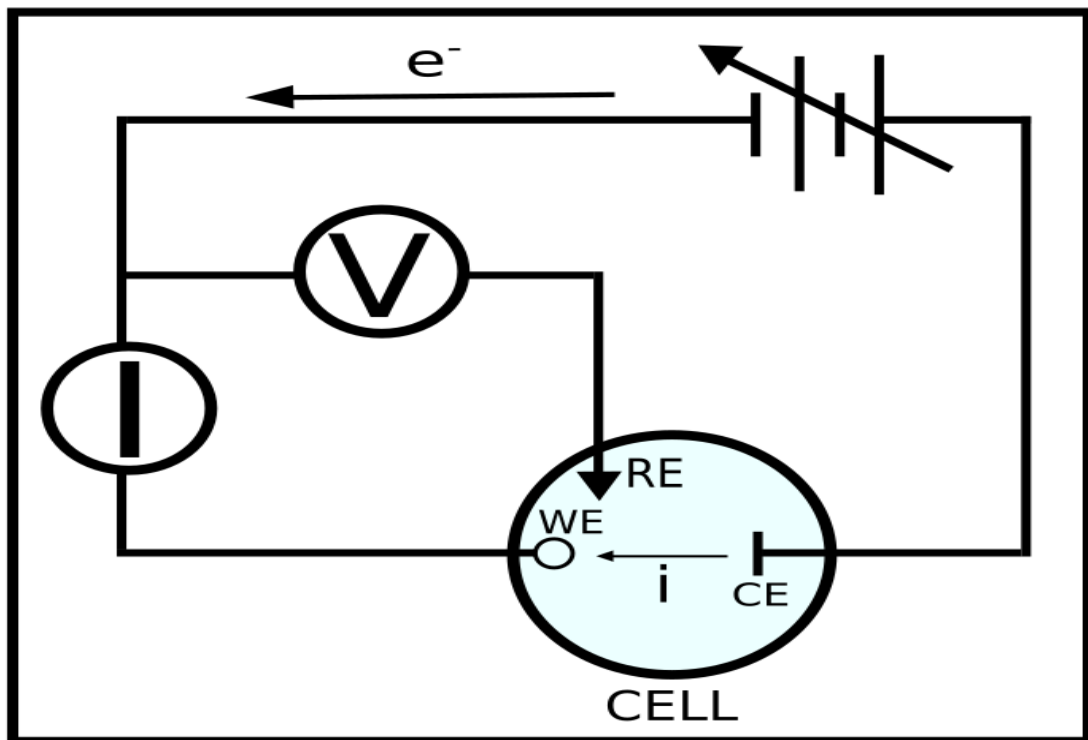


Figure 7. Simplified circuit diagram for three-electrode setup drawn by Jere Leinonen.

The potential in RE should not ideally change even if small current were to flow through electrode-electrolyte interphase. This kind of electrode is called **non-polarizable electrode**. There is no real electrodes that are truly non-polarizable but the most common **silver chloride electrode (Ag/AgCl)** and the **saturated calomel electrode (SCE)** come very close.²⁴ Ideally no current flows through RE,¹⁶ but in real system negligible current flows through RE. The very small current is achieved by having voltage meter (potentiostat) with large impedance.¹⁵ RE is kept close to WE to avoid **internal resistance induced loss of potential (IR-loss)**. The IR-loss occurs because the electrolyte solution has its own resistance. By keeping RE and WE close IR-loss is smaller and the voltage measured between RE and WE depends solely on the potential difference of the electrodes.^{16,24} Three-electrode system is used in cyclic voltammetry and electrical impedance spectroscopy.^{26,27}

In the simpler **two-electrode system** the RE works also as CE. This leads to current flowing through the RE which then affects the concentrations of ions and in the end the electrode potential. This is a problem especially in large scale electrolysis or quick voltammetry in organic solvents. The voltage measured in two-electrode setup is the **complete voltage dropped across the whole cell**. This includes the IR-losses of the electrolyte which have to be taken into account.¹⁶

4.4 Cyclic voltammetry

In cyclic voltammetry (CV) **excitation signal** is applied between working electrode and reference electrode. This excitation signal is linear potential scan with a **triangular waveform** (Figure 8).^{23,27} Other types of waveforms can also be used.

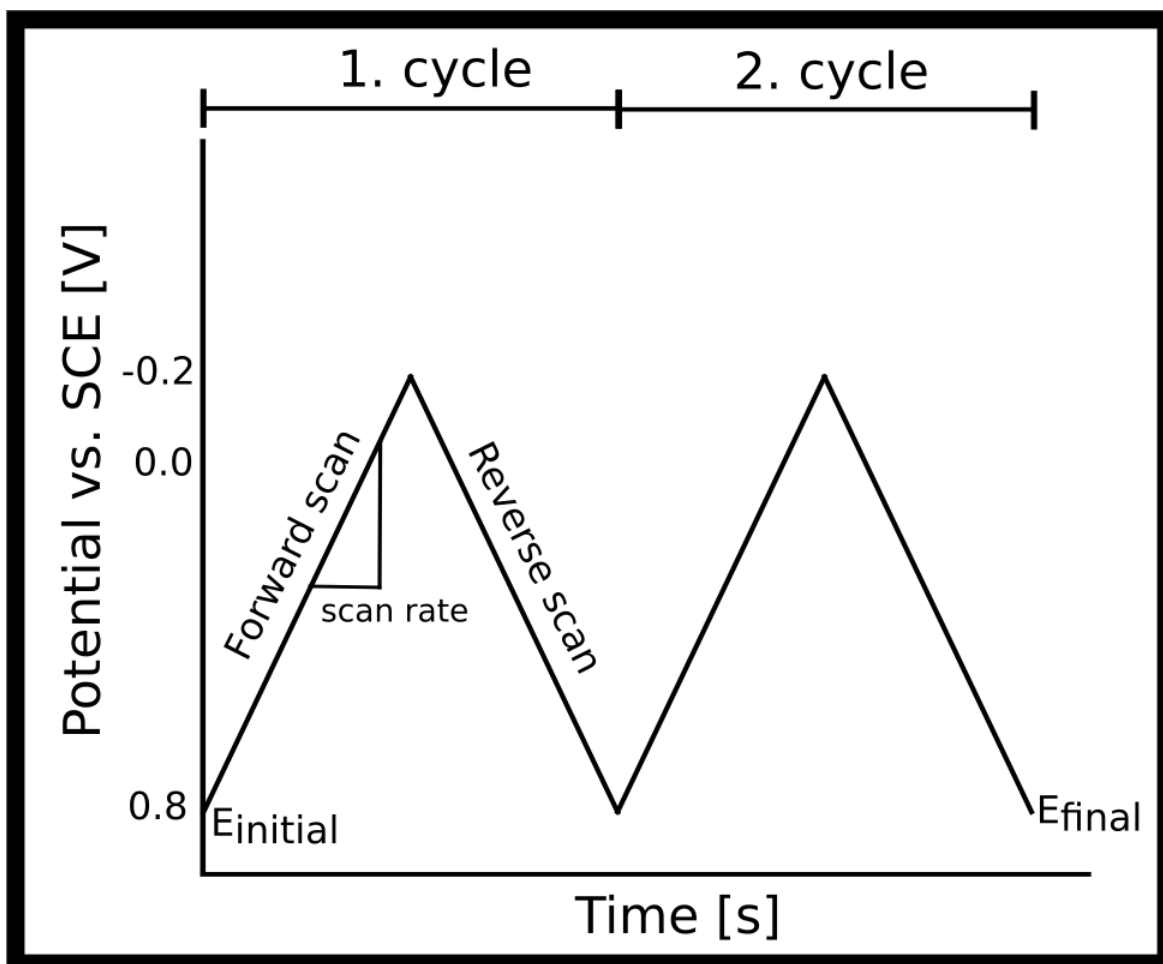


Figure 8. The triangular waveform commonly used in CV. Drawn by Jere Leinonen as depicted by Kissinger and Heineman.²⁷

This signal is produced by cycling the potential of the WE which is immersed in the unstirred solution of a three-electrode system. The potential is oscillated between two values sometimes called **switching potentials** one or more times.⁴² The slope of the waveform is the **scanrate** at which the potential is changed. Switching potentials are chosen so that diffusion-controlled oxidation or reduction of one or more analytes occurs.²³ The scan in which the value of potential goes down is called the **forward scan** and the scan where the value of potential goes up is called **reverse scan**. A **cyclic voltammogram** (Figure 13) is produced by measuring the **response signal** which is the current at the WE during the scan. In the

voltammogram x-axis is the potential, which can be also thought as a time axis as the potential changes with time. Y-axis is the current.²⁷

In a typical cyclic voltammogram (Figure 9) the **initial potential** is chosen so that the compound of interest doesn't go through electrolysis. During the forward scan the potential goes down and at some point the potential is low enough to start reducing the compound of interest. This reduction means that electrons start flowing and a current called **cathodic current** is measured, which can be seen as a peak in the voltammogram.

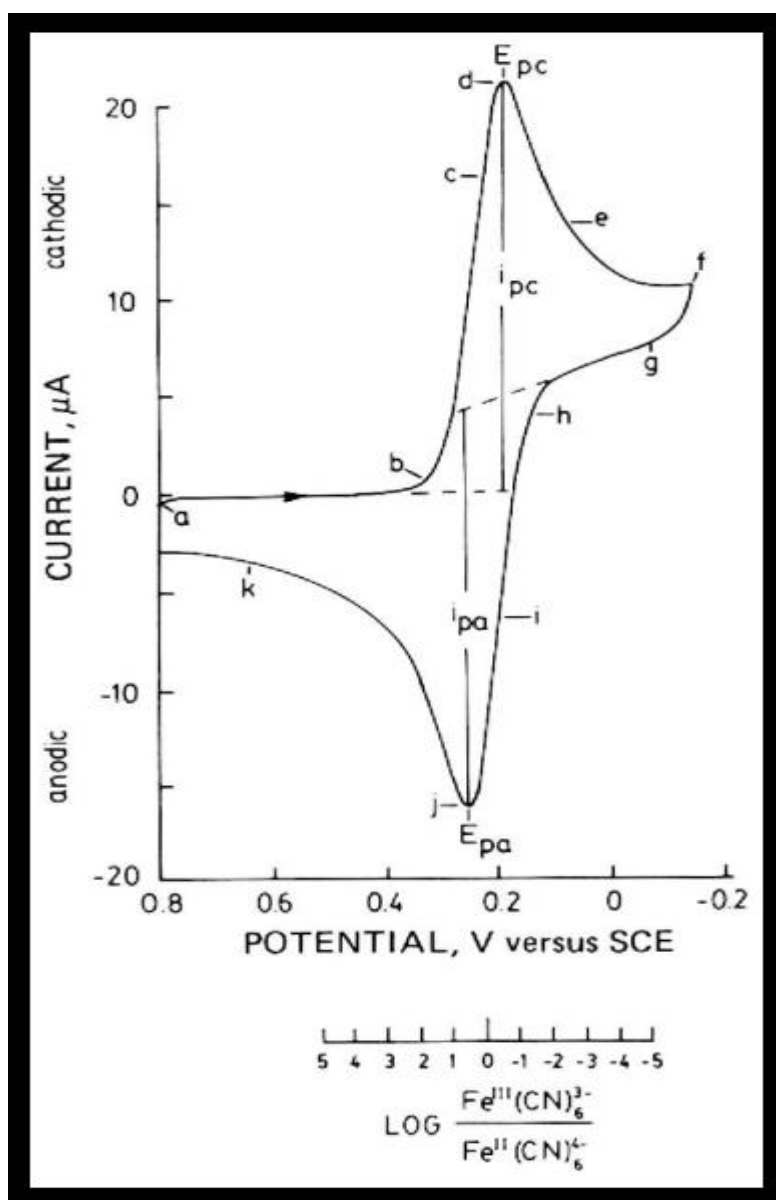


Figure 9. Voltammogram by Kissinger and Heineman reprinted with permission from American Chemical Society.²⁷

This peak forms because at some point the current has its maximum value as the amount of the non-reduced compound goes down on the electrode surface and in the solution around it and thus the current will go down also. Then the scan direction is switched. During the start of this **reverse scan** the potential is still negative enough to produce cathodic current and reduce the compound. When the electrodes potential is positive enough it starts to oxidize the just reduced compound of interest. This causes **anodic current** which rapidly increases until there is no more of the compound to be oxidized after which the negative current starts to decay. To satisfy the Nernst equation (12) the redox-reaction has to happen. The big change in current in the diagram is explained by the logarithmic relation between E_{cell} and $K = \ln(a_{\text{products}})/(a_{\text{startingmaterials}})$. At one point between the peaks the concentrations or the activities of the compound of interest equal each other and then $\ln(a_{\text{products}})/(a_{\text{startingmaterials}}) = 1$.²⁷

The important parameters of CV are the sizes of **anodic peak current (i_{pa})**, **cathodic peak current (i_{pc})**, **anodic peak potential (E_{pa})**, and **cathodic peak potential (E_{pc})**. The i_p values can be extrapolated from the curve as in Figure 9. In a **electrochemically reversible couple** both species (oxidizing and reducing species) rapidly exchange electrons with the working electrode. In this kind of a couple, the **formal reduction potential ($E^{\circ'}$)** is centered between E_{pa} and E_{pc} :

$$E^{\circ'} = \frac{E_{pa} + E_{pc}}{2} . \quad (14)$$

The number of electron transferred in the reaction (n) can also be determined from the distance between peak potentials:

$$\Delta E_p = E_{pa} - E_{pc} \cong \frac{0.059}{n} . \quad (15)$$

If the electron transfer is slow its considered a sign of “irreversibility” and this causes the peak separation to increase. **Electrochemical irreversibility** is caused by slow electron change of the redox species with the working electrode. When this happens equations (13) and (14) cannot be used. **Coupled chemical reactions** have effect on the shape of the diagram. It means that the diagram may have multiple peaks associated with the reactions happening to the initially reduced compound. This is common with LFP that is doped. CV requires **waveform generator** for producing the excitation signal, a **potentiostat** to apply the signal to the cell, a **current-to-**

voltage converter to measure the current, and an **oscilloscope** to display the voltammogram.²⁷ In the studies electrochemical workstations were used for CV.

4.5 Equivalent circuits and electrochemical impedance spectroscopy

Equivalent circuits can be used to simplify circuits,¹⁷ show parasitic non-idealistic effects happening in real circuit elements,¹⁹ and to describe physical phenomena in cells. The equivalent circuit models (ECMs) are used by BMS software to estimate battery pack information and detect failures in the battery pack by comparing the model values to the measured values. Researchers use ECMs for electrochemical measurements such as electrochemical impedance spectroscopy. ECMs are built on based on the understanding of physical phenomena happening in the cell.²⁸ One of the most common equivalent circuits used for electrochemical cells is the **Randles equivalent circuit** (Figure 10).¹⁵

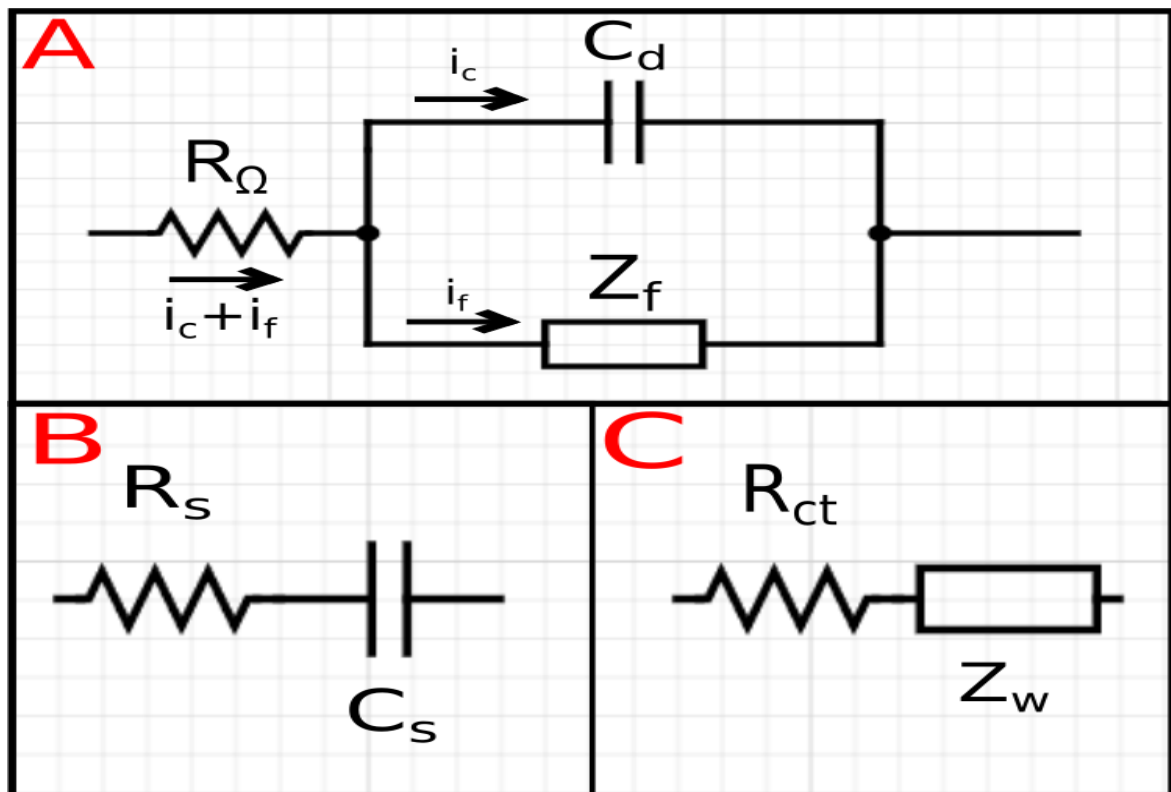


Figure 10. A) Randles equivalent circuit B) General impedance Z_f can be described with R_{ct} and C_s or with C) R_{ct} and Z_w .

The current (i_c) is needed for double-layer (C_d) charging and current (i_f) is attributed to faradaic processes. Z_f is general impedance which can be described in two ways with series resistance (R_s) and pseudocapacity (C_s) or with charge-transfer

resistance (R_{ct}) and **Warburg impedance (Z_w)** which is associated with mass transfer. (R_Ω) is presenting solution resistance. The elements contributing to Z_f are not ideal and change according to **angular frequency (ω)** defined by frequency (f) as depicted by Equation 16.¹⁵

$$\omega = 2\pi f \quad (16)$$

Sinusoidal current (i) is defined in Equation 17 with ω , time (t), **phase angle (ϕ)**, and the amplitude of current (I):

$$i = I \sin(\omega t + \phi). \quad (17)$$

ϕ is used to describe the difference in phases of, for example, current phasor and potential phasor in **phase diagrams**. Commonly small sinusoidal current or potential signal is applied to the electrochemical system studied in EIS. Then the signal received from the system is used to calculate **impedance (Z)**. Impedance can be thought as the equivalent to resistance in AC circuits. Relationship of impedance, voltage, and current can be described with generalized Ohm's law (Equation 18) written as^{15,17}

$$\varphi = ZI. \quad (18)$$

Impedance can be divided into real (Z_{Re}) and imaginary (Z_{Im}) components which can be written in form of Equation 19

$$Z(\omega) = Z_{Re} + jZ_{Im}, \quad (19)$$

where j is the imaginary number $\sqrt{-1}$. From Equation 19 we can see that impedance depends on frequency. The frequency dependent portion of impedance is Z_{Im} which comes from reactance (X). Reactance can be divided into capacitive reactance (X_C) and inductive reactance (X_L). This division can be written as Equation 20.¹⁵

$$X = Z_{Im} = X_C + X_L. \quad (20)$$

Inductive reactance describes inductors ability to oppose changes in current by its self-induced electromotive force. Larger frequency leads to larger X_L which leads to lowered I . X_L is the product of ω and inductance (L) as shown by Equation 21.¹⁷

$$X_L = \omega L. \quad (21)$$

Inductive elements are not used in Randles circuit. Capacitive reactance describes capacitors tendency to pass high frequency signals and filter low frequency signals. This connection can be seen from Equation 22,¹⁷ where

$$X_C = \frac{1}{\omega C}. \quad (22)$$

Z_{Re} however comes from resistance (R) and is not affected by the alternating current in an ideal scenario (Equation 23) and thus¹⁷

$$Z_{Re} = R. \quad (23)$$

Equations 24 and 25 written below can be derived for R_s and C_s mentioned before. R_s can be defined as

$$R_s = R_{ct} + \frac{\sigma}{\omega^{1/2}} \quad (24)$$

where σ is the **Warburg coefficient** associated with kinetic parameters of a standard redox reaction and Warburg impedance. C_s can be defined as

$$C_s = \frac{1}{\sigma \omega^{1/2}}. \quad (25)$$

Equations 26 and 27 can be derived for Z_{Im} and Z_{Re} which can be written as

$$Z_{Re} = R_\Omega + \frac{R_{ct} + \sigma \omega^{-1/2}}{(C_d \sigma \omega^{\frac{1}{2}} + 1)^2 + \omega^2 C_d^2 (R_{ct} + \sigma \omega^{-1/2})^2} \quad (26)$$

and

$$Z_{Im} = \frac{\omega C_d (R_{ct} + \sigma \omega^{-1/2})^2 + \sigma \omega^{-\frac{1}{2}} (\omega^{\frac{1}{2}} C_d \sigma + 1)}{(C_d + \sigma \omega^{\frac{1}{2}} + 1)^2 + \omega^2 C_d^2 (R_{ct} + \sigma \omega^{-1/2})^2}. \quad (27)$$

Chemical information can be derived by plotting Z_{Im} vs. Z_{Re} for different ω . This plot is called the Nyquist plot and is commonly used in research papers to present EIS data (Figure 10). At low frequencies ω approaches zero and there is linear correlation between Z_{Im} and Z_{Re} described by Equation 28 which can be derived from Equations 26 and 27.¹⁵

$$Z_{Im} = Z_{Re} - R_{Re} + R_{ct} + 2\sigma^2 C_d. \quad (28)$$

At very high frequencies ($\omega \rightarrow \infty$) Warburg impedance becomes unimportant and half-circle with center at $Z_{Re} = R_{\Omega} + R_{ct}/2$ and $Z_{Im} = 0$ with radius of $R_{ct}/2$ is observed on Nyquist plot. This is described by Equation 30 as¹⁵

$$(Z_{Re} + R_{\Omega} - \frac{R_{ct}}{2})^2 + (Z_{Im}^2)^2 = (\frac{R_{ct}}{2})^2. \quad (30)$$

Combining the half-circle and the linear part will result into Nyquist plot presented in Figure 11.

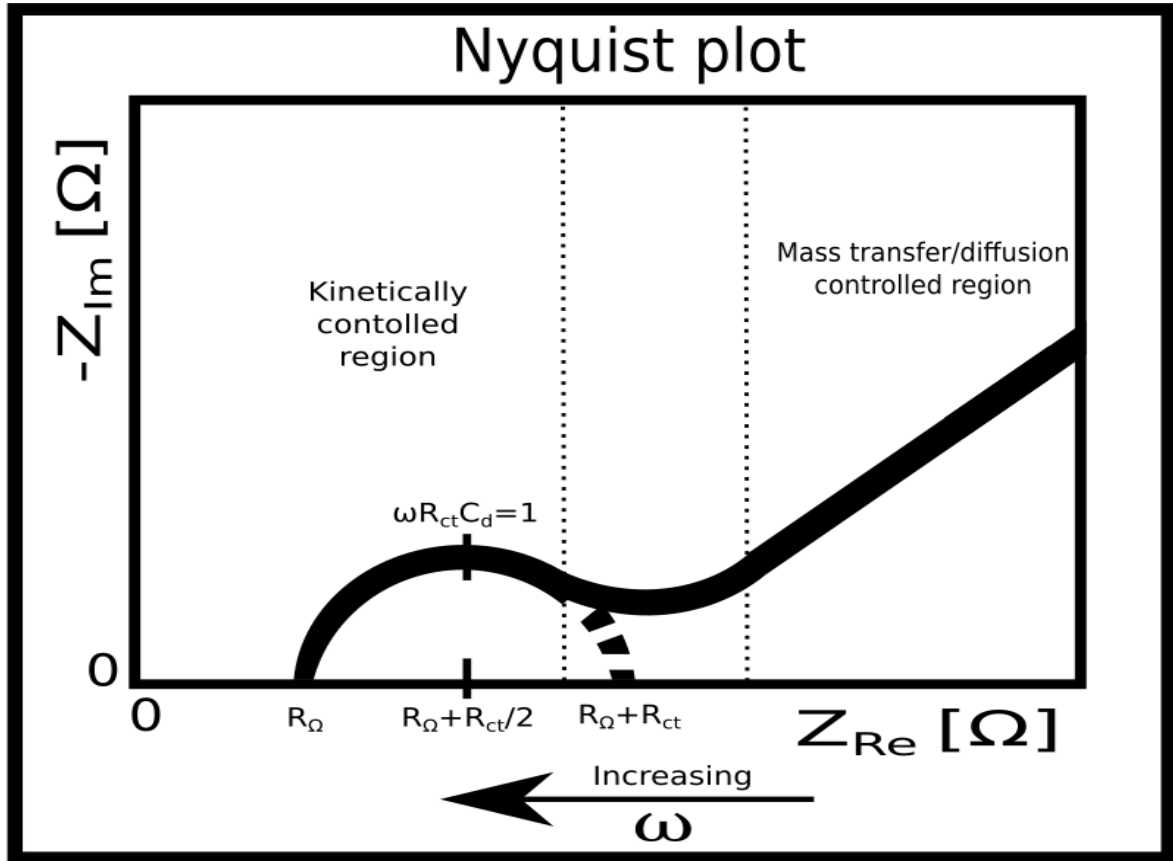


Figure 11. Common shape of a Nyquist plot from measuring impedance at different angular frequencies.^{15,26} Notice the negative sign ahead of Z_{Im} .

Figure 11 is from a real research paper²⁹ and we can see that the Nyquist plot has a shape similar to Figure 11.

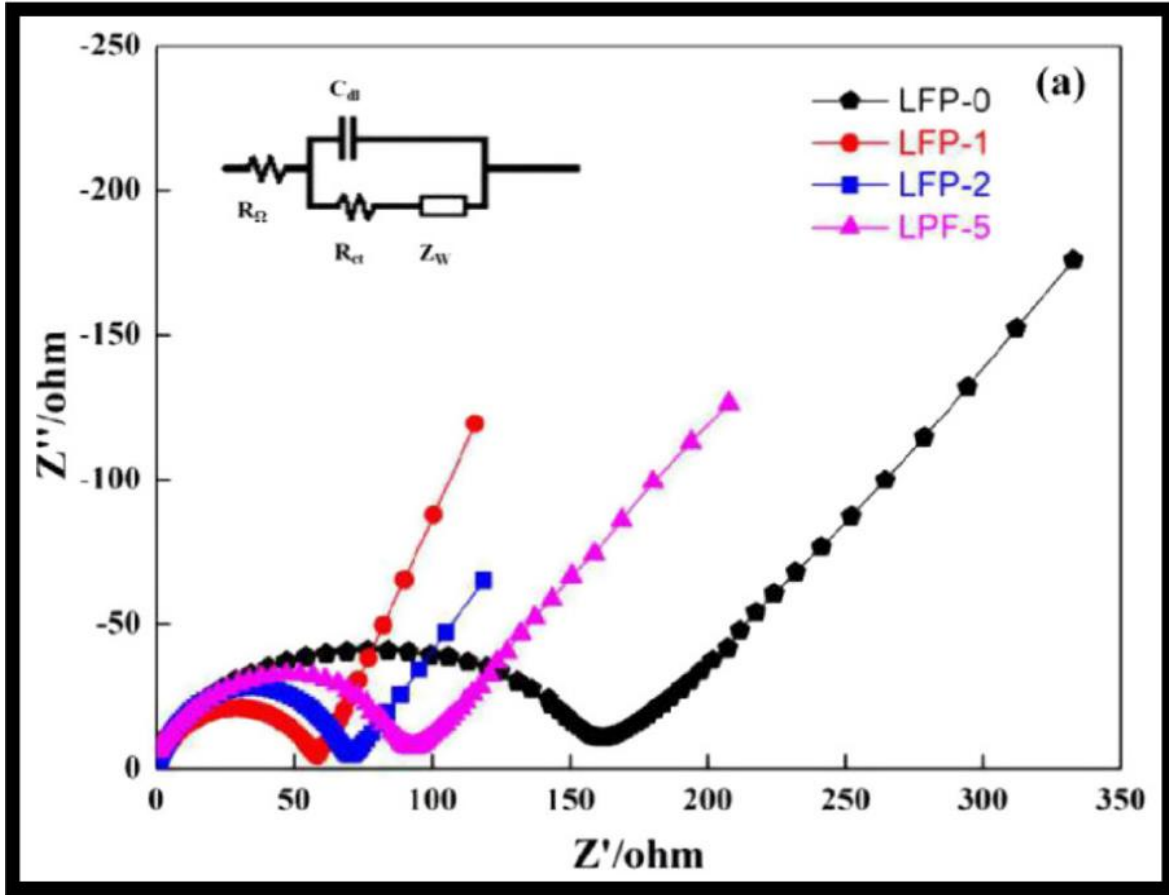


Figure 12. Figure from article by Yuan Gao *et al.*²⁹ We can see that LFP-1 has the least amount of R_{ct} and R_{Ω} by the position and size of the half-circles.²⁹

From the Nyquist plot R_{ct} and R_{Ω} can be calculated. Using Equation 31 σ can be calculated.

$$Z_{Re} = R_{\Omega} + R_{ct} + \sigma \omega^{-1/2} \quad (31)$$

After that Li-ion diffusion coefficient can be calculated using Equation 32.

$$D_{Li}^+ = \frac{R^2 T^2}{2 A^2 n^4 F^4 C_{Li}^2 \sigma^2} \quad (32)$$

Sometimes different equations than the ones presented here are used to derive the Li-ion diffusion coefficient, but Equations 31 and 32 are common.²⁶ EIS can also be used to define the **exchange current density** of an electrochemical cell, which is the net current of an electrochemical cell in the absence of external electric field.²⁶

5 THE OLIVINE CRYSTAL STRUCTURE OF LITHIUM IRON PHOSPHATE

5.1 Basic crystal geometry

Before we can go into doping of LFP we need to understand the crystal structure of LFP, and to do that we need to know the basics of crystal geometry. A **crystal** is a solid compound composed of atoms, ions or molecules arranged in periodic three-dimensional pattern, also known as **the basis**. The crystal structure is then presented mathematically with **lattices**, **lattice points**, **interaxial angles (α , β , γ)** and **lattice vectors (a , b , c)**. The lattice points are separated by a distance of the lattice vectors lengths and lattice points can be generated by applying the vectors repeatedly. Lattice points have identical surroundings. Together the vectors and points define the crystal lattice, which is a mathematical construct unlike the basis. The lattice vectors are used to define the **unit cell (Figure 13)** which is a small repeating pattern of crystal lattice. The crystal lattice is a repetition of these unit cells through the crystalline material. One thing to note is that the crystal lattice can often be defined with **alternate unit cells**.³⁰

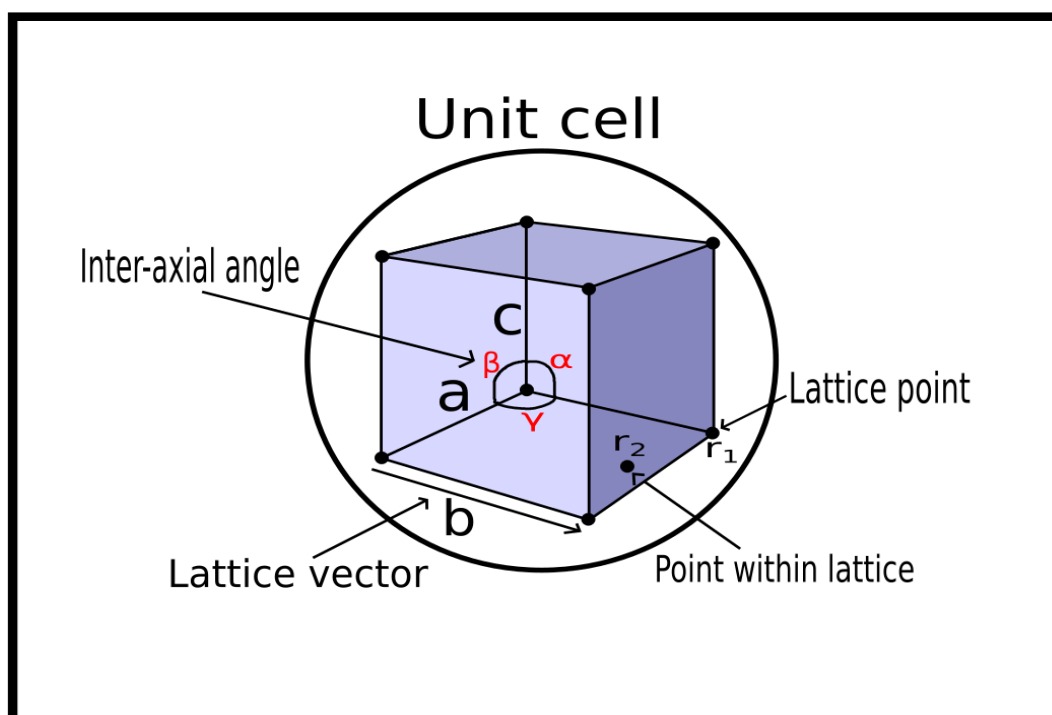


Figure 13. Example of a unit cell, the repeating structure in crystal lattice. Drawn by Jere Leinonen.

Points in the lattice can be defined with respect to the origin of the lattice by position vector. This can be formulated as Equation 33.

$$r = u'a + v'b + w'c = (na + pb + qc) + (ua + vb + wc), \quad (33)$$

where a , b , and c are the lattice vectors. n , p , q are integers which are used to define lattice points (r_1). u , v , and w are fractions used to define the points that are not lattice points (r_2). Basically, two vectors, one between lattice points, and the other from lattice point to inside the cell can define r_2 . u' , v' , and w' contain the integer and the non-integer values.³⁰

Now that we know how to define points, we can define lines in the lattice by drawing a line through origin point to a given line and then giving coordinates to any one point drawn on the line. Let the point have coordinates u' , v' , and w' . **Indices** of the line are then $[uvw]$. They are also the indices of any line parallel to the given line as lattices are infinite and origin point can be taken at any point. The values of u' , v , and w' are always converted to smallest integers in the index by multiplication or division. For example, $[\frac{1}{2}\frac{1}{2}1]$, $[112]$, and $[224]$ all represent the same direction but $[112]$ is the preferred index. Negative indices are written with a bar over the number e.g. $[\bar{1}00]$. Figure 14 below shows examples of indices of lines.³⁰

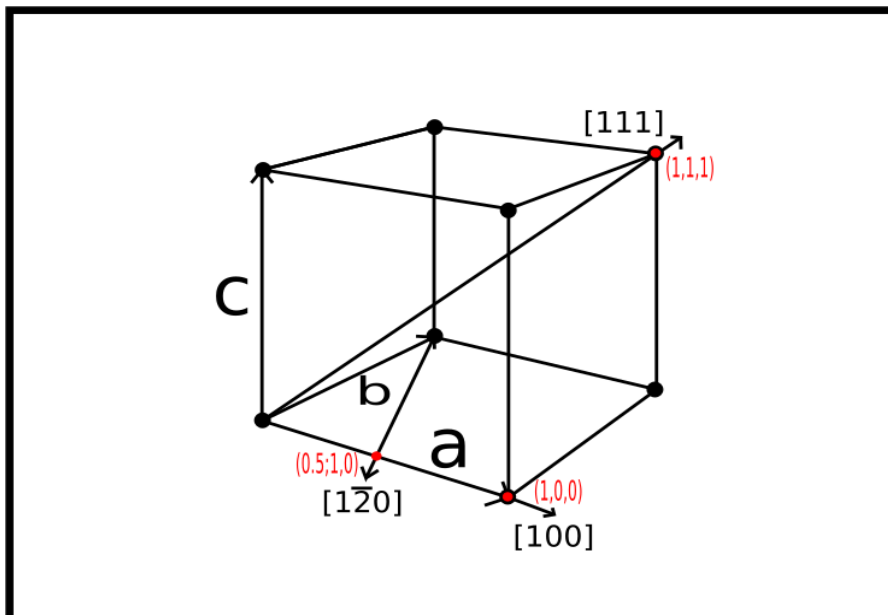


Figure 14. Examples on how to mark indices of lines in a lattice drawn by Jere Leinonen.

Planes are described with indices called **Miller indices**. Orientation of the plane can be described by giving the distances at which the plane intersects a vector axis measured from the origin as a fraction of the axial lengths. Similarly to lines, three indices: **h, k, and l** are used to describe the fraction of the axial length. They are defined as the “reciprocals of the fractional intercepts which the plane makes with the crystallographic axes.”³⁰ See Table 2 and Figure 15 for example.

Table 2. Example parameters for determining Miller indices.

Lattice vector	a	b	c
Axial length	4 Å	4 Å	6 Å
Intercept length	1 Å	4 Å	6 Å
Fractional intercepts	1/4	1/1	1/1
(hkl)	$h = 4$	$k = 1$	$l = 1$
Miller indice	(411)		

When the plane is parallel to some of the axis then the Miller index value is zero and when the plane cuts negative axis the corresponding index is negative and bar is put on top of it.³⁰

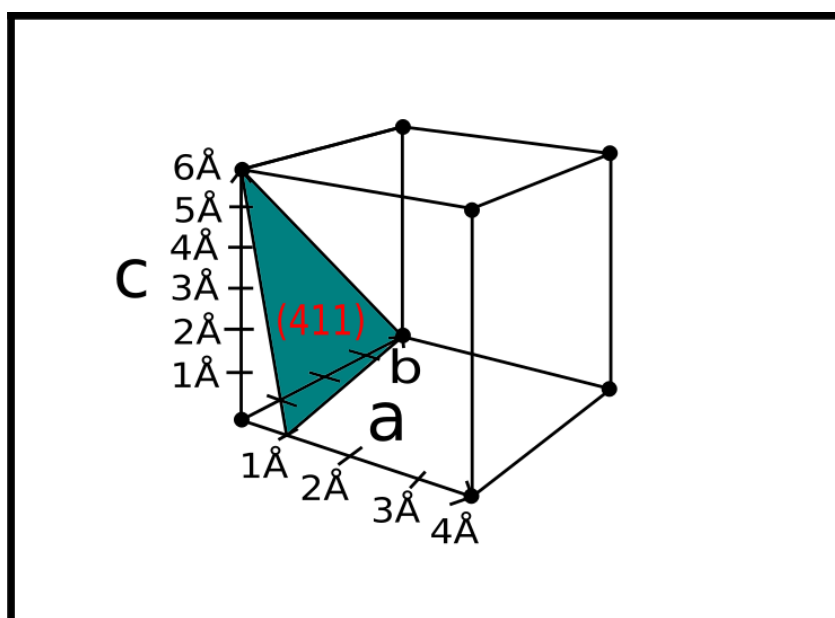


Figure 15. Describing a plane in crystal lattice with Miller indices. Drawn by Jere Leinonen.

With the help of **X-ray diffraction (XRD)** interplanar spacing d_{hkl} can be calculated with Bragg's law. This is the distance between two planes of the same indice as shown in Figure 16.³⁰

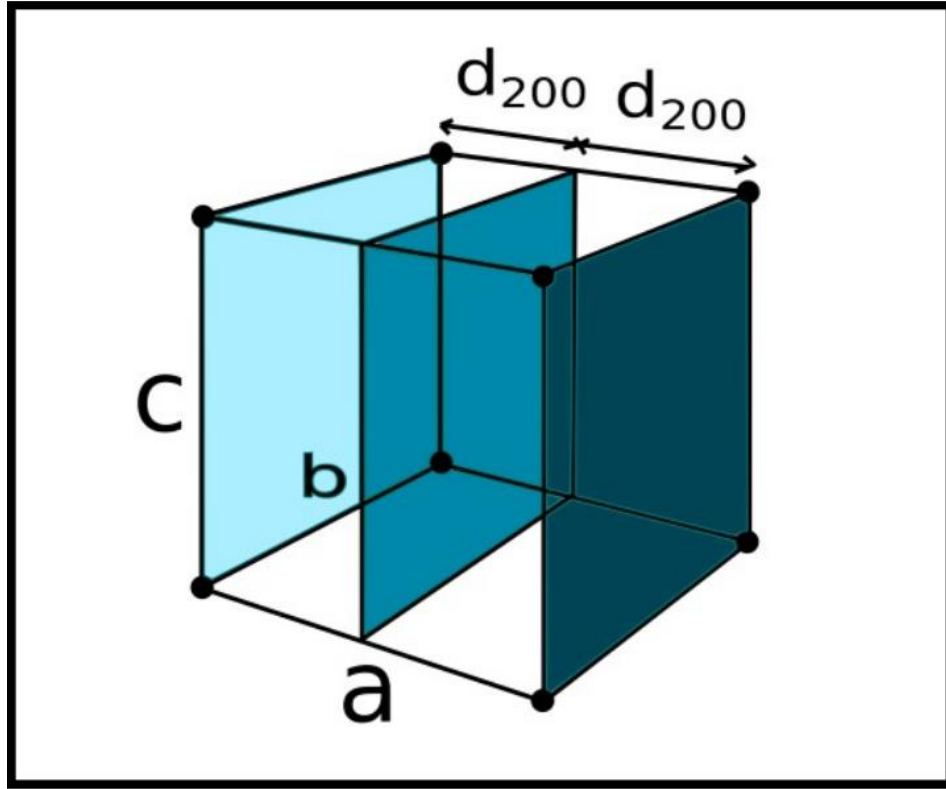


Figure 16. Interplanar spacing of plane (200) drawn by Jere Leinonen.

The plane spacings in orthorhombic system can be calculated with Equation (34).

$$\frac{1}{d^2} = \frac{h^2}{a^2} + \frac{k^2}{b^2} + \frac{l^2}{c^2}, \quad (34)$$

where d is the interplanar distance, a , b , and c are the lattice vector lengths and h, k , and l are the Miller indices.³⁰

It has been proven that only seven different kind of **point lattices** are needed to define all crystals by the lattice vectors and vector angles to **crystal systems**. However, 14 different point lattices are used as seven more point lattices can be defined from the fact that each lattice point have different surroundings. These are called **Bravais lattices**. Often Bravais lattice and point lattice are used as synonyms. Unit cells can be divided to **simple (P) also known as primitive and non-primitive (A, B, C, F, I, R)**. Primitive cells have only points in corners (N_c) and they have only one lattice point per cell while non-primitive cells have points on their faces or inside and have more than one lattice point. The amount of lattice point can be calculated by Equation 35:³⁰

$$N = N_i + \frac{N_f}{2} + \frac{N_c}{8} \quad (35)$$

where, N is the amount of lattice point, N_i are the internal lattice points belonging completely to the cell, N_f are the lattice points on faces that are shared between two cells, and N_c are the corner point shared between eight cells. Example of orthorhombic and hexagonal Bravais lattices can be seen in Figure 17 below.³⁰

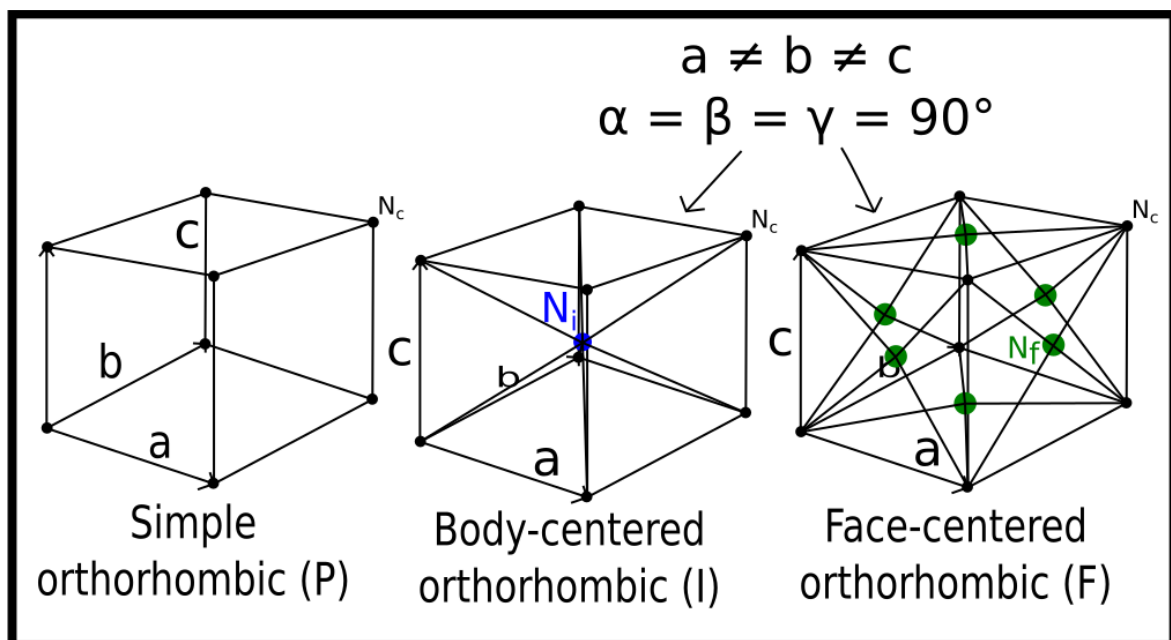


Figure 17. Three of the four Bravais lattices of the orthorhombic crystal system and the defining vector lengths and angles. N_c marks corner point, N_i internal point, and N_f face point.³⁰ Drawn by Jere Leinonen.

Symmetry operations and elements are also needed to define repetition in the crystals. Symmetry operations change the orientation of repeated features or **motifs** in the lattice. The operations describe the changes which the lattice vectors and lattice angles cannot. The symmetry elements tell where to look for identical objects, except for orientation, relative to the symmetry element. The elements tell where the operation is carried out. A structure is said to be identical when you can do the symmetry operation and everything overlaps with the original. This can be demonstrated by rotating cube by 90° or by putting a **mirror plane** in the middle of a cube. By rotating the cube through an axis by 90° the cube looks identical. Same can be said when a mirror is placed in the middle of the cube as both halves of cube are identical and make up the complete cube by **reflection**.³⁰ Figure 18 shows example of rotation axes and mirror plane. Combining mirror and translation produces **glide plane**.³¹ The symmetry elements act through a point and are thus called **point groups**.³⁰

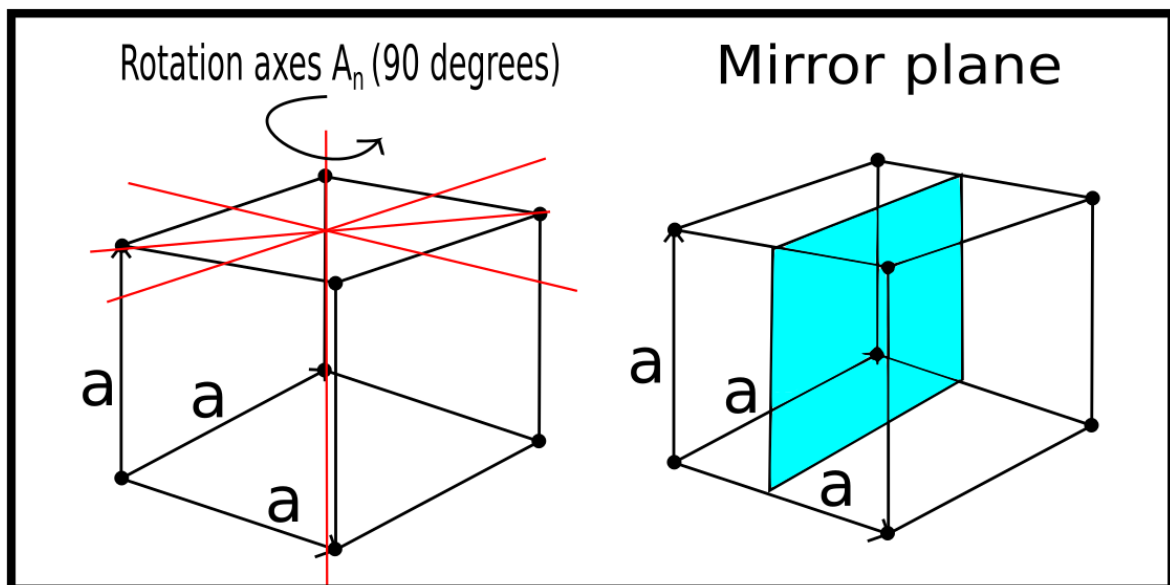


Figure 18. Rotation axes and mirror planes are common symmetry elements.

Drawn by Jere Leinonen.

Point groups together with lattice parameters makes up the **space group** which defines the spatial arrangement of crystal system. There are 230 unique space groups in three-dimensions. The simplest crystals are formed by placing identical atoms to the Bravais lattice points. However, most crystals are not like this and multiple atoms can be associated with each point of Bravais lattice.³⁰ One example of this is the **hexagonal close-packed (HCP) structure** seen in Figure 19 below.

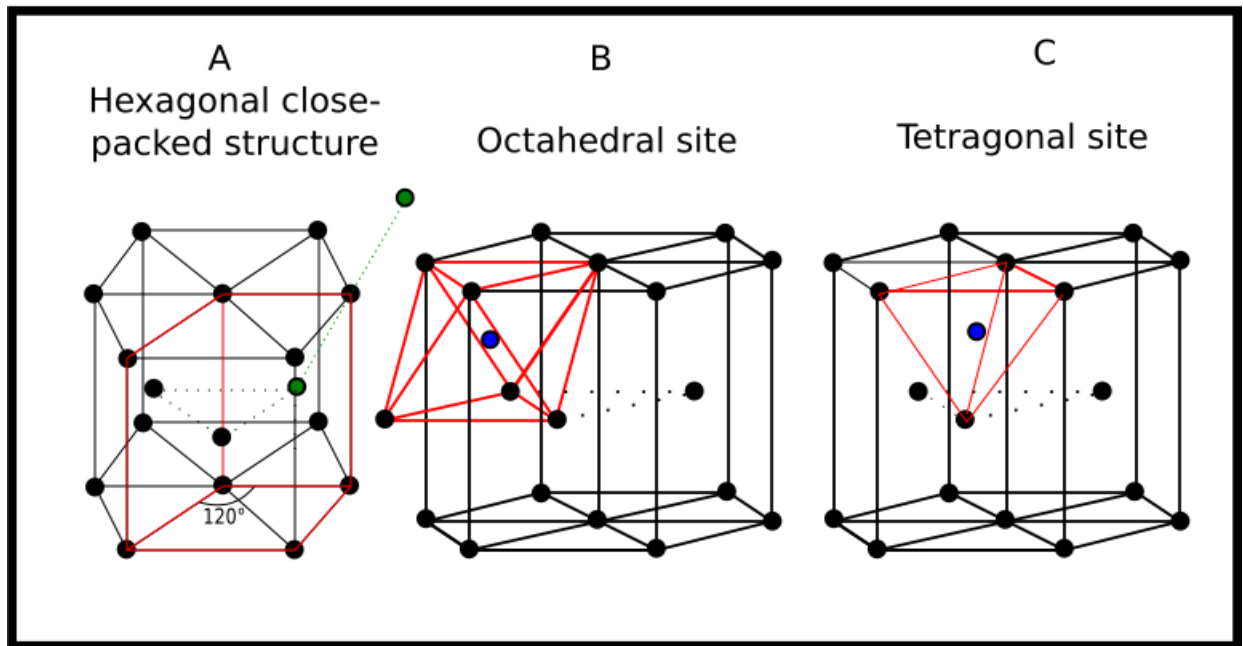


Figure 19. A) The hexagonal close-packed (hcp) crystal structure with its Bravais lattice in red. Green marks the one pair of atoms associated to one point. B) Shows one possible octahedral site in hcp. Blue marks interstitial site (**void**) where an atom can fit. C) Shows one possible tetrahedral site in hcp. The red lines mark the lattices/sites shape.

5.2 The crystal structure of lithium iron phosphate

Lithium iron phosphate has **olivine distorted hexagonal close-packed crystal structure** with **orthorhombic unit cell** and it belongs to space group ***Pbnm***,³ also known as group 62.³² What does *Pbnm* mean? *Pbnm* are the **short Hermann-Mauguin symbols, also known as short international symbols**, for LFP's space-group. The symbols can be divided into "*P*" and "*mmm*" parts for orthorhombic system. The "*mmm*"-part refers to the symmetry directions of the lattice, which orthorhombic system has three: $a = [100]$, $b = [010]$, and $c = [001]$. The "*P*"-part refers to the Bravais lattice type.³² See Figure 20 below to see what *b*, *n*, and *m* mean.

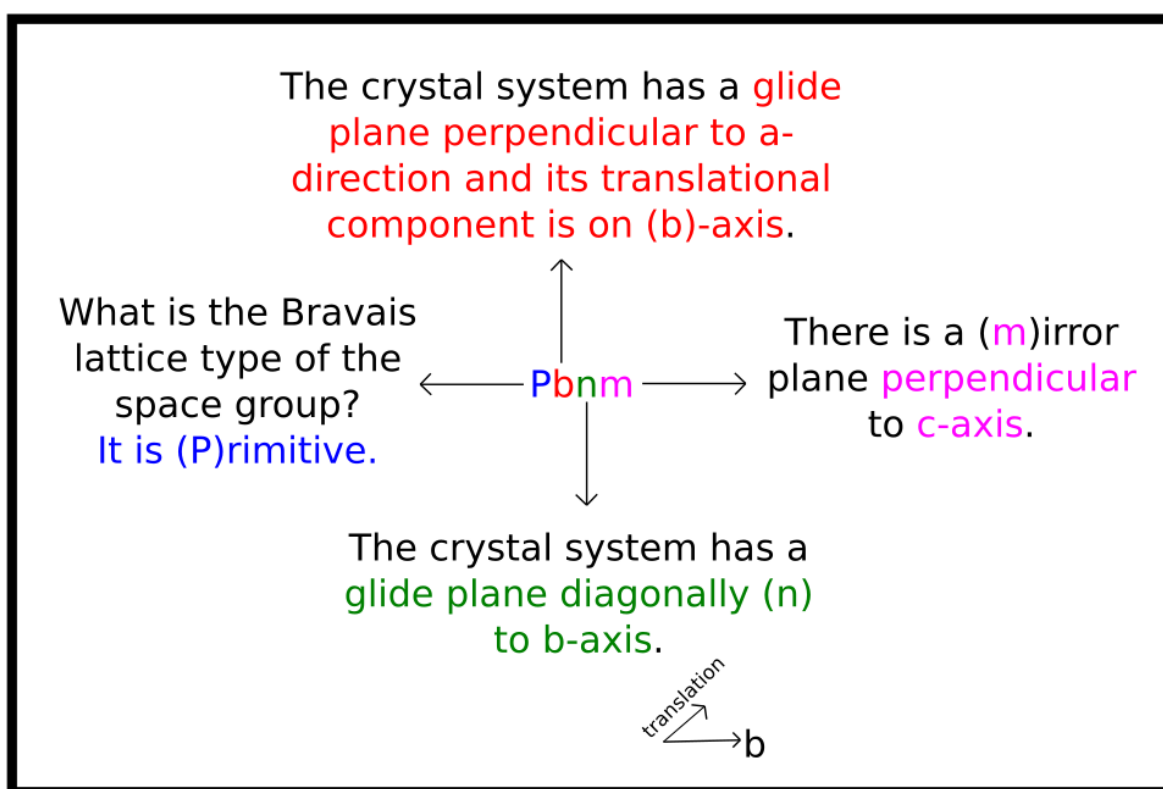


Figure 20. Space group symbols of LFP explained.³² Drawn by Jere Leinonen.

The orthorhombic unit cell of LFP is depicted on the next page in Figure 21. We can see octahedrons and tetrahedrons in the structure. The dark octahedrons are FeO_6 that share some of the oxygen atoms with light tetrahedral PO_4 and with each other. The phosphorus and iron are in the center of these shapes and oxygen on the corners.³ The lithium also forms LiO_6 octahedra that is not drawn often to pictures.

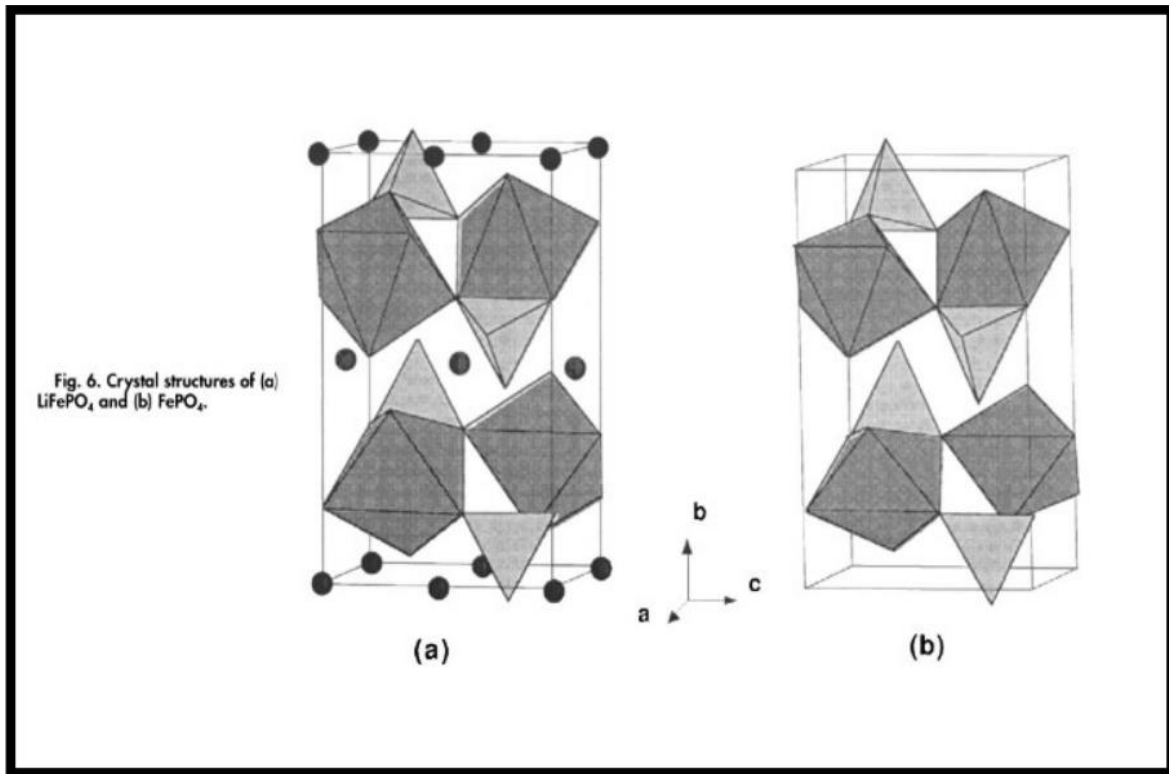


Figure 21. Orthorhombic unit cell of LFP from the study of Goodenough *et al.* reprinted with permission from IOP Publishing, Ltd.³ The dark balls are lithium ions. The octahedral shapes form from FeO_6 and the tetrahedral shapes form from PO_4 . In a) we can see LiFePO_4 with lithium in the structure. In b) we see that the shapes change little bit as the lithium is no more in structure.

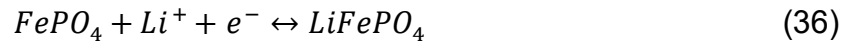
The P-O covalent bond is strong which stabilizes oxygen atoms leading to high thermal stability.⁵ The FeO_6 network is not continuous, and electrons can only be transferred through the Fe-O-Fe chain leading to low electrical conductivity of magnitude of $10^{-9} \sim 10^{-10} \text{ S/cm}$ at room temperature.^{6,33} Because of this pure LiFePO_4 is classified as semiconductor, **more specifically n-type semiconductor**, which means that conduction comes from free electrons. Pure **p-type semiconductors** on the other hand have holes, thought as positive charges, that carry the current. Doped LFP is p-type semiconductor.^{19,34}

Lattice parameters for LiFePO₄ and FePO₄ can be found in Table 3.

Table 3. Lattice vector lengths and volume of unit cell in Ångstroms.³⁵

Compound	a(Å)	b(Å)	c(Å)	V(Å ³)
LiFePO ₄	10.3449	6.0137	4.6990	292.33
FePO ₄	9.8213	5.7927	4.7886	272.43

We can see from the vector lengths that the structure is not perfectly rigid and that the cell shrinks a little during charge when Li⁺ leave LFP. The charge-discharge reaction for LFP is shown in Equation 36.³⁶



Computational and experimental studies show that Li⁺ migration in nanosized LFP particles occurs mostly via one dimensional channels along the [010] direction particles as shown in Figure 22.³⁷

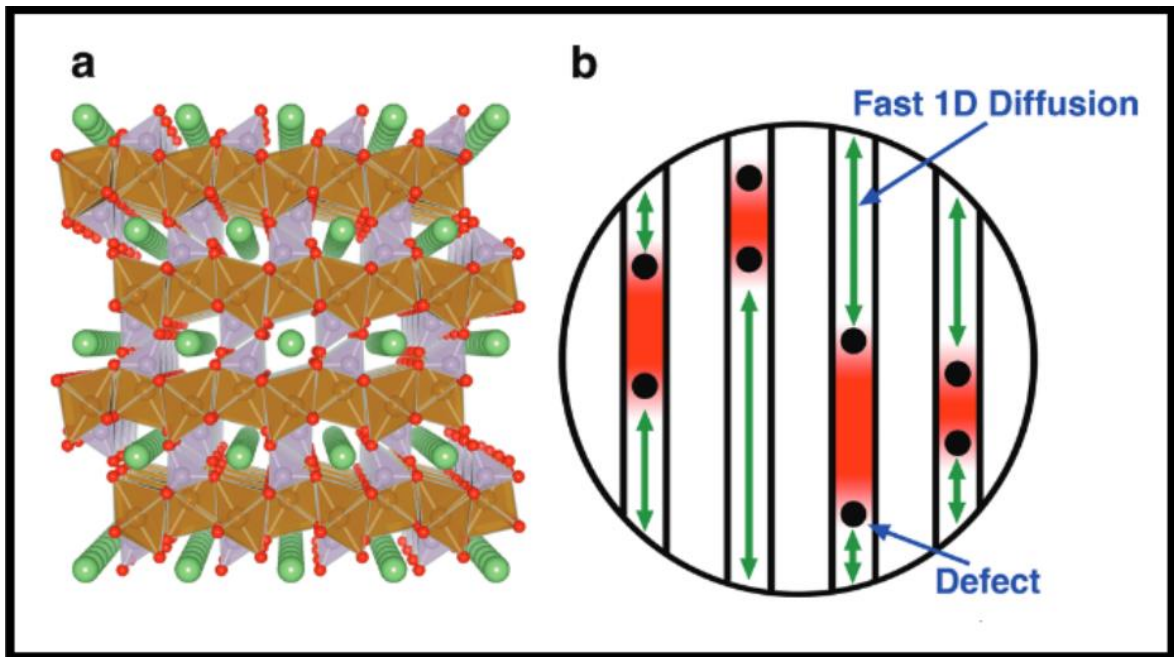


Figure 22. A) 1D-Li⁺ diffusion channels along [010] direction (b-axis). Li atoms are green, oxygen atoms red, FeO₆ is brown, and phosphate is purple. B) Point defects on the channels stopping lithium-ion diffusion to certain sites inside the material. Figure reprinted from article by Malik *et al.* with permission from American Chemical society.³⁷

The Li^+ ion diffusion along perfect b direction is calculated to be so fast ($D \sim 10^{-8} \text{ cm}^2\text{s}^{-1}$) that nanosized particles (100 nm) would be delithiated in 0.01 second and micrometer sized particles in a second if the intrinsic Li^+ mobility would be the rate-controlling factor. Macroscopic particles on the other hand have worse transport properties that are also different as more Li^+ diffusivity occurs along a, and c axes. The mostly one-dimensional diffusion is also hindered by possible defects on the diffusion channels. These defects as shown in Figure 21 will prevent the Li^+ diffusion and have huge impact to the diffusion time. Even 0.05 % defect concentration will decrease the characteristic diffusion time by order of magnitude.³⁷ The defect with the lowest energy is the cation **antisite defect** in which Li and Fe ions exchange position.³⁸

In short even very low number of defects on diffusion channels will increase diffusion time and nanosized particles have faster diffusion compared to bigger ones. The nanosizing also leads to lower packing density and thus lower energy density for batteries. For portable and moving applications larger defect free LFP particles are desirable.³⁷ The **tap density** of LFP should be kept at an acceptable level such as over 1.5 g/cm^3 to keep the volumetric energy density at a reasonable level.³⁹

6 SYNTHESIS OF DOPED LITHIUM IRON PHOSPHATE

6.1 Solid state synthesis

Solid-state synthesis methods are done at high temperature without solvent. The synthesis is simple and easy to industrialize. The downsides are that the prepared LFP has large particle size, is non-crystalline, non-uniform, and the synthesis time is long. The process usually requires repeated grinding (ball-milling) and calcination. Common lithium sources include Li_2CO_3 , $\text{LiOH}\cdot 2\text{H}_2\text{O}$, LiF , and LiCH_3COO . Common iron sources include $\text{Fe}(\text{CH}_3\text{COO}_2)_2$, $\text{FePO}_4(\text{H}_2\text{O})_2$, and $\text{FeC}_2\text{O}_4\cdot 2\text{H}_2\text{O}$. Common phosphorous sources include H_3PO_4 , $\text{NH}_4\text{H}_2\text{PO}_4$ and $(\text{NH}_4)_2\text{HPO}_4$.³⁵ One example of solid-state synthesis is presented in Figure 23. Common impurities for LFP synthesis include Fe_2O_3 and $\text{Li}_3\text{Fe}_2(\text{PO}_4)_3$.⁴⁰

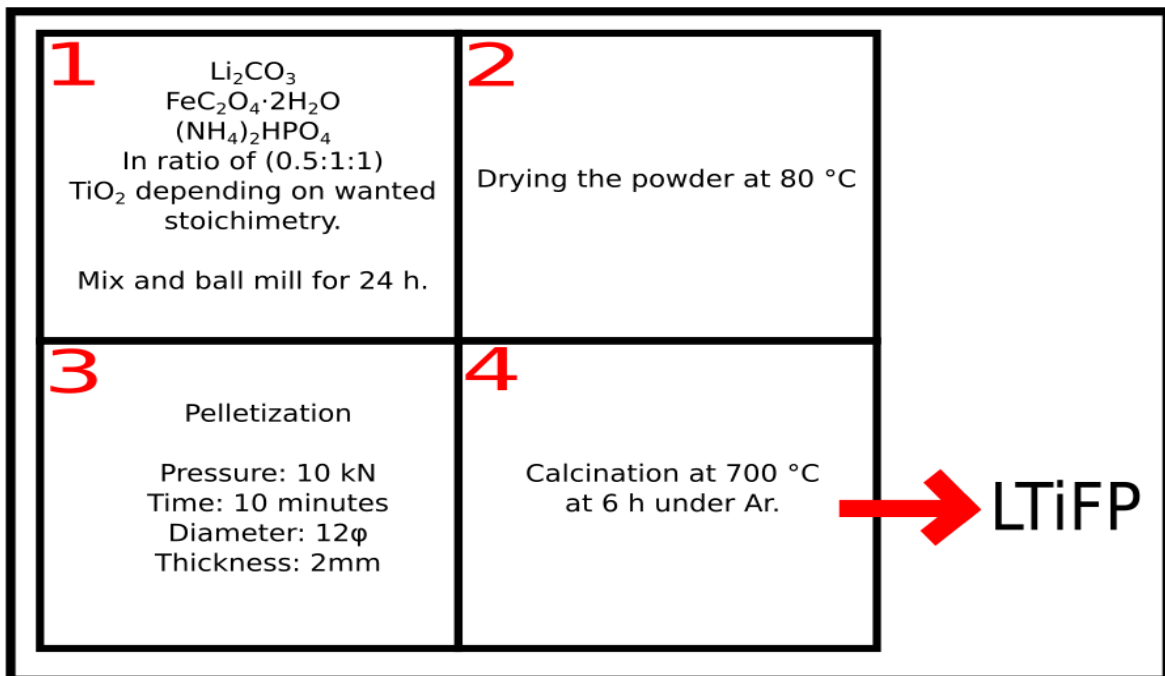


Figure 23. Kim *et al.* synthesized Ti-doped LFP with typical solid-state method via the presented route.⁴¹

6.1.1 Mechano-chemical activation

Mechano-chemical activation is based on increasing the reactivity of mixtures by high energy ball milling. The milling increases surface area and produces free valences (unbound electrons) on the outer layer of the material both of which increase reactivity. The powder produced has relatively low particle size and high surface area. The downsides are the temperature rise and impurities from milling.³⁵ Figure 24 shows one example of ball milling synthesis.

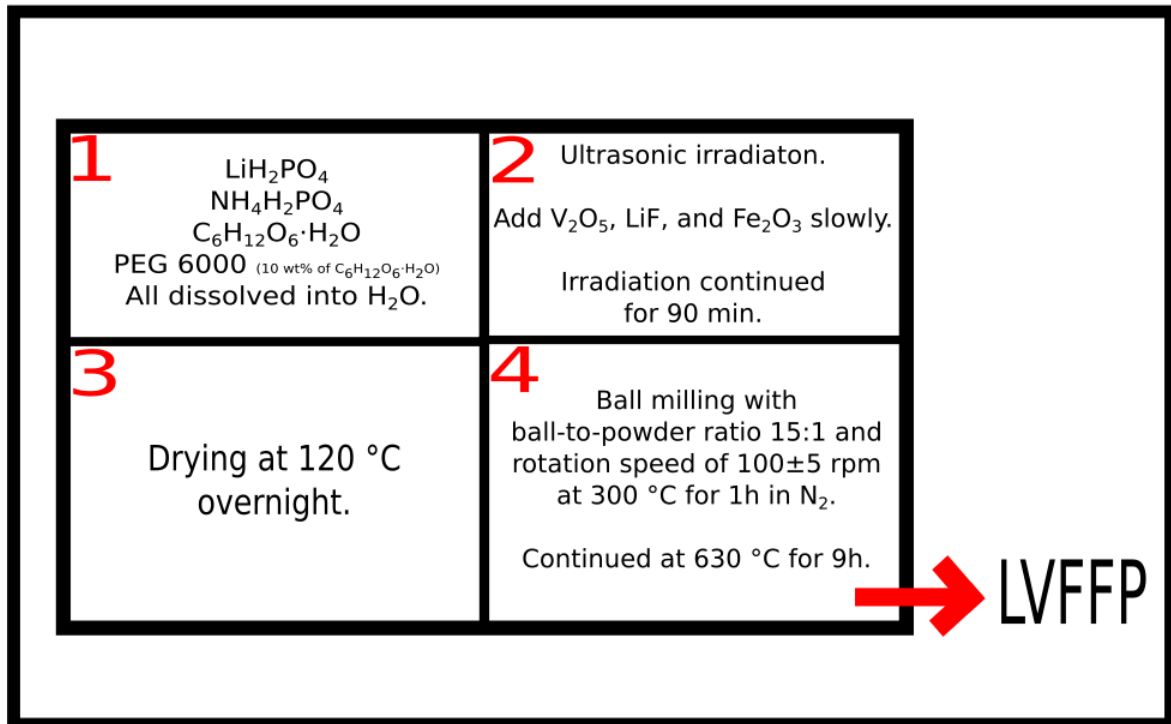


Figure 24. Li *et al.* used ball milling-based synthesis for V and F doped LFP.⁴² Ball milling is also commonly used in other synthesis routes to break down particles.

6.1.2 Carbothermal reduction

Carbothermal reduction allows the use of Fe(III) reagents instead of Fe(II). Fe(III) compounds are cheaper, more available, and chemically stable compared to Fe(II) compounds. It is also energy efficient and can produce fine, uniform particles with high capacity. In the synthesis carbon source like Carbon black, graphite, or pyrolyzed organic chemicals are used as a reducing agent. The carbon is mixed with other reagents with ball milling and then the resulting powder is calcined.³⁵

Two main reactions occur during the calcination. Reaction (38) results in more reductive conditions and significant volume and entropy change. Reaction (37) produces less reductive atmosphere and negligible changes in volume and entropy.³⁵ Figure 25 shows one example of a carbo-thermal reaction synthesis.

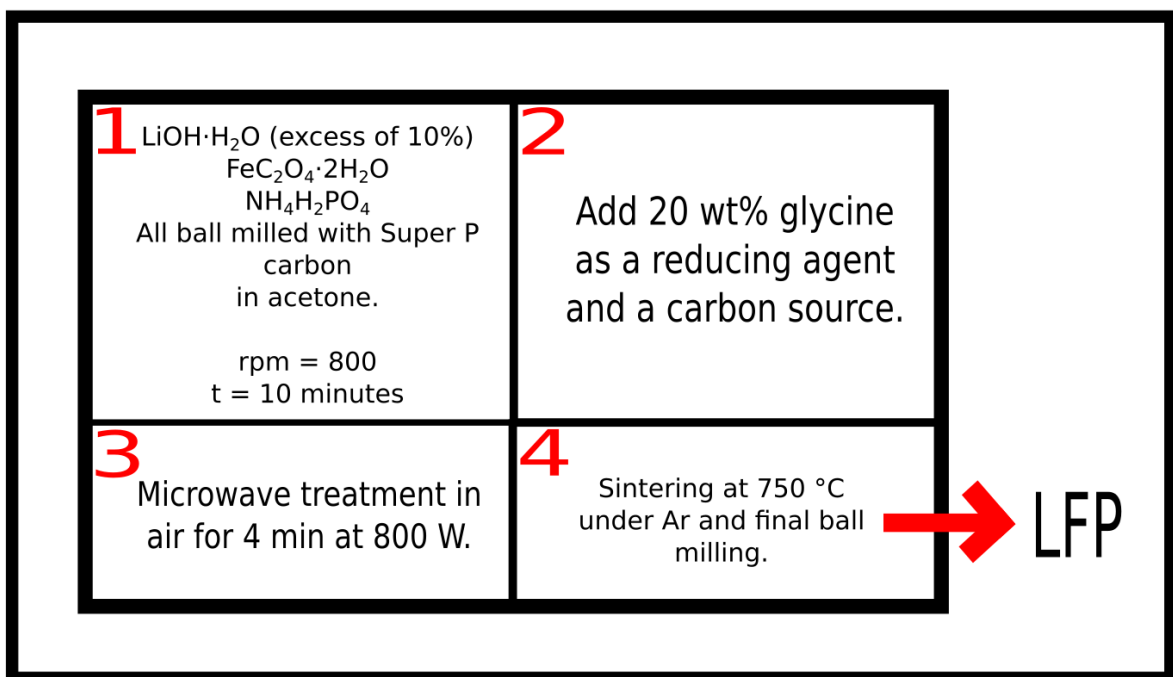
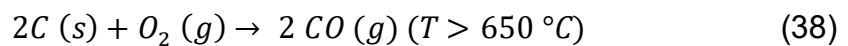
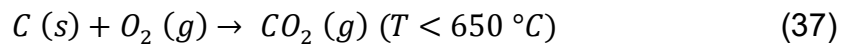


Figure 25. Fang *et al.* used carbothermal route for synthesis of K-doped LFP.⁴³

6.1.3 Microwave heating

In microwave heating the heat is generated inside the sample by rotating polar molecules. The heating rate is controlled with the power of the microwave. The advantages of microwave heating are good controllability, uniform selective heating, short processing time (2 – 20 min), energy efficiency, no need for inert gas, repeatability, and low cost. In microwave heating microwave absorber is commonly added to ensure heat generation. Commonly carbon is used as absorber as it is low cost, allows rapid heating, and forms reductive atmosphere for Fe(II). The heating time is critical for electrochemical performance of the product powders. Typically, longer heating times result in larger particle size, lower Li diffusion coefficient, Fe₂P impurities, and more capacity loss. Too short heating time results to incomplete crystalline structure and may also form contaminants which lowers charge and discharge capacities.³⁵ Figure 26 contains one example of microwave heating synthesis.

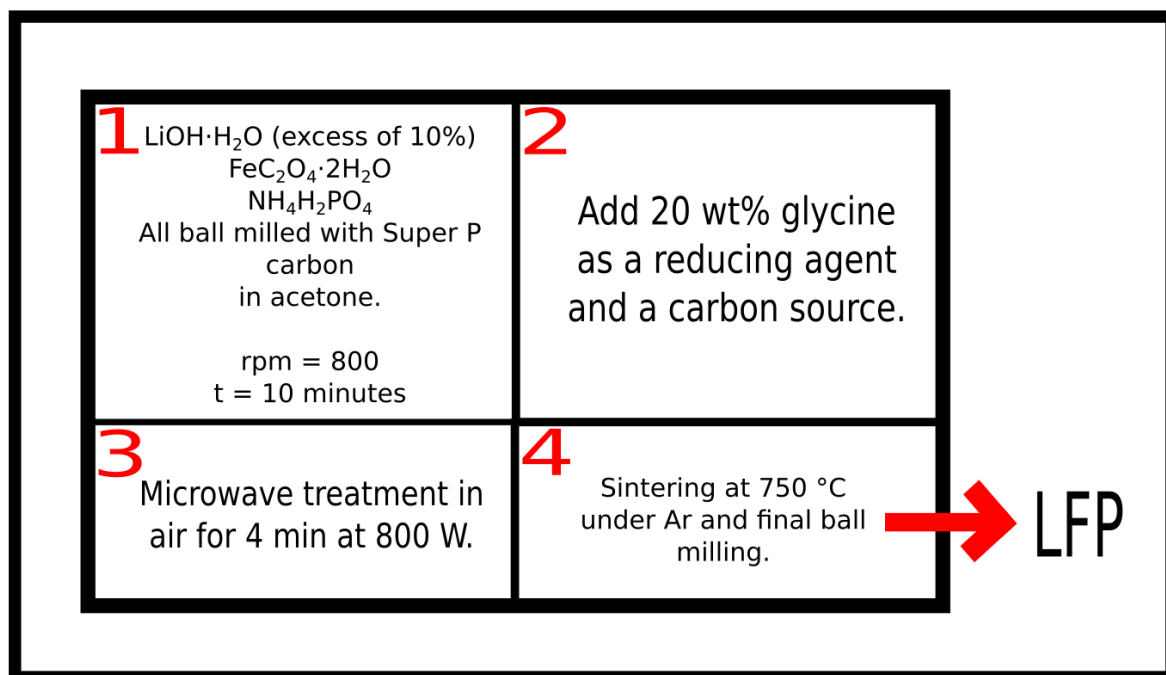


Figure 26. Calderón *et al.* synthesized LiFePO₄ with microwave heating and with tube furnace. Microwave heated sample showed better electrochemical performance.⁴⁴

6.2 Solution based synthesis

6.2.1 Hydrothermal synthesis

Solution based synthesis is done in presence of solvent. The methods are usually less time and energy consuming. They also tend to produce more uniform particles, higher purity, smaller particles, higher capacity, and more homogenous carbon coating.

In hydrothermal synthesis precursors are mixed with water and the solution is heated above the boiling temperature of water. Calcination step can be avoided if carbon coating is unwanted in hydrothermal synthesis. Hydrothermal synthesis is usually done in autoclave and the water temperature is one of the most important parameters as it controls the reaction rate, ionization degree, particle size, and crystal structure of LFP. The water flow rate and the concentration of precursors are also important.³⁵ Figure 27 contains an example of hydrothermal synthesis.

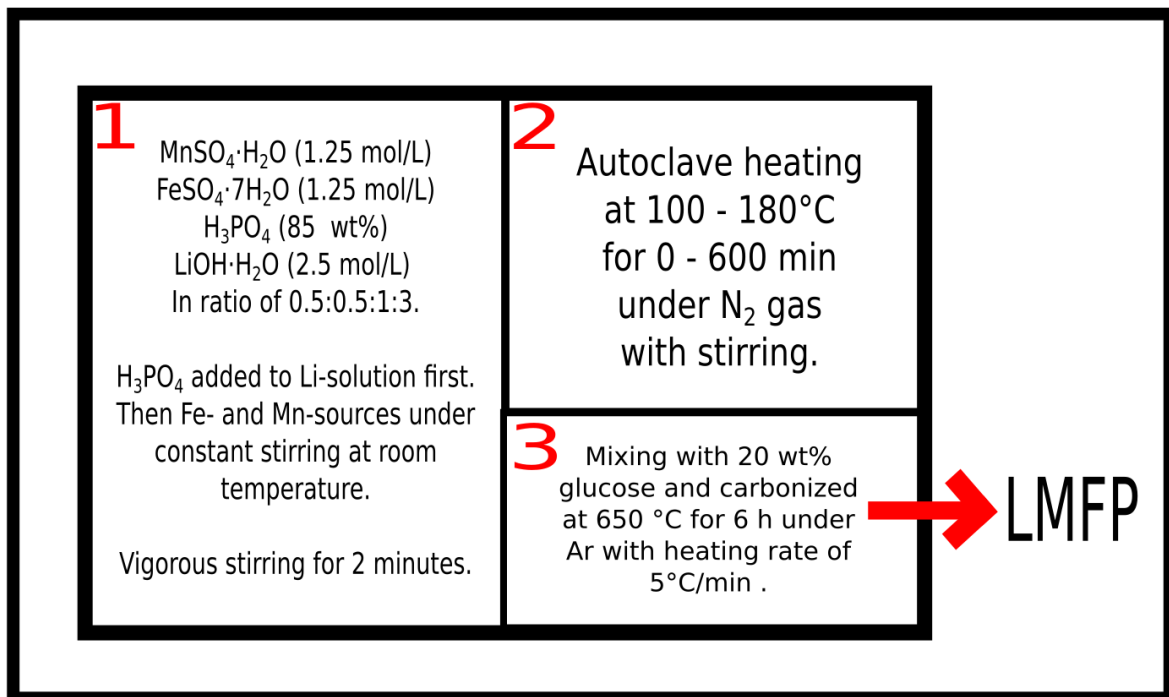


Figure 27. Xiang *et al.* synthesized $\text{LiMn}_{0.5}\text{Fe}_{0.5}\text{PO}_4$ with hydrothermal route.⁴⁵

6.2.2 Sol-gel synthesis

In sol-gel synthesis a sol and a gel are formed. First precursor materials and solvent are mixed together and then the mixture is heated, usually in low temperature, to form the sol, stable colloidal suspension of solid particles in a solvent. The heating is continued until a gel is formed. The gel is dried to form xerogel with lower volume.^{35,46} The xerogel is usually then presintered to remove excess carbon and other impurities stemming from the precursor materials. One example of this is the synthesis done by Ma *et al.*⁴⁷ Lastly the presintered material is sintered to form the final LFP powder. Reaction parameters like temperature, precursors, pH, solvent, and concentration affect the final powder. The type of solvent is extremely important for the control of powder structure. Water is the most used solvent, but organic solvents can also be used.^{35,46} Figure 28 contain one example of sol-gel synthesis.

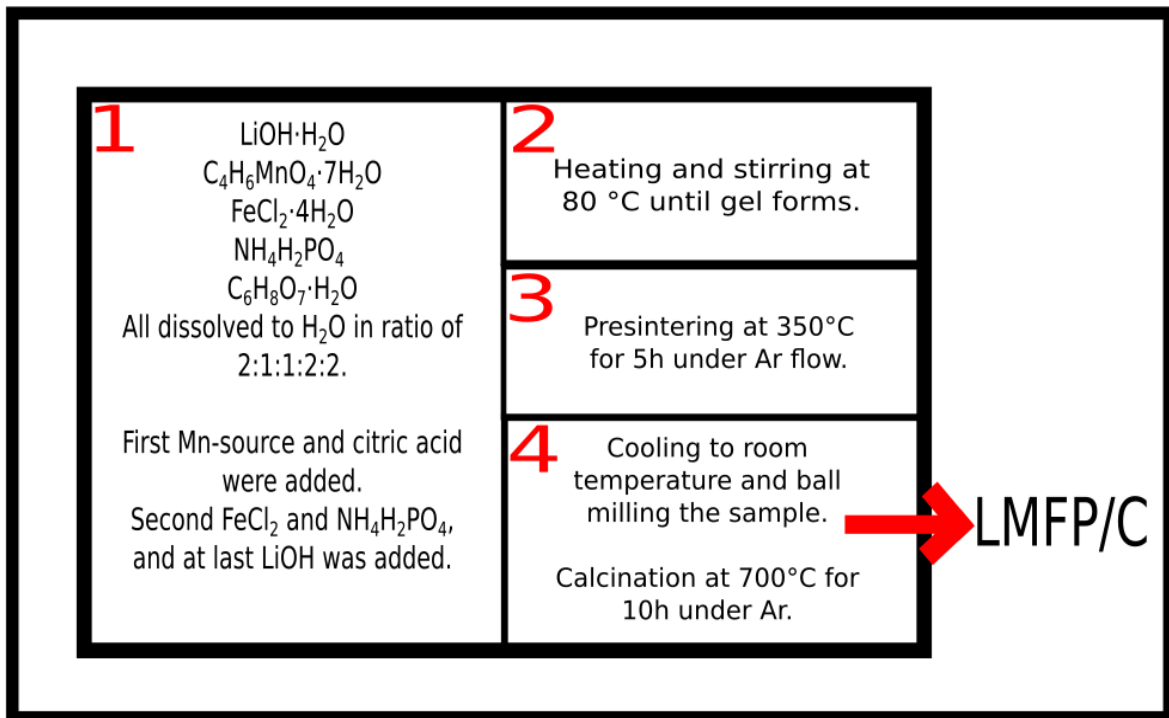


Figure 28. Liu *et al.* synthesized Mn-doped LiFePO_4 with sol-gel synthesis.⁴⁸

6.2.3 Spray pyrolysis and spray technologies

Spray pyrolysis is an important easy to control method to produce ultrafine powders of ceramic particles with narrow size distribution, and high purity. The method is based on continuous generation of droplets from a solution containing colloidal particles. Droplets can be generated with different methods such as ultrasonic transduction and peristaltic pumps. The droplets generation is a critical step as they act as nucleation centers which will evolve to the crystallized particles. Particles produced by spray pyrolysis have large surface area, high purity, and they can be smaller than 1 μm . The process starts with pumping or spraying of solution droplets with precursors in it into a pyrolysis furnace at around 400 – 600 $^{\circ}\text{C}$ by a carrier gas. The collected precursor powder is then calcined at 700 – 800 $^{\circ}\text{C}$. Metal dopants have been used in spray pyrolysis and carbon sources can be added during spray pyrolysis to produce LFP/C particles which increase the specific surface area of the powder. Process times under one minute can be achieved with spray pyrolysis.³⁵ Figure 29 shows synthesis with spray drying method.

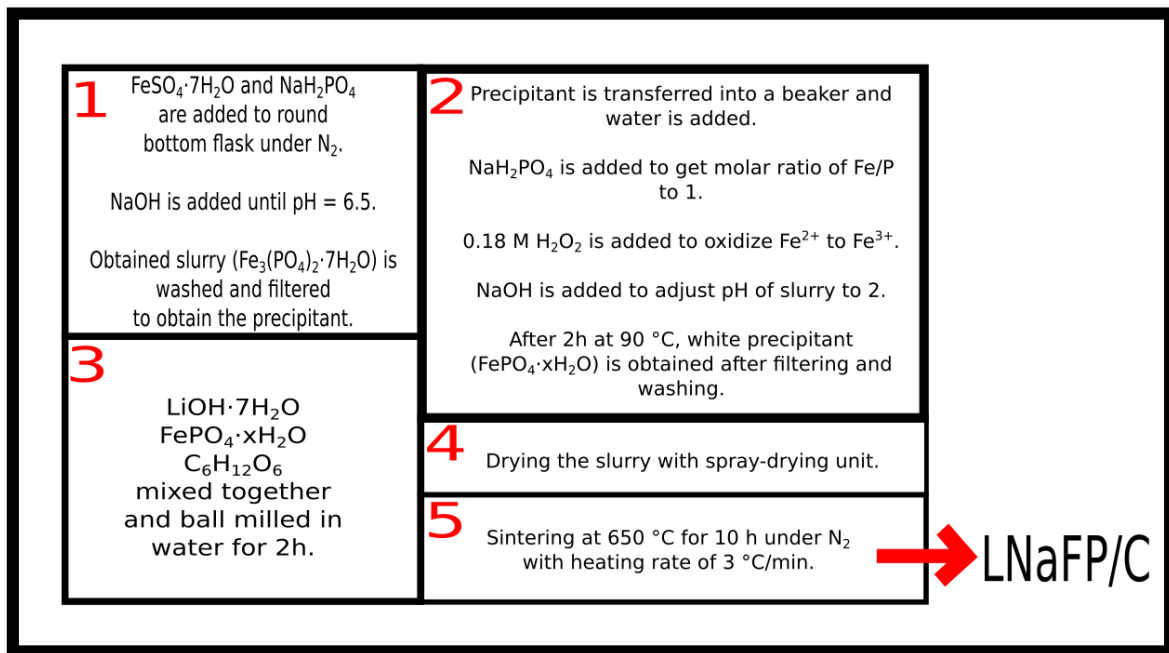


Figure 29. Wang *et al.* synthesized Na-doped LiFePO_4/C with precipitation method combined with spray drying method.⁴⁹

6.2.4 Co-precipitation

In co-precipitation the reagents are mixed while pH of the solution is controlled to allow precipitation of LFP precursors. The final LFP powder is obtained by calcination afterwards.³⁵ The pH and temperature conditions of co-precipitation are not often specified in the research papers. According to He *et al.* LiFePO_4 can be obtained at 298 K and $\text{pH} = 0 - 11.3$, with optimal precipitation occurring at $\text{pH} = 8 - 10.5$. $\text{Fe}_3(\text{PO}_4)_2 \cdot 8 \text{H}_2\text{O}$ and Li_3PO_4 are intermediates that have to be formed to produce LFP. At low temperature the rate of phase transformation is low and LFP production is therefore difficult.⁵⁰

6.2.5 Micro emulsion drying

LFP can be synthesized by drying micro emulsion solutions which are thermodynamically stable mixtures containing water, oil, and emulsifying agent that stabilizes the micro emulsions. The process starts by making microemulsion by mixing aqueous phase with organic oily phase. The microemulsions are then mixed, matured, dried, and usually calcinated.³⁵

6.3 Novel and rare synthesis methods

LFP or doped LFP can also be synthesized with pulsed laser deposition, template technology,⁵¹ glass-ceramic technique,⁵² and biomineralization.⁵³ In biomineralization living organisms are used to produce minerals. Article by Hou *et al.* is one example of biomineralization used for LFP synthesis. According to the article, FeCl_3 and MnCl_2 were added to purified yeast solution where the cells accumulated metal cations by biosorption for 4h. Then $(\text{NH}_4)_2\text{HPO}_4$ was added with continuous stirring for 30 minutes. Then pH was adjusted with CH_3COONa to 5 and the solution made was kept overnight to deepen the biomineralization process. The solution was centrifuged and washed with deionized H_2O and dried in vacuum freeze-drying machine. The precursor was mixed with Li_2CO_3 and regular presintering and sintering was done.⁵³

are more easily obtained through synthesis. Smaller band gap corresponds to higher electronic conductivity which enables better rate performance (fast charge and discharge).^{54,55} Using aforementioned properties theoretical screenings have been made for transition metal dopants. Zhang *et al.* screening results predicted Mn-, V-, Ni-, Rh-, and Os-doped LFP to have good electrochemical properties.⁵⁵ Other factors that should be considered include the price of the elements used in doping, the elements abundance, and environmental impact. We are going to see as we go through the studies that most dopants are used in low concentrations, usually replacing only 1% - 3% of Fe in LFP. This means that even quite expensive dopants would be viable if the enhanced electrochemical performance is deemed worth the increase in price.

It was already mentioned on Chapter 5 that doped LFP is a p-type semiconductor. This is because Fe is in oxidation state of +II in LiFePO_4 and most dopants are transition metals with possible oxidation states ranging from +II to +VI. In FePO_4 , Fe is in the oxidation state of +III. The fact that LFP is semiconductor also leads to lower conductivity at lower temperatures as less electrons have sufficient thermal energy to break loose from their bonds.¹⁹ Adding p-type impurities to n-type LFP will first lower electric conductivity because of reduction of electrons. At a certain point however, LFP transforms to p-type semiconductor and the hole concentration starts to rise which leads to increased conductivity. Too much dopant will lead to lattice distortion that may block the Li^+ diffusion channels.⁵⁶ Doping with cations with different charge from the parent ion (Li^+ or Fe^{2+}) is known as **aliovalent doping**.⁵⁷ **Supervalent dopants** include dopants with oxidation state 4^+ and 5^+ .⁵⁸

Polaron is a term used to define unit formed by an excess electron or a hole localized within a potential well, self-generated by displacing the surrounding ions.⁵⁹ In LFP electron mobility is highly complex phenomenon where LFP exhibits **polaron hopping** behaviour,⁶⁰ rather than band-like conduction. It seems that both the mechanics of conduction in LFP and how doping affects the conductivity are under debate. Some studies attribute the enhanced performance via cation doping to increased concentration of polarons and others to change in conduction mechanism from polaron hopping to band-like conduction.⁵⁷ Conductivity can also be increased by introducing Li vacancies.⁶⁰

Many details affect the performance of the active material. Table 4 has collection of details that should be considered during LFP synthesis, modifications, and analysis.

Table 4. Summarizing synthesis, modifications, and how they are characterized.

Detail	Note	Ref
Li ₃ PO ₄ impurity	Can increase ionic conductivity but can also lower performance.	61,62
Fe ₂ P impurity	Can increase conductivity but can also lower capacity.	61,62
H ₂ as reductive gas	Prevents Fe ²⁺ oxidation during sintering.	63
Nanosized particles	Increased conductivity and diffusion by shorter distances. May lower tap density. Increased surface area leads to increased rate capability.	35,39,64
Carbon coating	Increased conductivity and diffusion by lowering interfacial resistance. Can inhibit particle size growth. Lowers volumetric energy density.	35,56,64
n-type doping	Raises (free) electron concentration and thus contributes to conductivity.	65
p-type doping	Hole conduction must first overcome free electrons in LFP to increase conductivity. Too much doping can lead to lattice distortion.	56
Shortening of b-axis	Most diffusion occurs through b-axis and shortening of the axis results to faster diffusion.	34
Doping effects in general	Hybridization of orbitals due to existence of f-orbitals, shortening of b-axis, shortening of band gap, increased phase transformation kinetics, and formation of desirable morphology.	64,65
Smaller interval between oxidization- and reduction peak in CV	Smaller interval indicates better reversibility of a reaction.	66
Li-site doping	Can block lithium ion migration but can also enhance conductivity.	60
Small concentration in doping (~3%)	Most of the time only small mole concentration of (~3%) of dopant is needed for increased performance.	58,67
Excess lithium	Excess lithium can be added in synthesis to compensate losses during calcination.	68

7.2 Alkali metal doping

7.2.1 Sodium

Liu *et al.* synthesized LFP doped with Na⁺ (Li_{1-x}Na_xFP) by solvothermal synthesis. The LNaFP/C had increased Li⁺ conductivity ($1.23 \cdot 10^{-15}$ cm²/s) compared to LFP/C's ($3.44 \cdot 10^{-15}$ cm²/s). Lattice expansion occurred as Na⁺ (0.97 Å) ions are larger than Li⁺ (0.68 Å). The lattice structure stayed the same as in LFP. Lattice vector b was significantly reduced increasing the Li⁺ conductivity. Na doping had no significant effect on particle morphology. The Na⁺ ions probably didn't intercalate/deintercalated like Li⁺ ions as the initial discharge capacities were reduced by doping Na⁺. The Na⁺ seemed also less active than Li⁺ as the capacity decay was lower and capacity retention of 86.7% at 10 C was achieved after 500 cycles. The sample doped with 1% Na⁺ had larger discharge capacity and better rate performance than the LFP/C sample or the sample doped with 5% Na⁺ at high current densities (1C, 2C, 5C, and 10C) and LFP/C was better at 0.1 C.⁶⁹

Wang *et al.* synthesized ultra-high rate LiNa_{0.01}Fe_{0.99}PO₄/C with excellent cyclability using sodium salt process via a facile precipitation method coupled with spray drying technology. The lattice volume was increased via doping. The morphology of the material was bowl-like. The Na⁺ was assumed to occupy Li⁺ sites although the formula mentioned before might suggest otherwise. The doped sample exhibited discharge capacity of 119 mAh/g at 40 C and good cyclability having 60.3 % of its initial capacity at 3000 cycles at 10 C. The tap density of the composite was relatively low at ~0.95 g/cm³ because of its porous structure. The lithium diffusion coefficient was increased to $1.35 \cdot 10^{-13}$ cm²/s and charge transfer resistance was significantly reduced.⁴⁹

7.2.2 Potassium

Fang *et al.* synthesized $\text{Li}_{1-x}\text{K}_x\text{FePO}_4/\text{C}$ by carbo thermal reduction method. The $\text{Li}_{0.97}\text{K}_{0.03}\text{FePO}_4/\text{C}$ sample exhibited the best electrochemical properties. The initial discharge capacity was 153.7 mAh/g at 0.1 C and the capacity retention was 92 % after 50 cycles above 1 C. At 10 C discharge capacity was 76.4 mAh/g. Increase in lattice parameters occurred which could provide more space for Li^+ intercalation/deintercalation and increase the diffusion pathways. Increase in electronic conductivity was also measured from $7.28 \cdot 10^{-3}$ to $1.01 \cdot 10^{-2}$ S/cm between the undoped LFP and best doped sample. Slight increase in Li^+ diffusion coefficient was also measured.⁴³

7.3 Alkaline metal doping

7.3.1 Magnesium

In a study of Yang *et al.* Mg²⁺ doped LiFePO₄/C was produced via improved solid-state reaction without ball milling. LiCH₃COO·2H₂O, Mg(CH₃COO)₂·4H₂O, ascorbic acid, and homemade amorphous FePO₄ nanoparticles were used as raw materials. The FePO₄ was added last to the solution containing other materials. **Excess lithium was added to compensate for Li loss during calcination. Ascorbic acid acts as reductant reducing Fe(III) to Fe(II) and as a source for carbon for carbon coating of LFP.** The synthesis can be divided into three parts: mixing and evaporation, pre-calcination, and calcination. The synthesis is shown in Figure 31.⁶⁸

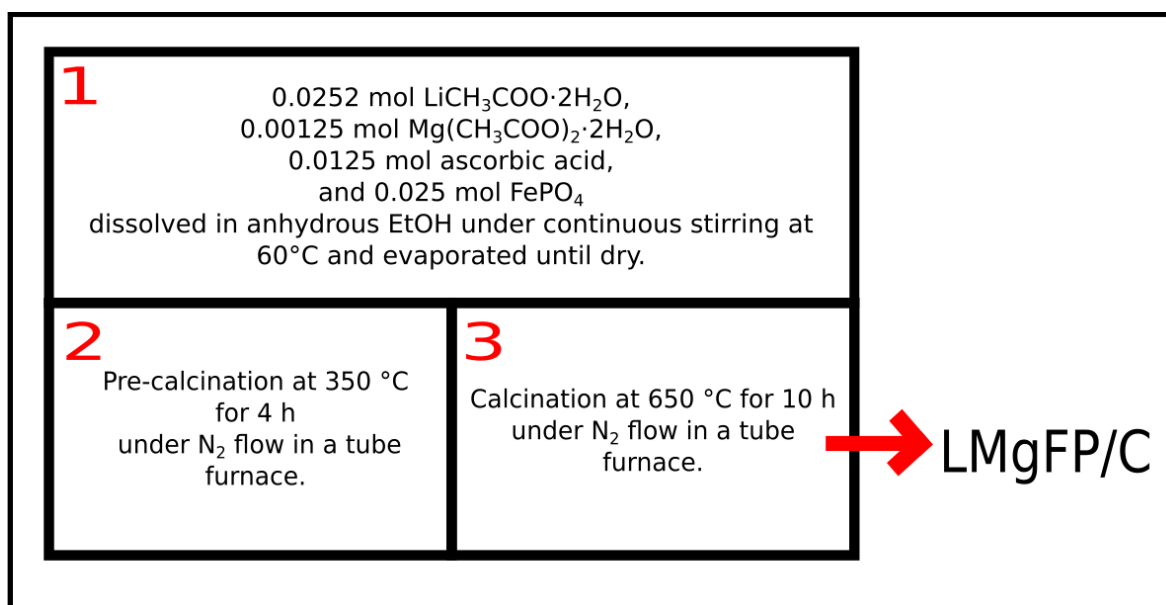


Figure 31. Yang *et al.* synthesized Mg-doped LiFePO₄/C via solid state route.⁶⁸

7.3.2 Calcium

Ting-Kuo Fey *et al.* synthesized LiFe_{1-x}Ca_xPO₄/C ($x = 0 - 0.014$) composites via solid-state method. The unit cell volume increased by a little (~0.2 %) which can be attributed to the larger size of Ca²⁺ compared to Fe²⁺. The sample with 1 mol% Ca had the highest conductivity ($5.48 \cdot 10^{-3}$ S/cm) and best electrochemical performance. The Li⁺ diffusion coefficient was calculated to be $4.59 \cdot 10^{-3}$ cm²/s. Increased conductivities led to increased reversible capacities of 120 mAh/g at 1 C and 80 mAh/g at 10 C and discharge capacity of 149 mAh/g at 0.2 C.⁷⁰

7.4 Transition metal doping

7.4.1 Titanium

Wu *et al.* produced Ti^{4+} -doped $\text{LiFe}_{1-x}\text{Ti}_x\text{PO}_4$ ($0 \leq x \leq 0.09$) via solution route. Interestingly Ti^{4+} -doping increased the lattice values although Ti^{4+} has smaller radius than Fe^{2+} . The results by Wu *et al.* suggest that Ti^{4+} doping did not occur on iron sites. The sample with 3% Ti doping exhibited highest reversible capacity (126 mAh/g) and it was attributed to the largest b and c parameters, enabling faster Li^+ diffusion. The study seemed that Ti^{4+} doping lowered the capacity compared to pure LFP prepared in the study (131 mAh/g). This probably stemmed from the particle size, composition, and thickness of the cathodes prepared for testing.⁷¹

However, many other studies suggest positive results. Wang *et al.* synthesized Ti, Mg, and Zr doped nanosized LFP crystals ($\text{LiTi}_{0.01}\text{Fe}_{0.99}\text{PO}_4$) in the 40 to 150 nm range with sol-gel method with near full capacity of 170 mAh/g in 2004. The Ti doped sample and the pure LFP sample both exhibited stable discharge capacity of 160-165 mAh/g at a rate of C/8.⁷² The synthesis is shown in Figure 32.

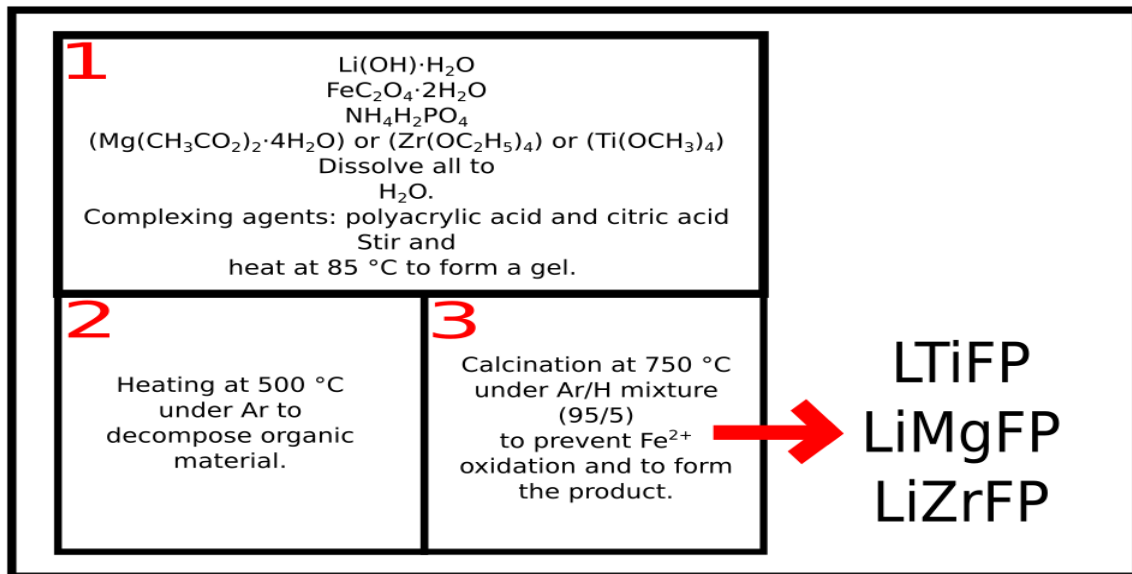


Figure 32. Sol-gel route of Wang *et al.* to Mg-, Ti-, and Zr-doped LiFePO_4 .⁷²

Kim *et al.* used solid-state method to produce $\text{LiTi}_{0.08}\text{Fe}_{0.92}\text{PO}_4$ with high rate capability as specific capacities of 160 mAh/g at 0.2 C and 110 mAh/g at 11.4 C were retained. The XRD pattern of the doped sample showed peaks corresponding to $\text{Li}_3\text{Fe}_2(\text{PO}_4)_3$, $\text{Li}_2\text{TiFe}(\text{PO}_4)_3$, and TiO_2 phases. These phases (except TiO_2) may improve conductivity in Ti-doped LFP. The lattice parameters decreased by Ti

doping. Ti^{4+} has smaller radius (74.5 pm) than Fe^{2+} (92 pm). Kim *et al.* thought that this may result in atomic and electronic structure variation that improves electrical conductivity.⁴¹ See Figure 22 on page 37 for the synthesis.

Gao *et al.* produced titanium nitride (TiN) coated LFP **with atomic layer deposition (ALD)**. During the coating Ti doping occurred simultaneously. The synthesis of LFP particles was not described in the work. In ALD chemical precursors are sequentially introduced to the surface of the material that is coated. In this work TiN, titanium tetrachloride (TiCl_4), and NH_3 were used. ALD produces uniform coating with precise control of the coating thickness. It also works on challenging materials but can be costly. The material exhibited increased capacity of ~159 mAh/g from the capacity of uncoated LFP at ~150 mAh/g. It seemed that 5 cycle coating process was better than 10 cycles as the Li diffusion was inhibited in the sample with more cycles. More cycles lead to more layers of coating. The cycling stability of the sample was superior compared to the uncoated LFP. Capacity retention of the TiN coated LFP was ~89% at 1,000 cycles. For the uncoated LFP deterioration started to occur already at 500 cycles.⁷³

7.4.2 Vanadium

Chiang *et al.* synthesized V-doped LFP ($\text{Li}_{1-x-v}\text{V}_x\text{FePO}_4$) with modified sol-gel method. The capacity increased from 138 mAh/g to 155 mAh/g and the conductivity increased from $4.75 \cdot 10^{-4}$ S/cm to $1.9 \cdot 10^{-2}$ S/cm compared to the pristine LFP counterpart. Enhanced capacity and conductivity were observed when V was added less than 2% ($x < 0.02$). Impurity of LiV_2O_5 emerged when the concentration was higher. The V was substituted to Li sites and produced vacancies (v) to Li sites. The lattice parameters saw no significant change. Figure 33 below shows the details of the synthesis.⁷⁴

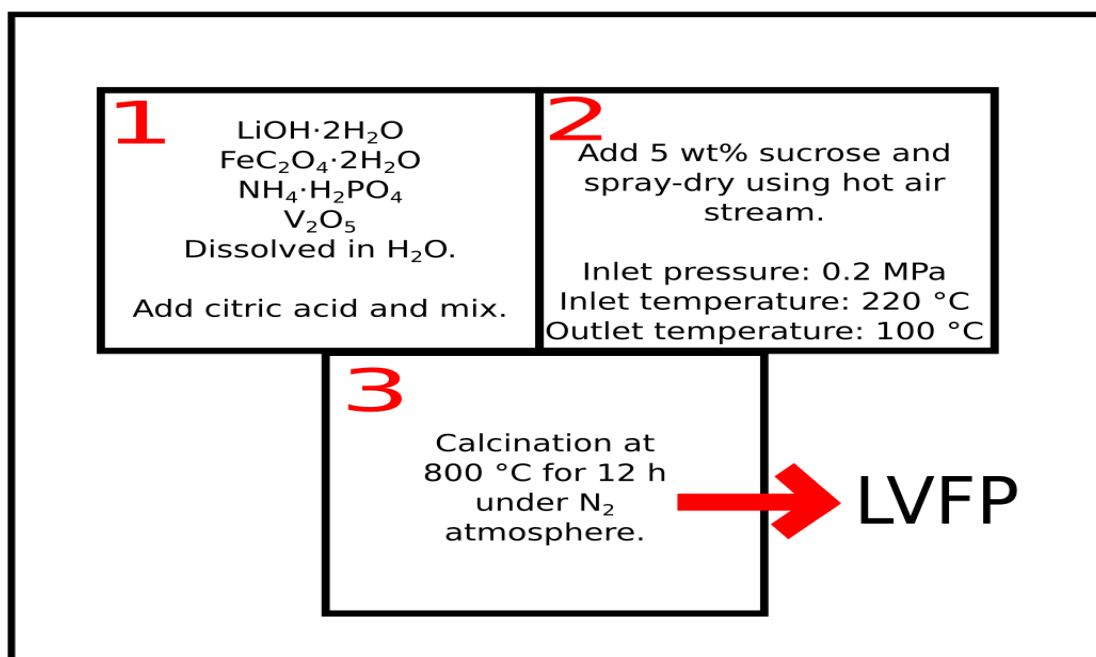


Figure 33. Chiang *et al.* synthesized V-doped LiFePO_4 by modified sol-gel method.⁷⁴

Jiang and Wang synthesized V-doped LiFePO_4/C with sol-gel method. No change in crystal structure was observed for doped samples. Particle size for doped samples was lower than for the undoped sample (< 140 nm). $\text{LiFe}_{0.97}\text{V}_{0.03}\text{PO}_4/\text{C}$ sample exhibited the best electrochemical performance with 112.7 mAh/g capacity at 10 C after 200 cycles. Electrical conductivity was reported to be $5.9 \cdot 10^{-4}$ S/cm. Raman spectrometry suggested existence of $\text{Li}_3\text{V}_2(\text{PO}_4)_3$ phase.⁶⁷

7.4.3 Chromium

Shin *et al.* synthesized $\text{LiFe}_{0.97}\text{Cr}_{0.03}\text{PO}_4/\text{C}$ by mechanochemical process and heat treatment. The doped sample had bigger particle size (100 nm) than the pristine LFP (73 nm) and LFP/C (95 nm). It is suggested that carbon coating inhibited particle growth because the LFP/C sample had similar particle size to the doped sample. The doped sample had initial discharge capacity of 151.5 mAh/g and the LFP/C had 149.5 mAh/g. The doped sample exhibited better performance at 10 C as it maintained high capacity of 120 mAh/g. The doped material had smaller unit cell than the carbon doped and pristine counter parts.⁷⁵ However, other studies have demonstrated that Cr-doping blocks Li^+ -diffusion, although conductivity is increased.⁷⁶

7.4.4 Manganese

LiMnPO_4 (LMP) is one of the materials in the lithium metal phosphate family LiMPO_4 , where $\text{M} = \text{Fe}, \text{Mn}, \text{Co}, \text{and Ni}$. LMP has the same crystal structure as LFP but higher theoretical energy density at 700 Wh/kg compared to energy density of LFP at 578 Wh/kg.⁷⁷ LMP has higher operating voltage than LFP at 4.1 V. On the other hand pure **LMP has even worse electrical conductivity than LFP** at $<10^{-10}$ S/cm and Jahn-Teller distortion occurs during LiMnPO_4 charge/discharge process which hinders lithium removal and uptake resulting to large changes in volume.¹⁸ This means that the structure is not stable. Doping LFP with Mn^{2+} ions is probably the most common way to dope LFP and yields $\text{LiFe}_{1-y}\text{Mn}_y\text{PO}_4$ (LMFP) that combines the high safety of LFP and the high energy density of LMP. LMFP's structure is similar to LFP. It has octahedrons consisting of M-O , where $\text{M} = \text{Fe}, \text{Mn}$ and the octahedron is isolated by P-O tetrahedron and no continuous metal-oxygen network forms leading to low conductivity. The diffusion of Li^+ also happens through one dimensional channels which makes it slow.⁷⁷ Increase in average working voltage can be achieved by Mn^{2+} doping but it creates a sudden voltage drop as Mn^{2+} oxidizes at different voltage compared to Fe^{2+} . This is not ideal for most electronics.¹ However, the Mn^{2+} ions widen the diffusion channels as it has bigger radius than Fe^{2+} enhancing the mobility of Li^+ ions.⁷⁸

Many studies have been made on the different Fe to Mn ratios of LMFP. Some studies indicate that the optimal material is in the range of $\text{LiFe}_{(0.75-0.85)}\text{Mn}_{(0.15-0.25)}\text{PO}_4$. Other studies indicate that materials with higher Mn percentage perform

better. It seems that the optimal ratio of Fe to Mn depends on the synthesis method, carbon coating degree, and raw materials.⁷⁷ There is many ways to synthesize LMFP. Common ones include **sol-gel synthesis**, **hydrothermal/solvothermal synthesis**, **spray pyrolysis**, and **solid-state synthesis**. Sol-gel synthesis is the simplest synthesis method and can be easily reproduced. It produces powders with high purity, uniform structure, and small particles size. Small amount of dopant can be uniformly dispersed into final product and low temperature can be used.⁷⁸

Ultrahigh rate capabilities have been achieved by Hu *et al.* via 3D-printed electrodes from $\text{LiMn}_{1-x}\text{Fe}_x\text{PO}_4$ nanocrystals synthesized with reflux process and carbonization. The $\text{LiMn}_{0.21}\text{Fe}_{0.79}\text{PO}_4@\text{C}$ had particles size of 40-44.7 nm and discharge capacities of 161.36 to 108.45 mAh/g at rates of 1 C to 100 C. **The material also had excellent cyclability as the reversible discharge capacities remained at 150.21 and 140 mAh/g after 1000 cycles at rates of 10 C and 20 C with almost no capacity decay. These numbers were the highest recorded for LMFP LIBs in 2016.** In comparison, traditional electrode had capacities of 103.38 and 90.64 mAh/g at same rates.¹³

7.4.5 Cobalt

Cobalt is a raw material that is used a lot in different LIB chemistries. These include LiCoO_2 (LCO), $\text{LiNi}_x\text{Mn}_y\text{Co}_z\text{O}_2$ (NMC), $\text{LiNi}_x\text{Co}_y\text{Al}_z\text{O}_2$ (NCA), and the LiCoPO_4 (LCP) that belongs to the same olivine family as LFP. LCP has high operating voltage of ~4.8 V, high theoretical capacity of ~167 mAh/g and higher energy density than LFP at ~800 Wh/kg. However, cobalt is more expensive than iron, and LCP has unsatisfactory cycle life and rate performance. The higher operating voltage can also decompose electrolytes.⁷⁹ These are some of the reasons why LCP is not as widely used as LFP.

Gao *et al.* synthesized Co-doped LFP via sol-gel method. $\text{LiCo}_{0.01}\text{Fe}_{0.99}\text{PO}_4/\text{C}$ sample exhibited best rate performance with discharge capacity of 114.8 mAh/g at 10 C at and 104.2 mAh/g at 20 C. Capacity retention after 20 cycles at 20 C was 98.75 %. Decrease in lattice parameters was attributed to the smaller radius of Co^{2+} . Doped samples had higher electrical conductivities than pure LFP and $\text{LiCo}_{0.01}\text{Fe}_{0.99}\text{PO}_4/\text{C}$ had second highest at $5.46 \cdot 10^{-4}$ S/cm, lower compared to

$\text{LiCo}_{0.02}\text{Fe}_{0.98}\text{PO}_4/\text{C}$ at $6.53 \cdot 10^{-4}$ S/cm. However, 0.02 Co-doped sample had larger particle size that probably attributed to worse electrochemical performance.⁸⁰

7.4.6 Nickel

Örnek *et al.* synthesized nano-sized, carbon coated, and nickel doped $\text{LiNi}_{0.05}\text{Fe}_{0.95}\text{PO}_4/\text{C}$ with high initial discharge capacity of 155 mAh/g at 0.2 C via sol-gel assisted carbothermal reduction. The material had also good capacity retention of 99.1 % over 100 cycles and higher conductivity than its undoped counterpart. The electrochemical properties seem to decline when the share of Ni exceeds 0.05 mol in LFP. The unit cell volume on the other hand went down as the Ni content increased.⁸¹ The synthesis is shown in Figure 34.

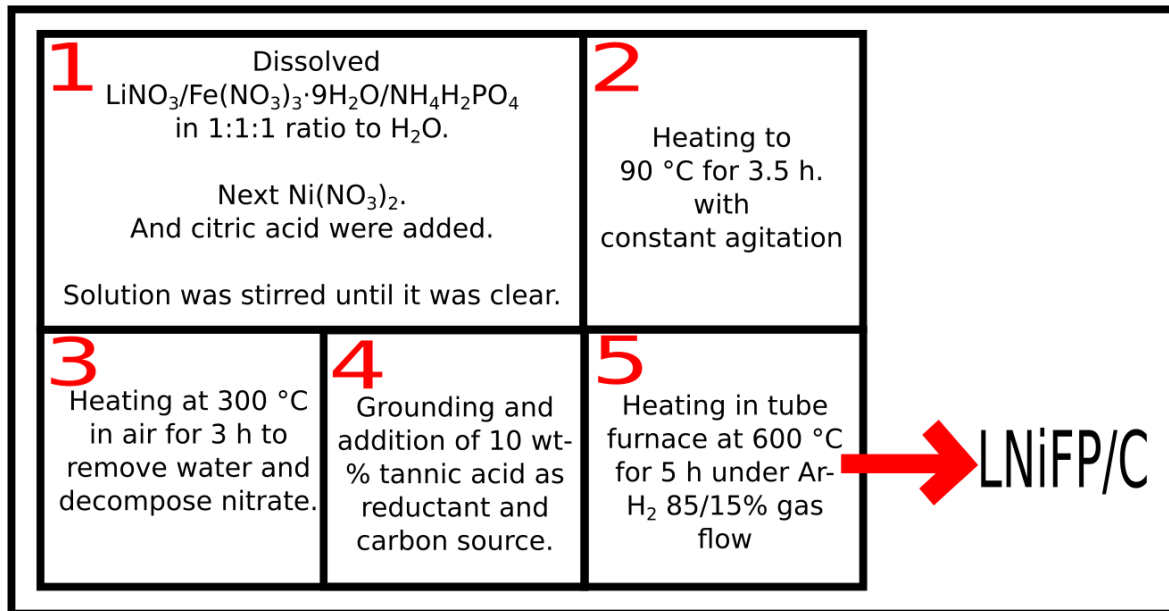


Figure 34. Örnek *et al.* synthesized Ni-doped LiFePO_4 with sol gel assisted carbothermal reduction.⁸¹

Liu *et al.* synthesized Ni-doped $\text{LiNi}_x\text{Fe}_{1-x}\text{PO}_4/\text{C}$ via spray drying-carbothermal method. $\text{LiNi}_{0.03}\text{Fe}_{0.97}\text{PO}_4$ sample exhibited capacity of 135.5 mAh/g at 5 C, which was 50% higher than that of pristine LFP prepared by same method. The sample had the largest a, c, and V lattice values indicating widest Li^+ pathway. b value on the other hand was the smallest indicating shortest Li^+ diffusion distance. The sample also had smallest potential interval between oxidation and reduction peak, largest peak current, higher peak discharge potential, and lower peak charge potential in CV. The doped sample exhibited particles that were microsphere (1-5

µm) aggregates of nanosized primary particles that are considered superior structure for cathode materials.⁶⁶

7.4.7 Copper

Chang *et al.* produced $\text{LiFe}_{1-x}\text{Cu}_x\text{PO}_4/\text{C}$ materials with high tap density and nanosized particles (100-300 nm) via solid-state route. The $\text{LiFe}_{0.98}\text{Cu}_{0.02}\text{PO}_4/\text{C}$ sample had high tap density of 1.98 g/cm^3 and a discharge capacities of 150 mAh/g and 127.3 mAh/g at 0.1 C and 2 C respectively. Although the capacities were not that high the high tap density lead to volumetric capacities of 297 mAh/cm^3 and 252 mAh/cm^3 . The study indicates that higher Cu concentrations than 2% can replace Li in the LFP crystal lattice leading to worse electrochemical performance.⁸²

7.4.8 Zinc

Liu *et al.* reported Zn-doped LiFePO_4 for the first time in 2006. Solid state method was used. Conductivity increase from $9.98 \cdot 10^{-14} \text{ cm}^2/\text{s}$ to $1.58 \cdot 10^{-13} \text{ cm}^2/\text{s}$ was reported between LiFePO_4 and $\text{LiZn}_{0.01}\text{Fe}_{0.99}\text{PO}_4$. Zn^{2+} radius does not change during de-intercalation process unlike Fe^{2+} that oxidizes to Fe^{3+} with smaller radius resulting into smaller lattice shrinkage compared to pure LFP. The lattice unit cell was reported to increase. Capacity of 133 mAh/g at 0.1 C was reported.⁵¹ Yiming *et al.* produced $\text{LiFe}_{1-x}\text{Zn}_x\text{PO}_4$ ($0 \leq x \leq 0.26$) with wet chemistry method. The unit cell volume decreased with increased Zn content. Particles in the 10 – 100 nm range were produced. Zn is less electroactive than Fe and thus the theoretical capacity of the material is lower than pure that of pure LFP. According to Yiming *et al.* more investigation is needed to find the optimal level of doping.⁸³

7.4.9 Niobium

Jiang *et al.* synthesized $\text{LiFe}_{0.95}\text{Nb}_{0.05}\text{PO}_4/\text{C}$ via sol-gel method with specific capacities of 157 mAh/g at 0.2 C and 85 mAh/g at 5 C. Smaller particles were reported for the doped sample and diffusion coefficient increased to $7.94 \cdot 10^{-12} \text{ cm}^2/\text{S}$.⁶¹

7.4.10 Molybdenum

Ma *et al.* synthesized Mo-doped $\text{LiMo}_{0.01}\text{Fe}_{0.99}\text{PO}_4/\text{C}$ via two-step ball milling solid-state reaction. No changes in crystal structure were reported. Increase in interplanar distance (d) was reported indicating wider Li^+ pathway. Particle size of about 200 nm was reported for the doped material with high tap density of 1.82 g/cm^3 . High tap density was achieved by filling of interspaces of bigger particles with smaller particles. The best doped sample $\text{LiMo}_{0.01}\text{Fe}_{0.99}\text{PO}_4/\text{C}$ exhibited discharge capacities of 114.4 mAh/g at 5 C and 82.9 mAh/g at 20 C. Charge-transfer resistance was cut nearly in half from 330.8 to 162.4 Ω .⁸⁴

7.4.11 Ruthenium

Gao *et al.* synthesized $\text{LiFe}_{0.99}\text{Ru}_{0.01}\text{PO}_4/\text{C}$ with surface assisted sol-gel method with increased electrical conductivity, Li-ion diffusion velocity, specific capacity, and rate capability. The capacity retention after 15 cycles at 0.1 C rate was 99.5%, the specific capacity was 162 mAh/g at 0.1 C and at 107 mAh/g at 10 C. The details for the synthesis are shown in Figure 35.⁸⁵

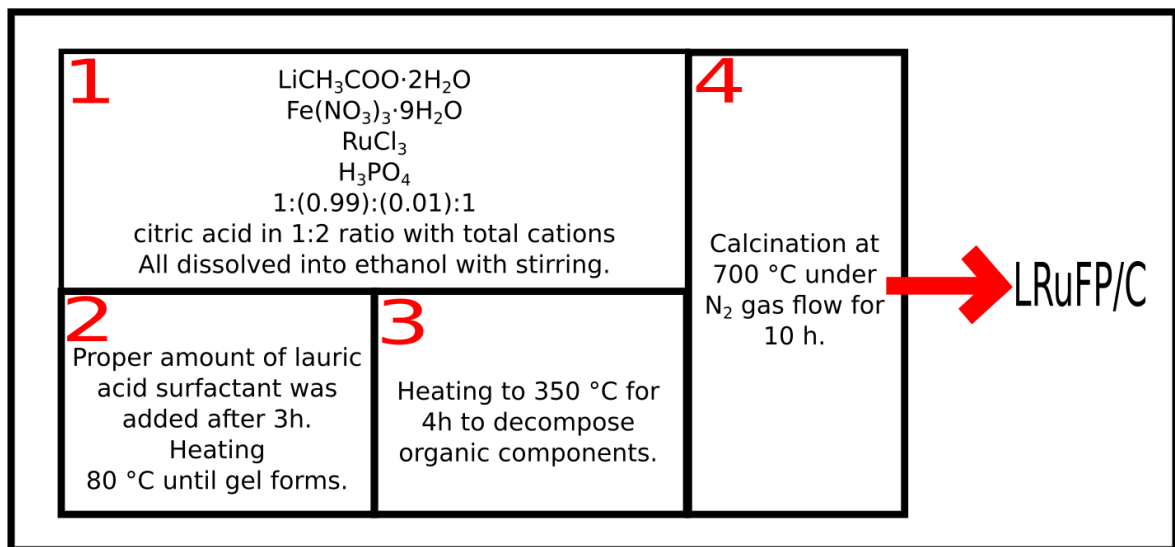


Figure 35. Gao *et al.* used surface assisted sol-gel method for Ru-doped LiFePO_4 synthesis.⁸⁵

Gao *et al.* believed the high rate capability came from combination of carbon coating, Li_3PO_4 and Fe_2P phases, small particles, and Ru doping which formed vacancies to Fe and Li sites.⁸⁵

7.4.12 Rhodium

Tong *et al.* synthesized Rh-doped LFP via carbothermal reduction. $\text{LiFe}_{0.975}\text{Rh}_{0.025}\text{PO}_4/\text{C}$ sample exhibited best performance having discharge capacity of 117 mAh/g at 10 C and great cyclability. Capacity remained as 135.4 mAh/g at 300th cycle at 55 °C at 1 C rate which was 82% of the initial capacity. Slight increase in lattice parameters was observed although Rh^{3+} ion is smaller than Fe^{2+} . Particle size of the doped materials was about 120 nm.⁸⁶

7.4.13 Palladium

Talebi-Esfandarani and Savadogo synthesized LFP doped with Pd via sol-gel method. Pd doping seems to induce formation of impurities like Li_3PO_4 which are inactive mass. Lattice shrinkage seemed to occur although Pd^{2+} has bigger radius than Fe^{2+} . This probably leads blocked diffusion channels as less space is available. Specific surface area decreased with more Pd doping. Low specific capacity of 107 mAh/g at 0.2 C was achieved for $\text{LiFe}_{0.96}\text{Pd}_{0.04}\text{PO}_4/\text{C}$. Palladium seems to be unsuitable dopant.⁸⁷

7.4.14 Tungsten

Arava *et al.* studied the effects of tungsten W^{6+} doping on Fe site in LFP synthesized with solid state reaction. The sample with 2% W doping and carbon coating had the highest charge capacity of 146 mAh/g at 0.1 C and 110 mAh/g at 1 C. The diffusion rate was also observed to increase to $8.82 \cdot 10^{-12} \text{ cm}^2/\text{s}$ from carbon coated LFP's $3.42 \cdot 10^{-12} \text{ cm}^2/\text{s}$ and pristine LFP's $10^{-14} \text{ cm}^2/\text{s}$. Minor increase in unit cell volume was observed.⁸⁸ The details of the synthesis are presented on Figure 36 below.

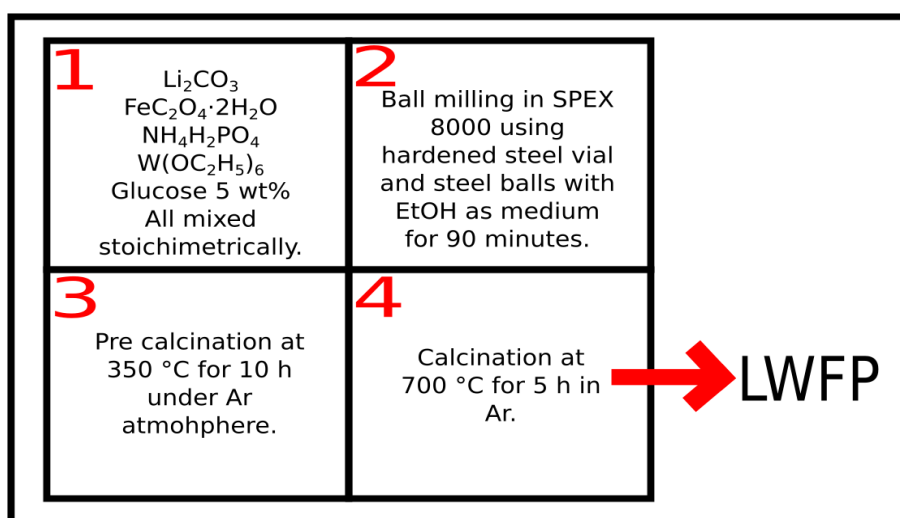


Figure 36. Arava *et al.* synthesized W-doped LiFePO_4 via solid-state route.⁸⁸

7.5 Post-transition metals

7.5.1 Aluminium

Kulka *et al.* prepared Al doped $\text{Li}_{0.97}\text{Al}_{0.01}\text{FePO}_4$ via ceramics method with worse electrochemical performance (96 mAh/g at 0.2 C) than the nanosized LFP counterpart (150 mAh/g). The crystallite size was about 300 nm for all samples and unit cell volume grew with increasing Al content.⁸⁹

7.5.2 Indium

Kumar *et al.* synthesized $\text{LiFe}_{0.99}\text{In}_{0.01}\text{PO}_4/\text{C}$ with sol-gel method. The best sample had discharge capacity of 142 mAh/g at 1 C and ~128 mAh/g at 10 C. The sample also had excellent cycling stability of 96 % after 250 cycles. Decrease in charge-transfer resistance was detected. Minor impurities of Fe_2P and Li_3PO_4 were detected with XRD. The conductivity was measured with Van der Pauw method and increase from $8 \cdot 10^{-2}$ to $1 \cdot 10^{-2}$ S/cm between undoped and doped sample. The Li-ion diffusion coefficient also increased from $4.5 \cdot 10^{-14}$ to $1.4 \cdot 10^{-13}$ cm^2/s . **The presence of conductive Fe_2P seems to enhance electrical conductivity.**⁶²

7.5.3 Tin

Hou and Tao studied the effects of Sn^{2+} , Sn^{4+} , and $\text{Sn}^{2+}/\text{Sn}^{4+}$ co-doping doping to LFP iron sites. Upon Sn doping new electronic states appear on the top of valence band (Sn^{2+}) and to the bottom of conduction band (Sn^{4+}) leading to decrease in band gap. The change was from pure bulk LFP (3.74 eV) to (1.50 V) of $\text{Sn}^{2+}/\text{Sn}^{4+}$ co-doped LFP. The decrease in band gap was highest for co-doping. High level Sn doping won't be beneficial as Sn is electrochemically inactive.⁹⁰

Ma *et al.* used sol-gel method to synthesize $\text{LiFe}_{0.97}\text{Sn}_{0.03}\text{PO}_4$ with excellent specific capacities of 146 and 128 mAh/g at 5 C and 10 C rates which were also higher than the capacities of pristine LiFePO_4 (119 and 107 mAh/g) prepared in the study. Both samples had carbon coating. The electric conductivity was also increased from $3.08 \cdot 10^{-4}$ to $3.47 \cdot 10^{-3}$ S/cm. No significant change occurred in lattice parameters. Particles size decreased from 71 to 60 nm. The synthesis is described in Figure 37 below.⁴⁷

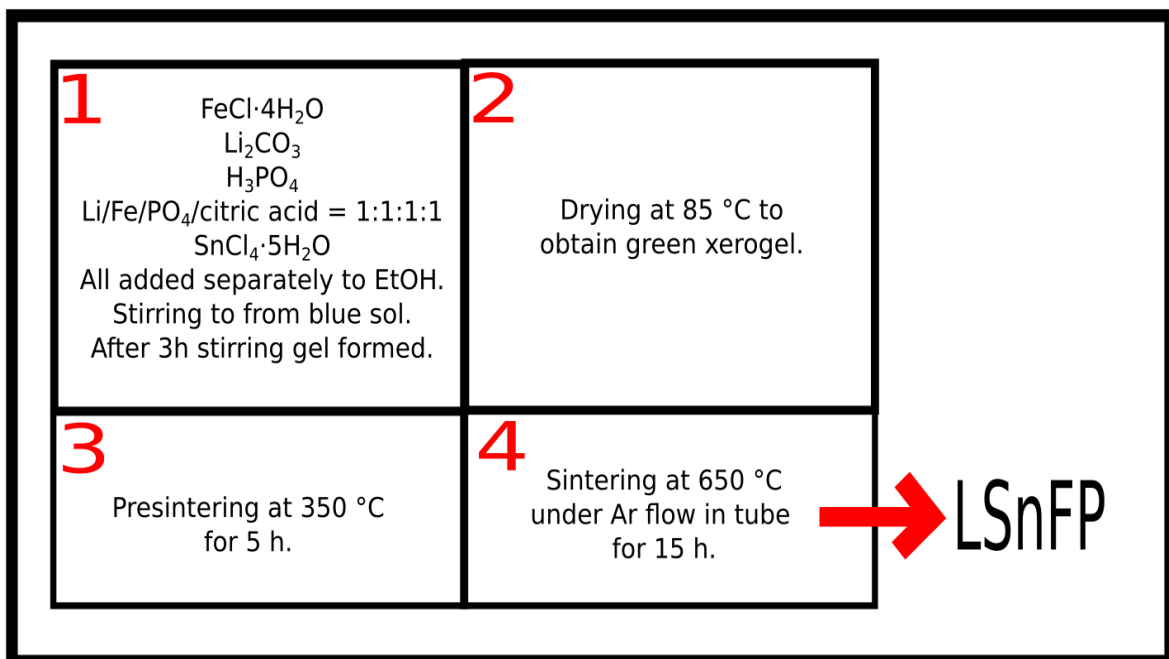


Figure 37. Sol-gel synthesis of Ma *et al.* to produce Sn-doped LFP.⁴⁷

7.6 Metalloid doping

7.6.1 Boron

Li *et al.* synthesized $\text{LiFeP}_{1-x}\text{B}_x\text{O}_{4-\delta}/\text{C}$ via solvothermal route. $\text{LiFeP}_{0.98}\text{B}_{0.02}\text{O}_{4-\delta}/\text{C}$ sample showed first discharge capacity of 138 mAh/g at 2C with no obvious capacity fade after 300 cycles. At 10 C the discharge capacity was reported to be 110 mAh/g. No impurities were detected with XRD. The smaller radius of B compared to P^{5+} resulted into smaller unit volume in doped samples. Crystal size decreased after B doping from 37.5 nm for virginal LFP to 32.4 nm for $\text{LiFeP}_{0.98}\text{B}_{0.02}\text{O}_{4-\delta}/\text{C}$. Grain size for doped sample ranged from 100 to 250 nm. Increase in Li^+ diffusion coefficient and electronic conductivity was also reported between LFP and $\text{LiFeP}_{0.98}\text{B}_{0.02}\text{O}_{4-\delta}/\text{C}$. More than 0.04 B doping resulted in oxygen defects which lead to decrease in active lithium.⁹¹

7.6.2 Silicon

Zhao *et al.* used solid state route to synthesize $\text{LiFeP}_{1-x}\text{Si}_x\text{O}_4/(\text{C} + y\text{Li}_2\text{SiO}_3)$, ($0 \leq x \leq 0.04$, $0 \leq y \leq 2\%$) composites with particle size of about 200 nm that had increased electrical conductivities. The sample with 0.03 Si and 1% Li_2SiO_3 exhibited the best rate capability at 158 mAh/g at 0.1 C and 121 mAh/g at 5C. Lithium-ion diffusion coefficient increased from $5.6 \cdot 10^{-13} \text{ cm}^2/\text{s}$ to $4.42 \cdot 10^{-12} \text{ cm}^2/\text{s}$ and charge-transfer resistance decreased. Li_2SiO_3 coating seems to increase rate capability only at higher rates.⁵⁶

7.6.3 Antimony

Full access to this article was not available but according to the abstract of the article by Fey *et al.* solid state method was used to synthesize Sb-doped $\text{LiFe}_{0.99}\text{Sb}_{0.01}\text{PO}_4/\text{C}$ that had discharge capacity of 154 mAh/g at 0.2 C.⁹²

7.7 Nonmetal and halogen doping

7.7.1 Sulfur

Okada *et al.* synthesized S-doped LFP/C nanoparticles (~100 nm) with solvothermal method. Increase in lattice parameters occurred as S^{2-} is larger than O^{2-} . The S doping increased the electrical conductivity and suppressed antisite defect (Fe occupying Li sites) formation which helps Li-ion diffusion. The doping occurred on the O-site and the LFP-S-0.22 sample had the best discharge capacity (112.7 mAh/g) of the samples at 10 C. Particles were about 100 nm in diameter.⁹³

7.7.2 Fluoride

Radhamani *et al.* used hydrothermal- and sol-gel methods to prepare F doped $LiFe(PO_4)_{1-x}F_{3x}$ ($0 \leq x \leq 0.4$) where F is substituted for O. The suppression of antisite defects was demonstrated with F doping by studying P-O stretching vibrational mode in FTIR spectra. Small changes occurred in lattice parameters.⁹⁴

Meng *et al.* synthesized F-doped LFP with N-, B-, and F-doped carbon. F-doped sample had discharge capacity of 123.9 mAh/g at 5 C and 71.3 mAh/g at 15 C. Increased diffusion and conductivity were reported.⁹⁵

7.7.3 Chloride

Liu *et al.* used solid state method to synthesize Cl-doped LFP/C by using pickling iron oxide red (Fe_2O_3) as Fe source. They also studied the optimal synthesis parameters and came to conclusion that the Li/Fe 1.03:1 ratio, sintering time of 4 h, sintering temperature of 650 °C, and having mass percentage of 80.25 wt% citric acid to Fe_2O_3 was optimal. Initial discharge capacity of 164.1 mAh/g at 0.1 C and a reversible capacity of 105.3 mAh/g at 10 C after 500 cycles was achieved for doped sample. Increase in Li^+ diffusion rate and electronic conductivity were both achieved.⁹⁶

7.7.4 Bromide

Zheng *et al.* synthesized Br-doped $LiFe(PO_4)_{(3-x)/3}Br_x/C$ via sol-gel method. Particle size was between 1-4 μm and the shape was irregular. Porous structure was induced by breakdown of citrate to water. Lattice volume increased via B^- doping. The best sample $LiFe(PO_4)_{(2.98)/3}Br_{0.02}/C$ had discharge capacity of 152 mAh/g at 0.2 C and 105 mAh/g at 1 C.⁹⁷

7.8 Rare earth element doping

7.8.1 Yttrium

Herrera *et al.* synthesized $\text{LiFe}_{1-x}\text{Y}_x\text{PO}_4$ with hydrothermal method. They showed that Y doping can increase lithium insertion degree and better cycling stability.⁹⁸

Yanwen *et al.* produced Y doped cathode materials with one being $\text{Li}_{0.99}\text{Y}_{0.01}\text{FePO}_4$ prepared with solid state method. The material had smaller grain size and increased initial discharge capacity (~ 130 mAh/g) and improved cycling performance.⁹⁹

7.8.2 Lanthanum

Cho *et al.* synthesized La^{3+} doped $\text{LiFe}_{1-x}\text{La}_x\text{PO}_4/\text{C}$ with solid-state method. The $\text{LiFe}_{0.99}\text{La}_{0.01}\text{PO}_4/\text{C}$ sample had the best maximum discharge capacity of 156 mAh/g at 0.2 C. The samples electronic conductivity was $2.82 \cdot 10^{-3}$ S/cm. It seemed that higher than 1 mol% dopant would result to lower discharge capacity. Samples were synthesized with varying amount of salicylic acid, which was source of carbon for coating, and the sample with 50 wt% of salicylic acid showed best electrochemical performance.⁶³

7.8.3 Cerium

Zhao *et al.* used solid state route to synthesize Ce^{3+} doped $\text{LiFe}_{1-x}\text{Ce}_x\text{PO}_4/\text{C}$ samples. The best sample $\text{LiFe}_{0.9}\text{Ce}_{0.1}\text{PO}_4/\text{C}$ delivered initial capacity of 155.4 mAh/g and possessed capacity retention of 99.6% after 100 cycles at 1 C. The capacity remained high at 136.7 mAh/g at 5 C. More than 10 mol% dopant resulted to worse electrochemical performance. Lattice parameters were higher for doped samples as Ce^{3+} has bigger radius than Fe^{2+} . The particle size decreased via doping.¹⁰⁰

7.8.4 Neodymium

Zhang *et al.* synthesized Nd-doped LFP/C via novel solid-state route without inert gas sintering as shown in Figure 38. Slight increase in lattice parameters occurred via Nd^{3+} doping providing more space for Li^+ intercalation/deintercalation. Carbon coating inhibited particle growth. The $\text{Li}_{0.99}\text{Nd}_{0.01}\text{FePO}_4/\text{C}$ sample exhibited improved performance compared to undoped samples. The doped sample had specific capacity of ~ 152 mAh/g. After 20 cycles at 0.5 C the discharge capacity remained at ~ 151 mAh/g for the doped samples.⁴⁰

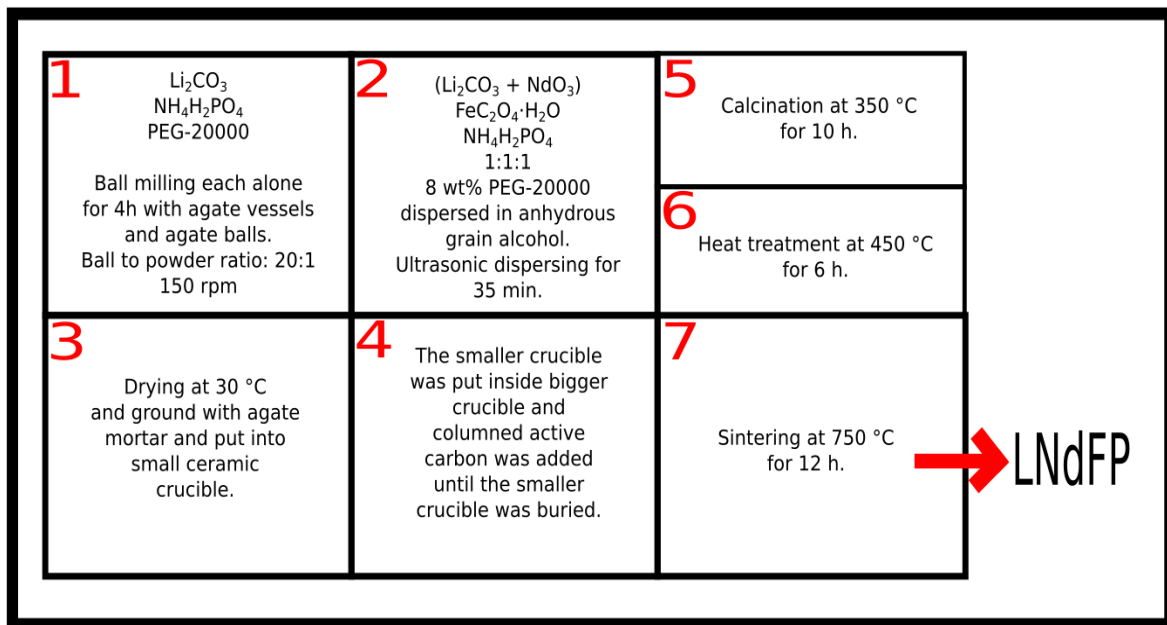


Figure 38. Novel synthesis route of Zhang *et al.* to produce Nd-doped LiFePO_4 .⁴⁰

7.8.5 Samarium

Meng *et al.* used sol-gel method to produce Sm^{3+} doped $\text{LiFe}_{1-x}\text{Sm}_x\text{PO}_4/\text{C}$ ($x = 0, 0.02, 0.04, 0.06, 0.08$). The $\text{LiFe}_{0.94}\text{Sm}_{0.06}\text{PO}_4/\text{C}$ sample had the highest discharge capacity (162.1 mAh/g at 0.1 C) within voltage range 2.5 – 4.2 V. The sample had high specific discharge capacity of 112.6 mAh/g at 10 C and average particle size of 150 nm, which was smaller than the pristine LFP prepared. Diffusion and conductivity were increased via doping. Charge-transfer resistance was lowered. The small amount of doping seemed to have no effect to the structure of LFP besides increasing lattice parameters.¹⁰¹

7.8.6 Europium

Altin *et al.* synthesized $\text{LiFe}_{1-x}\text{Eu}_x\text{PO}_4$ by glass-ceramics technique quenching. Eu doping induced $\text{Li}_3\text{Fe}_2\text{P}_3\text{O}_{12}$ impurities which were the lowest for the best sample $\text{LiFe}_{0.98}\text{Eu}_{0.02}\text{PO}_4$ that had capacity of 149.4 mAh/g at 0.5 C.⁵²

7.8.7 Gadolinium

Pang *et al.* synthesized $\text{LiFe}_{1-x}\text{Gd}_x\text{PO}_4/\text{C}$ via high temperature solid-phase reaction. Slight increase in unit cell parameters occurred for doped samples. The particle size was smaller for doped samples. The $\text{LiFe}_{0.93}\text{Gd}_{0.07}\text{PO}_4/\text{C}$ sample exhibited best electrochemical performance with maximum discharge capacities of 150.7 mAh/g at 0.2 C and 81.3 mAh/g at 10 C, initial discharge capacity of 80.4 mAh/g at -20 °C and 0.1 C. The discharge capacity decreased as the temperature decreased. This was attributed to polarization and slower Li^+ diffusion at lower temperature. The charge-transfer reactance (R_{ct}) decreased greatly.¹⁰²

7.8.8 Dysprosium

Göktepe synthesized $\text{LiDy}_{0.02}\text{Fe}_{0.98}\text{PO}_4/\text{C}$ in a solution medium. Both the undoped and doped sample were classified as orthorhombic *Pnma*. The volume of the unit cell increased slightly and electrical conductivity increased to $1.9 \cdot 10^{-2}$ S/cm. The doped sample had increased discharge capacity of 152.6 mAh/g at 0.1 C.¹⁰³

7.8.9 Holmium

Altin and Yolun synthesized Ho-doped $\text{LiFe}_{1-x}\text{Ho}_x\text{PO}_4$ ($x = 0, 0.01, 0.03, 0.05$) via solid-state reaction. The doped samples had smaller particles size than the pristine LFP prepared with 1 mol% doped sample having the smallest one. Best capacity value was obtained for the undoped sample but the 1 mol% and 3 mol% Ho-doped samples exhibited better cycling performance.¹⁰⁴

7.8.10 Erbium

Göktepe *et al.* synthesized Er-doped $\text{LiEr}_{0.02}\text{Fe}_{0.98}\text{PO}_4/\text{C}$ via solution-based method. It exhibited increased lattice volume and increased conductivity (from 10^{-4} to 10^{-2} S/cm). Er^{3+} ion has larger radius ($r = 0.104$ nm) than Fe^{2+} ($r = 0.074$ nm) which can explain lattice expansion. These factors led to increased initial capacity of 149 mAh/g at 0.1 C for the doped sample. Particle size and agglomeration also decreased compared to undoped LFP.¹⁰⁵

7.8.11 Ytterbium

Göktepe synthesized $\text{LiYb}_{0.02}\text{Fe}_{0.98}\text{PO}_4/\text{C}$ by solution-based method. The sample had smaller particle size, increased conductivity, and increased reversible capacity of ~146 mAh/g at 0.1 C.¹⁰⁶

7.9 Co-doping

7.9.1 Cerium and lanthanum

Zhang *et al.* synthesized La and Ce co-doped $\text{LiCe}_{0.015}\text{La}_{0.015}\text{Fe}_{0.97}\text{PO}_4/\text{C}$ with ultrahigh rate performance of 91.9 mAh/g at 200 C via solvothermal method. The sample exhibited high power density of 57.6 kW/kg at energy density of 300 Wh/kg. The Li^+ diffusion coefficient was calculated to be $7.09 \cdot 10^{-13} \text{ cm}^2/\text{s}$. N-type doping effect was indicated by X-ray photoelectron spectroscopy (XPS) and by electron density states. This changed the conduction type from p to n and lead to increased number of electrons on the conductive band. The doped sample had nanosphere and nanorod shaped particles with sizes of $\sim 10 \text{ nm}$ and $\sim 100 \text{ nm}$. Interplanar spacing also increased. The increase was attributed to the larger size of La^{3+} and Ce^{3+} ions compared to Fe^{2+} . Lower resistances of doped sample resulted to conductivity that was 5 orders of magnitude higher than that of the undoped sample.⁶⁵

7.9.2 Niobium and titanium

Tian *et al.* used sol-gel method to synthesize graphene (G) coated Nb- and Ti-doped $\text{Li}_{0.99}\text{Nb}_{0.01}\text{Fe}_{0.97}\text{Ti}_{0.03}\text{PO}_4/\text{G}$ with discharge capacity of 140.1 mAh/g at 5 C. Nb was assumed to locate to Li-site as the Nb^{5+} ion is smaller than Fe^{2+} and Ti^{4+} was attributed to Fe-sites because of the similar size to Fe^{2+} . b-axis of the crystal lattice shrunk resulting to shorter diffusion distance. The lattice volume increased despite of this. Graphene layer and doping both decreased the particle sized to an average of 155.6 nm. The doped sample had the best exchange current (0.284 mAh/g) implying best reversibility among the samples in the study. The electrical conductivity of LFP increased from $0.16 \cdot 10^{-3}$ to $0.89 \cdot 10^{-3} \text{ S/cm}$ between pristine LFP and LFP/G. The conductivity of doped LFP was $3.1 \cdot 10^{-3} \text{ S/cm}$.¹⁰⁷

7.9.3 Fluorine and vanadium

Li *et al.* synthesized V and F doped LiFePO_4/C via ball milling route with high-rate capacity of 124.9 mAh/g at 10 C with high capacity retention of 95.7 % after 100 cycles at 1 C. All lattice parameters increased. Electrolyte resistance and charge resistance both were lower for doped sample. Li^+ diffusion coefficient was increased to $3.58 \cdot 10^{-11} \text{ cm}^2/\text{s}$ for oxidation state. The doping affected Fe-site and PO_3 -site and the goal was to make a conducting cluster with mainly Li vacancies coupled with Fe and O ions.⁴²

7.9.4 Cobalt and zirconium

Gao *et al.* synthesized Zr and Co co-doped LFP via solid-state method. Cobalt was located on octahedral sites decreasing a and c lattice parameters but expanding b direction. However, Co^{2+} ions act as pillar to prevent collapse of crystal during intercalation and de-intercalation. Particle size was between 200 and 400 nm. $\text{Li}_{0.99}\text{Zr}_{0.0025}\text{Fe}_{0.99}\text{Co}_{0.01}\text{PO}_4$ sample showed best electrochemical performance having initial discharge capacity of 139.9 mAh/g at 0.1 C, remaining at 115.8 mAh/g after 50 cycles. Lithium diffusion coefficient was $3.8 \cdot 10^{-12} \text{ cm}^2/\text{s}$.⁶⁴

7.9.5 Sodium and chlorine

Wang *et al.* prepared Na^+ and Cl^- co-doped LFP/C via solid-state reaction. Co-doped sample had higher electrical conductivity ($1.1 \cdot 10^{-2}$) S/cm than pristine LFP and samples doped with only Cl^- or Na^+ . Na^+ was assumed to be at Fe^{2+} -site and Cl^- at O^{2-} -site. Li-O and P-O bonds for co-doped sample were longer than Na^+ -doped ones and shorter than Cl^- -doped ones. For Fe-O the case was exact opposite. Na^+ serves as a pillar in the structure, which can stabilize the crystal structure. Cl can also stabilize crystal structure by shortening the P-O bond length. Particle size was between 20-60 nm. Near 100% coulombic efficiency was achieved and increased capacity was achieved for co-doped samples. At 10 C, capacity was 115 mAh/g. Charge-transfer resistance was also reduced.⁷⁶

8 WHICH DOPANTS ARE THE BEST?

In this chapter materials with ultra high rate performance are coloured with green. These materials are classified as materials with discharge capacity over 100 mAh/g at +20 C in this thesis. High performance materials are coloured with blue, and exhibit discharge capacities of over 110 mAh/g at +10 C or over 120 mAh/g at 5 C. Yellow colour is used for materials with average capacity at high C-rate and for materials with good capacity at lower C-rates. Red colour is used for materials that had worse performance than their LFP counterpart and for materials with poor rate capabilities. Arrows pointing up (\uparrow) indicate increased performance compared to LFP counterpart and arrows pointing down (\downarrow) indicate worse performance compared to LFP counterpart. Lastly, other than performance factors are considered in Figure 39 where green, blue, yellow, and red are used to indicate best-, good-, mediocre-, and poor dopants. Table 5 includes capacity, conductivity, and Li-ion diffusion coefficient of alkali-, alkaline-, and post-transition metal dopants. We can see that Na-doped LFP has shown ultra high rate performance. Metalloids In and Sn have also shown great rate performance. In-doped LFP and Eu-doped LFP show the highest electrical conductivity (10^{-2} S/cm) of all the doped LFP materials presented here.

Table 5. Performance metrics of LiFePO₄ doped with alkali-, alkaline-, and post-transition metals.

Material	Specific discharge capacity and C-rate [mAh/g]	Electric conductivity [S/cm]	Li ⁺ diffusion coefficient [cm ² /S]	Synthesis method	Ref
LiNa _{0.01} Fe _{0.99} PO ₄ /C	119 40 C	\uparrow	$\uparrow 1.35 \cdot 10^{-13}$	precipitation and spray drying	⁴⁹
Li _{0.97} K _{0.03} FePO ₄ /C	76 10 C	$\uparrow 1.01 \cdot 10^{-2}$	$\uparrow 1.14 \cdot 10^{-15}$	carbothermal reduction	⁴³
Li _{0.95} Mg _{0.05} FePO ₄ /C	108 5 C	\uparrow	\uparrow	solid-state	⁶⁸
LiCa _{0.01} Fe _{0.99} PO ₄ /C	80 10 C	$\uparrow 5.48 \cdot 10^{-3}$	$4.59 \cdot 10^{-13}$	solid-state	⁷⁰
Li _{0.97} Al _{0.01} FePO ₄	\downarrow 95 C/5	-	-	ceramic	⁸⁹
LiIn _{0.01} Fe _{0.99} PO ₄ /C	128 10 C	$\uparrow 1 \cdot 10^{-2}$	$\uparrow 1.4 \cdot 10^{-13}$	sol-gel	⁶²
LiSn _{0.03} Fe _{0.97} PO ₄ /C	146 5 C	$\uparrow 3.47 \cdot 10^{-3}$	$\uparrow 2.89 \cdot 10^{-10}$	sol-gel	⁴⁷

From Table 6 we can see that metalloid, halogen and nonmetals produce materials with relatively good rate capabilities.

Table 6. Performance metrics of LiFePO₄ doped with metalloids, halogens, and nonmetals.

Material	Specific discharge capacity and C-rate [mAh/g]	Electric conductivity [S/cm]	Li ⁺ diffusion coefficient [cm ² /S]	Synthesis method	Ref
LiFeP _{0.98} B _{0.02} O _{4-δ} /C	110 10 C	↑ 1.86·10 ⁻⁵	1.38·10 ⁻¹⁴	solvothermal	⁹¹
LiFeP _{0.97} Si _{0.03} O ₄ / (C+1%Li ₂ SiO ₃)	121 5 C	↑	↑ 4.42·10 ⁻¹²	solid-state	⁵⁶
LiSb _{0.01} Fe _{0.99} PO ₄ /C	154 C/5	-	-	solid-state	⁹²
LiFePO _{3.78} S _{0.22} /C	113 10 C	↑	↑	solvothermal	⁹³
F-LFP@NBFC	124 5 C	↑	↑	hydrothermal	⁹⁵
LiFe(PO ₄) _{0.97} Cl _{0.01} /C	105 10 C	-	-	solid-state	⁹⁶
LiFe(PO ₄) _{2.98/3} Br _{0.02} /C	152 C/5	-	-	sol-gel	⁹⁷

All the LFP materials doped with elements close to Fe (Ti, V, Cr, Mn, Co, Ni) in the periodic table have shown good rate performances. Especially Mn-doped LFP. Rh-doped LFP also shows good performance as predicted by theoretical screenings.⁵⁵

Table 7. Performance metrics of LiFePO₄ doped with transition metals.

Material	Specific discharge capacity and C-rate [mAh/g]	Electric conductivity [S/cm]	Li ⁺ diffusion coefficient [cm ² /S]	Synthesis method	Ref
LiTi _{0.08} Fe _{0.92} PO ₄ /C	110 11.4 C	↑	↑	solid-state	⁷²
LiV _{0.03} Fe _{0.97} PO ₄ /C	117 10 C	↑ 5.9·10 ⁻⁴	-	sol-gel	⁶⁷
LiCr _{0.03} Fe _{0.97} PO ₄ /C	120 10 C	↑	-	mechanochemical	⁷⁵
LiMn _{0.21} Fe _{0.79} PO ₄ /C	108 100 C	↑	↑	reflux process and carbonization	¹³
LiCo _{0.01} Fe _{0.99} PO ₄ /C	115 10 C	↑ 5.46·10 ⁻⁴	↑ 1.04·10 ⁻¹¹	sol-gel	⁸⁰
LiNi _{0.03} Fe _{0.97} PO ₄ /C	94 10 C	-	-	spray drying and carbothermal reduction	⁶⁶
LiCu _{0.02} Fe _{0.98} PO ₄ /C	127 2 C	↑	-	solid-state	⁸²
LiZn _{0.01} Fe _{0.99} PO ₄ /C	133 C/10	-	↑ 1.58·10 ⁻¹³	solid-state	⁵¹
LiNb _{0.05} Fe _{0.95} PO ₄ /C	85 5 C	-	↑ 7.94·10 ⁻¹³	sol-gel	⁶¹
LiMo _{0.01} Fe _{0.99} PO ₄ /C	83 10 C	-	-	ball milling and solid state	⁸⁴
LiRu _{0.01} Fe _{0.99} PO ₄ /C	117 5 C	↑	↑ 7.15·10 ⁻¹²	surfactant-assisted sol-gel	⁶⁵
LiFe _{0.975} Rh _{0.025} PO ₄ /C	117 10 C	↑	↑	carbo thermal reduction	⁸⁶
LiPd _{0.02} Fe _{0.98} PO ₄ /C	↓ 109 5 C	-	↓	sol-gel	⁸⁷
LiW _{0.02} Fe _{0.98} PO ₄ /C	110 1 C	↑	↑	solid-state	⁸⁸

From Table 8 we can see that Ce- and Sm-doped LFP show the best high C-rate performance out of rare earth elements.

Table 8. Performance metrics of LiFePO₄ doped with rare earth elements.

Material	Specific discharge capacity and C-rate [mAh/g]	Electric conductivity [S/cm]	Li ⁺ diffusion coefficient [cm ² /S]	Synthesis method	Ref
Li _{0.99} Y _{0.01} FePO ₄	~130 -	-	-	solid-state/ball milling	⁹⁹
LiLa _{0.01} Fe _{0.99} PO ₄ /C	156 C/5	↑ 2.82·10 ⁻³	↑	solid-state	⁸³
LiCe _{0.1} Fe _{0.9} PO ₄ /C	137 5 C	↑ 5.93·10 ⁻²	↑	solid-state	¹⁰⁰
LiNd _{0.01} Fe _{0.99} PO ₄ /C	115 2 C	↑	↑	solid-state	⁴⁰
LiSm _{0.06} Fe _{0.94} PO ₄ /C	113 10 C	↑	↑ 1.25·10 ⁻¹³	sol-gel	¹⁰¹
LiEu _{0.02} Fe _{0.98} PO ₄ /C	149 C/2	↑	-	glass-ceramics quenching	⁵²
LiGd _{0.03} Fe _{0.97} PO ₄ /C	81 10 C	↑	↑	solid-state	¹⁰²
LiDy _{0.02} Fe _{0.98} PO ₄ /C	~110 2 C	↑ 1.9·10 ⁻²	↑	sol-gel	¹⁰³
LiHo _{0.01} Fe _{0.99} PO ₄ /C	~160 C/6	↑	↑	solid-state	¹⁰⁴
LiEr _{0.02} Fe _{0.98} PO ₄ /C	~105 2 C	↑ 10 ⁻²	-	sol-gel	¹⁰⁵
LiYb _{0.02} Fe _{0.98} PO ₄ /C	~146 C/10	↑ 1.9·10 ⁻³	-	sol-gel	¹⁰⁶

Table 9 shows that co-doping can produce LFP materials with great performances. La- and Ce co-doped LFP has ultrahigh rate performance that is much better than the LFP materials doped with just Ce or La presented in Table 8.

Table 9. Performance metrics of co-doped LiFePO₄.

Material	Specific discharge capacity and C-rate [mAh/g]	Electric conductivity [S/cm]	Li ⁺ diffusion coefficient [cm ² /S]	Synthesis method	Ref
LiCe _{0.015} La _{0.015} Fe _{0.97} PO ₄ /C	92 200 C	-	↑ 7.09·10 ⁻¹³	solvothermal	⁶⁵
Li _{0.99} Nb _{0.01} Fe _{0.97} Ti _{0.03} PO ₄ /G	140 5 C	↑ 3.1·10 ⁻³	-	sol-gel	¹⁰⁷
~Li _{0.97} V _{0.017} F _{0.058} FeP _{1.01} O _{3.99} C	125 10 C	↑	↑ 3.58·10 ⁻¹³	ball milling	⁴²
Li _{0.99} Zr _{0.0025} Fe _{0.99} Co _{0.01} PO ₄	140 C/10	-	3.8·10 ⁻¹²	solid-state	⁸⁴
LiFe _{0.99} Na _{0.01} PO _{3.99} Cl _{0.01} /C	115 10 C	↑ 1.1·10 ⁻²	↑	solid-state	⁷⁶

The performance metrics are not all that matters when developing battery materials. The abundance and price of the elements vary, and this affects the reasonability of some dopants. In Figure 39 we can see prices of most dopants.

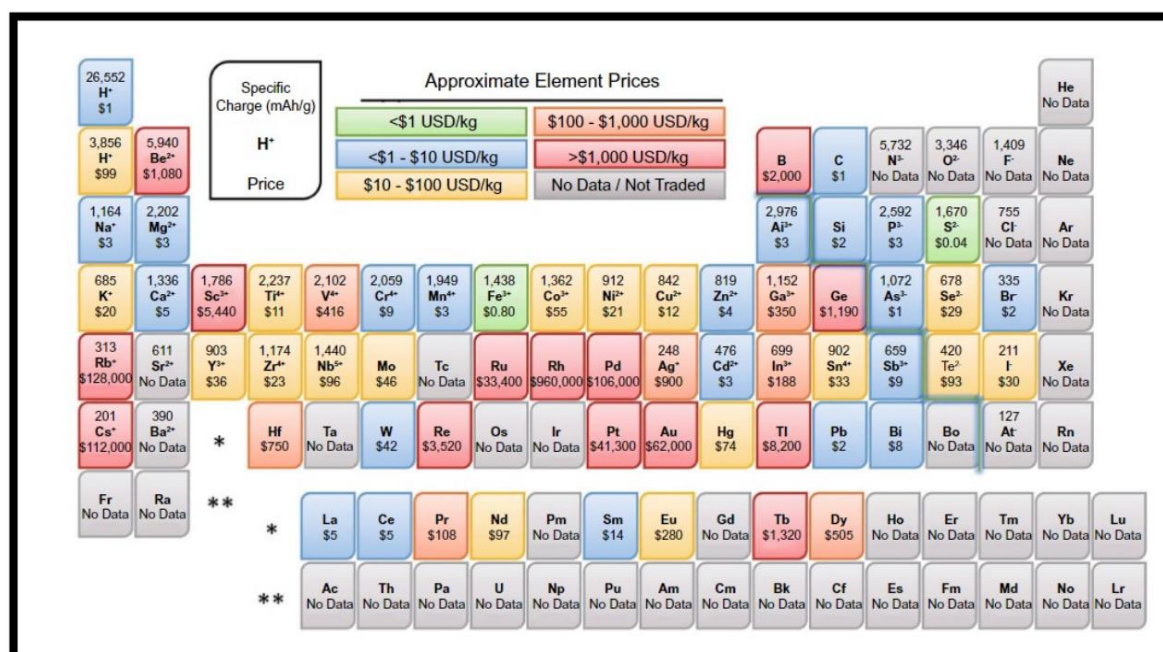


Figure 39. Price of elements in USD/kg and charge capacities of each element at indicated oxidation states. Figure 39 is from an article by Gao *et al.*¹⁰⁸

We can see from Figure 38 that elements Ru, Rh, and Pd are extremely expensive. Although Ru and Rh both show good or at least average electrochemical performance they wouldn't be economically feasible. Using the same logic Tb and B shouldn't be considered as good dopants. V and In are also quite expensive but the reported performances are good. About 95% of rare-earth elements (REEs) are produced in China and this increases supply risks of REEs.¹⁰⁹ REEs like Tb, Pr, Eu, and Dy are also quite expensive as shown in Figure 38. Assuming similar prices for elements Er, Ho, and Gd not listed in Figure 38 leaves only La, Ce, and Sm as reasonable dopants from REEs. This is because La and Ce co-doped material has shown ultra high rate performance and both are quite abundant elements.¹¹⁰ Sm is also quite inexpensive according Figure 38 and has shown good performance making it average dopant. Child labour and supply risks¹ make Co less favorable dopant than the electrochemical performance suggests. European Union (EU) has made a list of critical raw materials (CRMs) in 2020. CRMs are materials with high importance and with high supply risks to EU economy. Some pure elements are included on this list. These are Sb, Co, In, Nb, Ti, V, W, and all REEs.¹¹¹ The average performance, CRM status, and alternative uses of Sb and W make them poor dopants. F has shown good performance as a single dopant and as a co-dopant with V. S and Si are cheap and good performances have been reported.

However, several factors are not considered here. Adding one or more reagents to a synthesis that is already complicated in industrial scale can have many effects. Articles with large scale synthesis were not reviewed. The cyclability and effects on low temperature performance were not discussed in detail. The analysis in the research articles have been made with different systems and electrode preparation processes. Different coatings have been used through the research articles. This affects the measured performance of a material in electrochemical testing. The amount of literature of available for each dopant varies a lot. Some dopants have been studied more in detail and thus better synthesis routes for LFP doped with that singular element could have been found that are not included here. The articles reviewed here may or may not be the best presentations for each dopant's true performance. The price and availability of dopant elements is also under constant change.

With this shallow analysis, acknowledging the shortcomings, dopants are divided into four tiers: green, blue, yellow, and red as shown in Figure 40. Green tier has the best dopants where ultra high performance and economic feasibility are combined. Blue tier combines dopants with high performance and economic feasibility. Yellow tier consist of dopants with mediocre performance. Red tier consist of expensive dopants, dopants with low performance, and dopants with possible supply chain or abundance issues.

1 H																	2 He		
3 Li	4 Be													5 B	6 C	7 N	8 O	9 F	10 Ne
11 Na	12 Mg													13 Al	14 Si	15 P	16 S	17 Cl	18 Ar
19 K	20 Ca	21 Sc	22 Ti	23 V	24 Cr	25 Mn	26 Fe	27 Co	28 Ni	29 Cu	30 Zn	31 Ga	32 Ge	33 As	34 Se	35 Br	36 Kr		
37 Rb	38 Sr	39 Y	40 Zr	41 Nb	42 Mo	43 Tc	44 Ru	45 Rh	46 Pd	47 Ag	48 Cd	49 In	50 Sn	51 Sb	52 Te	53 I	54 Xe		
55 Cs	56 Ba	71 Lu	72 Hf	73 Ta	74 W	75 Re	76 Os	77 Ir	78 Pt	79 Au	80 Hg	81 Tl	82 Pb	83 Bi	84 Po	85 At	86 Rn		
87 Fr	88 Ra	103 Lr	104 Rf	105 Db	106 Sg	107 Bh	108 Hs	109 Mt	110 Ds	111 Rg	112 Cn	113 Nh	114 Fl	115 Mc	116 Lv	117 Ts	118 Og		
		57 La	58 Ce	59 Pr	60 Nd	61 Pm	62 Sm	63 Eu	64 Gd	65 Tb	66 Dy	67 Ho	68 Er	69 Tm	70 Yb				
		89 Ac	90 Th	91 Pa	92 U	93 Np	94 Pu	95 Am	96 Cm	97 Bk	98 Cf	99 Es	100 Fm	101 Md	102 No				

Figure 40. Considering performance and economic factors dopants are coloured with four different colours. Green marks the best dopants, blue good dopants, yellow average dopants, and red worst dopants.

9 SUMMARY

Basics of electrochemical analysis methods CV and EIS were presented. Combining the electrochemical characterization with structural analysis methods like XRD and SEM gives researcher a lot of tools to work with. Particle size, possible impurity phases, particle morphology, lithium diffusion coefficients, electrical conductivity, and resistances associated with different phenomena occurring in the material can all be defined. Understanding the common figures and values given in research articles is essential for study of battery materials and are given in almost any article available. These characterization tools can be applied to LFP but also to all other battery chemistries.

Several synthesis routes can be used to produce pure or doped LFP with high performance. These include carbothermal reduction, sol-gel method, solid state synthesis, and hydrothermal synthesis, to name a few.³⁵

LFP has low electronic and ionic conductivity which affect rate performance negatively during charging and discharging. Using nanosizing, coating, and doping the conductivities and electrochemical performance of LFP can be improved.⁶ As shown by the studies reviewed in Chapter 7, coating and nanosizing of active material particles is almost universally applied. Carbon coating can reduce charge transfer resistance, ensure good electronic contact, and inhibit particle growth. Nanosized particles have larger surface area, shorter diffusion pathways, and lead to a lower charge transfer resistance and increased rate capability.³⁵ Economically feasible dopants with best electrochemical performance were identified in Chapter 8. Top three includes Mn-,¹³ Na-,⁴⁹ and La and Ce co-doped⁶⁵ LFP all with reported ultra high rate performances. Si-,⁵⁶ S-,⁹³ Ti-,⁴¹ V-,⁶⁷ Cr-,⁷⁵ Nb-,⁶¹ In-,⁶² Sn-,⁴⁷ and F and V co-doped⁴² materials have also shown high performance. It seems that the conduction mechanism and the effect of doping to conductivity in LFP is not yet completely understood.⁵⁷ However, doping with right elements can have positive effect on unit cell stability, unit cell volume, band gap, elasticity, lithiation/delithiation voltage,^{54,55} and conduction mechanisms.⁵⁷

10 REFERENCES

1. Lee, S.; Manthiram, A. Can Cobalt Be Eliminated from Lithium-Ion Batteries? *ACS Energy Letters*. American Chemical Society September 9, **2022**, pp 3058–3063. <https://doi.org/10.1021/acsenergylett.2c01553>.
2. Xie, L.; Tang, C.; Bi, Z.; Song, M.; Fan, Y.; Yan, C.; Li, X.; Su, F.; Zhang, Q.; Chen, C. Hard Carbon Anodes for Next-Generation Li-Ion Batteries: Review and Perspective. *Advanced Energy Materials*. John Wiley and Sons Inc October 1, **2021**. <https://doi.org/10.1002/aenm.202101650>.
3. Padhi, A. K.; Nanjundaswamy, K. S.; Goodenough, J. B. *Phospho-olivines as Positive-Electrode Materials for Rechargeable Lithium Batteries*; John Wiley & Sons, Inc, **1997**; Vol. 144.
4. Zhang, W. J. Structure and Performance of LiFePO₄ Cathode Materials: A Review. *Journal of Power Sources*. March 15, 2011, pp 2962–2970. <https://doi.org/10.1016/j.jpowsour.2010.11.113>.
5. Li, M.; Lu, J.; Chen, Z.; Amine, K. 30 Years of Lithium-Ion Batteries. *Advanced Materials*. Wiley-VCH Verlag August 16, **2018**. <https://doi.org/10.1002/adma.201800561>.
6. Chen, S. P.; Lv, D.; Chen, J.; Zhang, Y. H.; Shi, F. N. Review on Defects and Modification Methods of LiFePO₄ Cathode Material for Lithium-Ion Batteries. *Energy and Fuels*. American Chemical Society February 3, 2022, pp 1232–1251. <https://doi.org/10.1021/acs.energyfuels.1c03757>.
7. Linden, D., Reddy, T. B., *Handbook of Batteries*, Third edition.; Eds.; McGraw-Hill Companies, Inc.: USA, **2002**. Pages 1.3 – 1.5, 35.67.
8. Bushkova, O. v.; Yaroslavtseva, T. v.; Dobrovolsky, Y. A. New Lithium Salts in Electrolytes for Lithium-Ion Batteries (Review). *Russian Journal of Electrochemistry*. Maik Nauka Publishing / Springer SBM July 1, **2017**, pp 677–699. <https://doi.org/10.1134/S1023193517070035>.
9. Chernyaev, A.; Partinen, J.; Klemettinen, L.; Wilson, B. P.; Jokilaakso, A.; Lundström, M. The Efficiency of Scrap Cu and Al Current Collector Materials as Reductants in LIB Waste Leaching. *Hydrometallurgy*, **2021**, 203. <https://doi.org/10.1016/j.hydromet.2021.105608>.
10. Liu, Z.; Jiang, Y.; Hu, Q.; Guo, S.; Yu, L.; Li, Q.; Liu, Q.; Hu, X. Safer Lithium-Ion Batteries from the Separator Aspect: Development and Future Perspectives. *Energy and Environmental Materials*. John Wiley and Sons Inc July 1, **2021**, pp 336–362. <https://doi.org/10.1002/eem2.12129>.
11. Murray, V.; Hall, D. S.; Dahn, J. R. A Guide to Full Coin Cell Making for Academic Researchers. *J Electrochem Soc*, **2019**, 166 (2), A329–A333. <https://doi.org/10.1149/2.1171902jes>.
12. Jeon, D. H. Numerical Modeling of Lithium Ion Battery for Predicting Thermal Behavior in a Cylindrical Cell. *Current Applied Physics*, **2014**, 14 (2), 196–205. <https://doi.org/10.1016/j.cap.2013.11.006>.

13. Hu, J.; Jiang, Y.; Cui, S.; Duan, Y.; Liu, T.; Guo, H.; Lin, L.; Lin, Y.; Zheng, J.; Amine, K.; Pan, F. 3D-Printed Cathodes of $\text{LiMn}_{1-x}\text{Fe}_x\text{PO}_4$ Nanocrystals Achieve Both Ultrahigh Rate and High Capacity for Advanced Lithium-Ion Battery. *Adv Energy Mater*, **2016**, 6 (18). <https://doi.org/10.1002/aenm.201600856>.
14. Cavers, H.; Molaiyan, P.; Abdollahifar, M.; Lassi, U.; Kwade, A. Perspectives on Improving the Safety and Sustainability of High Voltage Lithium-Ion Batteries Through the Electrolyte and Separator Region. *Adv Energy Mater*, **2022**, 2200147. <https://doi.org/10.1002/aenm.202200147>.
15. Bard, A. J.; Faulkner, L. R. *Electrochemical Methods, Fundamentals and Applications*, Second edition.; John Wiley & Sons, Inc., **2001**. Pages 2 – 4, 22 – 29, 146, 231, 368 – 386.
16. Murtomäki, L.; Kallio, T.; Lahtinen, R.; Kontturi, K.; *Sähkökemia*, 2nd ed.; Kopijyvä Oy: Jyväskylä, **2010**, pages 15, 46, 63 – 78 , 98.
17. Young, H. D.; Freedman, R. A.; Ford, A. L. *Sears and Zemanskys's University Physics: With Modern Physics*, 13th edition.; Addison-Wesley, **2012**. Pages 177, 193, 754 – 755, 761, 794, 825, 1025 – 1031.
18. Wani, T. A.; Suresh, G. A Comprehensive Review of LiMnPO_4 Based Cathode Materials for Lithium-Ion Batteries: Current Strategies to Improve Its Performance. *Journal of Energy Storage*. Elsevier Ltd December 15, **2021**. <https://doi.org/10.1016/j.est.2021.103307>.
19. Hambley, A. R. *Electronics*, Second edition.; Prentice Hall, Inc.: USA, **2000**. Pages 682 – 683, 757.
20. Warner, J. T. *The Handbook of Lithium-Ion Battery Pack Design: Chemistry, Components, Types and Terminology*, First edition.; Elsevier: Amsterdam, **2015**. Pages 23 – 33.
21. Lin, Y.-X.; Liu, Z.; Leung, K.; Chen, L.-Q.; Lu, P.; Qi, Y. Connecting the Irreversible Capacity Loss in Li Ion Batteries with the Electronic Insulating Properties of Solid Electrolyte Interphase (SEI) Components, *Journal of Power Sources*, 309, March **2016**. pp 221 – 230. ISSN 0378-7753, <https://doi.org/10.1016/j.jpowsour.2016.01.078>.
22. Redondo-Iglesias, E.; Venet, P.; Pelissier, S. Measuring Reversible and Irreversible Capacity Losses on Lithium-Ion Batteries. In *2016 IEEE Vehicle Power and Propulsion Conference, VPPC 2016 - Proceedings*; Institute of Electrical and Electronics Engineers Inc., 2016. <https://doi.org/10.1109/VPPC.2016.7791723>.
23. Skoog, D. A.; Holler, F. J.; Nieman, T. A. *Principles of Instrumental Analysis*, Fifth edition.; Harcourt Brace & Company: USA, **1998**. Pages 569 – 570, 654 – 656.
24. Colburn, A. W.; Levey, K. J.; O'Hare, D.; Macpherson, J. v. Lifting the Lid on the Potentiostat: A Beginner's Guide to Understanding Electrochemical Circuitry and Practical Operation. *Physical Chemistry*

Chemical Physics. Royal Society of Chemistry April 14, 2021, pp 8100–8117. <https://doi.org/10.1039/d1cp00661d>.

25. Xiao, J.; Li, Q.; Bi, Y.; Cai, M.; Dunn, B.; Glossmann, T.; Liu, J.; Osaka, T.; Sugiura, R.; Wu, B.; Yang, J.; Zhang, J. G.; Whittingham, M. S. Understanding and Applying Coulombic Efficiency in Lithium Metal Batteries. *Nat Energy* **2020**, *5* (8), 561–568. <https://doi.org/10.1038/s41560-020-0648-z>.
26. Randviir, E. P.; Banks, C. E. Electrochemical Impedance Spectroscopy: An Overview of Bioanalytical Applications. *Analytical Methods*. March 7, **2013**, pp 1098–1115. <https://doi.org/10.1039/c3ay26476a>.
27. Kissinger, P. T.; Heineman, W. R. *Cyclic Voltammetry*, *Journal of Chemical education*, **60** (9), **1983**, <https://pubs.acs.org/sharingguidelines>.
28. Tran, M. K.; Dacosta, A.; Mevawalla, A.; Panchal, S.; Fowler, M. Comparative Study of Equivalent Circuit Models Performance in Four Common Lithium-Ion Batteries: LFP, NMC, LMO, NCA. *Batteries*, **2021**, *7* (3). <https://doi.org/10.3390/batteries7030051>.
29. Gao, Y.; Xiong, K.; Zhang, H.; Zhu, B. Effect of Ru Doping on the Properties of LiFePO₄/C Cathode Materials for Lithium-Ion Batteries. *ACS Omega*, **2021**, *6* (22), 14122–14129. <https://doi.org/10.1021/acsomega.1c00595>.
30. Cullity, B. D.; Stock, S. R. *Elements of X-Ray Diffraction*, Third edition.; Prentice-Hall, Inc.: USA, **2001**. Pages 31 – 56, 65 – 66, 633 -634.
31. Fanwick, P. E. *Crystallography for Chemists*; Cambridge Scholars Publishing, 1st edition, **2019**. Pages 62 – 70.
32. Th. Hahn, INTERNATIONAL TABLES FOR CRYSTALLOGRAPHY, *Volume A*, Fifth edition, corrected reprint, International Union of Crystallography, Denmark, **2005**, pages 7 – 8, 18, 44, 818 – 822.
33. Zhang, H.; Zou, Z.; Zhang, S.; Liu, J.; Zhong, S. A Review of the Doping Modification of LiFePO₄ as a Cathode Material for Lithium Ion Batteries. *Int J Electrochem Sci* **2020**, *15*, 12041–12067. <https://doi.org/10.20964/2020.12.71>.
34. Zhang, A.; Li, A.; Xia, J.; Shao, Z. Synthesis and Performance of Nb⁵⁺-Doped LiFePO₄/C as Cathode Material in Lithium-Ion Battery. *Int J Electrochem Sci* **2018**, *13* (6), 5243–5252. <https://doi.org/10.20964/2018.06.07>.
35. Satyavani, T. V. S. L.; Srinivas Kumar, A.; Subba Rao, P. S. V. Methods of Synthesis and Performance Improvement of Lithium Iron Phosphate for High Rate Li-Ion Batteries: A Review. *Engineering Science and Technology, an International Journal*. Elsevier B.V. March 1, **2016**, pp 178–188. <https://doi.org/10.1016/j.jestch.2015.06.002>.

36. Srinivasan, V.; Newman, J. Discharge Model for the Lithium Iron-Phosphate Electrode; *The Journal of the Electrochemical Society*, **2004**. <https://escholarship.org/uc/item/7dq154dd>.
37. Malik, R.; Burch, D.; Bazant, M.; Ceder, G. Particle Size Dependence of the Ionic Diffusivity. *Nano Lett*, **2010**, *10* (10), 4123–4127. <https://doi.org/10.1021/nl1023595>.
38. Gardiner, G. R.; Islam, M. S. Anti-Site Defects and Ion Migration in the $\text{LiFe}_{0.5}\text{Mn}_{0.5}\text{PO}_4$ mixed-Metal Cathode Material. *Chemistry of Materials*, **2010**, *22* (3), 1242–1248. <https://doi.org/10.1021/cm902720z>.
39. Wang, J.; Sun, X. Olivine LiFePO_4 : The Remaining Challenges for Future Energy Storage. *Energy and Environmental Science*. Royal Society of Chemistry April 1, **2015**, pp 1110–1138. <https://doi.org/10.1039/c4ee04016c>.
40. Zhang, Q.; Wang, S.; Zhou, Z.; Ma, G.; Jiang, W.; Guo, X.; Zhao, S. Structural and Electrochemical Properties of Nd-Doped LiFePO_4/C Prepared without Using Inert Gas. *Solid State Ion*, **2011**, *191* (1), 40–44. <https://doi.org/10.1016/j.ssi.2011.03.025>.
41. Kim, S.; Mathew, V.; Kang, J.; Gim, J.; Song, J.; Jo, J.; Kim, J. High Rate Capability of LiFePO_4 Cathodes Doped with a High Amount of Ti. *Ceram Int*, **2016**, *42* (6), 7230–7236. <https://doi.org/10.1016/j.ceramint.2016.01.115>.
42. Li, X.; Yu, L.; Cui, Y.; Li, A.; Shao, H.; Shao, Z.; Zhang, W.; Shao, Z. Enhanced Properties of LiFePO_4/C Cathode Materials Co-Doped with V and F Ions via High-Temperature Ball Milling Route. *Int J Hydrogen Energy*, **2019**, *44* (50), 27204–27213. <https://doi.org/10.1016/j.ijhydene.2019.08.187>.
43. Fang, X.; Li, J.; Huang, K.; Liu, S.; Huang, C.; Zhuang, S.; Zhang, J. Synthesis and Electrochemical Properties of K-Doped LiFePO_4/C Composite as Cathode Material for Lithium-Ion Batteries. *Journal of Solid State Electrochemistry*, **2012**, *16* (2), 767–773. <https://doi.org/10.1007/s10008-011-1426-4>.
44. Calderón, C. A.; Thomas, J. E.; Lener, G.; Barraco, D. E.; Visintin, A. Electrochemical Comparison of LiFePO_4 Synthesized by a Solid-State Method Using Either Microwave Heating or a Tube Furnace. *J Appl Electrochem*, **2017**, *47* (10), 1179–1188. <https://doi.org/10.1007/s10800-017-1111-0>.
45. Xiang, W.; Zhong, Y. J.; Ji, J. Y.; Tang, Y.; Shen, H.; Guo, X. D.; Zhong, B. H.; Dou, S. X.; Zhang, Z. Y. Hydrothermal Synthesis, Evolution, and Electrochemical Performance of $\text{LiMn}_{0.5}\text{Fe}_{0.5}\text{PO}_4$ Nanostructures. *Physical Chemistry Chemical Physics*, **2015**, *17* (28), 18629–18637. <https://doi.org/10.1039/c5cp02665b>.
46. Hench, L. L.; West, J. K. *The Sol-Gel Process*; **1990**; *90* (1). <https://doi.org/10.1021/cr00099a003>.

47. Ma, J.; Li, B.; Du, H.; Xu, C.; Kang, F. The Improvement of the High-Rate Charge/Discharge Performances of LiFePO₄ Cathode Material by Sn Doping. *Journal of Solid State Electrochemistry*, **2012**, *16* (1), 1–8. <https://doi.org/10.1007/s10008-010-1263-x>.
48. Liu, L.; Chen, G.; Du, B.; Cui, Y.; Ke, X.; Liu, J.; Guo, Z.; Shi, Z.; Zhang, H.; Chou, S. Nano-Sized Cathode Material LiMn_{0.5}Fe_{0.5}PO₄/C Synthesized via Improved Sol-Gel Routine and Its Magnetic and Electrochemical Properties. *Electrochim Acta*, **2017**, *255*, 205–211. <https://doi.org/10.1016/j.electacta.2017.09.165>.
49. Wang, B.; Wang, Y.; Wu, H.; Yao, L.; Yang, L.; Li, J.; Xiang, M.; Zhang, Y.; Liu, H. Ultrafast and Durable Lithium Storage Enabled by Porous Bowl-Like LiFePO₄/C Composite with Na⁺ Doping. *ChemElectroChem*, **2017**, *4* (5), 1141–1147. <https://doi.org/10.1002/celec.201600854>.
50. He, L. H.; Zhao, Z. W.; Liu, X. H.; Chen, A. L.; Si, X. F. Thermodynamics Analysis of LiFePO₄ Precipitation from Li-Fe(II)-P-H₂O System at 298 K. *Transactions of Nonferrous Metals Society of China (English Edition)*, **2012**, *22* (7), 1766–1770. [https://doi.org/10.1016/S1003-6326\(11\)61385-X](https://doi.org/10.1016/S1003-6326(11)61385-X).
51. Liu, H.; Cao, Q.; Fu, L. J.; Li, C.; Wu, Y. P.; Wu, H. Q. Doping Effects of Zinc on LiFePO₄ Cathode Material for Lithium Ion Batteries. *Electrochem commun*, **2006**, *8* (10), 1553–1557. <https://doi.org/10.1016/j.elecom.2006.07.014>.
52. Altin, S.; Coban, M.; Altundag, S.; Altin, E. Production of Eu-Doped LiFePO₄ by Glass–Ceramic Technique and Investigation of Their Thermal, Structural, Electrochemical Performances. *Journal of Materials Science: Materials in Electronics*, **2022**, *33* (17), 13720–13730. <https://doi.org/10.1007/s10854-022-08305-7>.
53. Hou, Y. K.; Pan, G. L.; Sun, Y. Y.; Gao, X. P. LiMn_{0.8}Fe_{0.2}PO₄/Carbon Nanospheres@Graphene Nanoribbons Prepared by the Biomineralization Process as the Cathode for Lithium-Ion Batteries. *ACS Appl Mater Interfaces*, **2018**, *10* (19), 16500–16510. <https://doi.org/10.1021/acsami.8b02736>.
54. Zhang, B.; Wang, L.; Zhang, H.; Xu, H.; He, X. Revelation of the Transition-metal Doping Mechanism in Lithium Manganese Phosphate for High Performance of Lithium-ion Batteries. *Battery Energy* **2022**, *1* (4), 20220020. <https://doi.org/10.1002/bte2.20220020>.
55. Zhang, B.; He, Y.; Gao, H.; Wang, X.; Liu, J.; Xu, H.; Wang, L.; He, X. Unraveling the Doping Mechanisms in Lithium Iron Phosphate. *Energy Materials*, **2022**, *2* (2), 200013. <https://doi.org/10.20517/energymater.2022.12>.
56. Zhao, J. W.; Zhao, S. X.; Wu, X.; Cheng, H. M.; Nan, C. W. Double Role of Silicon in Improving the Rate Performance of LiFePO₄ cathode Materials. *J Alloys Compd*, **2017**, *699*, 849–855. <https://doi.org/10.1016/j.jallcom.2016.12.430>.

57. Zhang, Y.; Alarco, J. A.; Nerkar, J. Y.; Best, A. S.; Snook, G. A.; Talbot, P. C.; Cowie, B. C. C. Observation of Preferential Cation Doping on the Surface of LiFePO₄ Particles and Its Effect on Properties. *ACS Appl Energy Mater*, **2020**, 3 (9), 9158–9167. <https://doi.org/10.1021/acsaem.0c01536>.
58. Kandhasamy, S.; Nallathamby, K.; Minakshi, M. Role of Structural Defects in Olivine Cathodes. *Progress in Solid State Chemistry*. June **2012**, pp 1–5. <https://doi.org/10.1016/j.progsolidstchem.2012.01.001>.
59. Franchini, C.; Reticcioli, M.; Setvin, M.; Diebold, U. Polarons in Materials. *Nature Reviews Materials*. Nature Research July 1, **2021**, pp 560–586. <https://doi.org/10.1038/s41578-021-00289-w>.
60. Banday, A.; Ali, M.; Pandey, R.; Murugavel, S. Direct Evidence for the Influence of Lithium Ion Vacancies on Polaron Transport in Nanoscale LiFePO₄. *Physical Chemistry Chemical Physics*, **2019**, 21 (19), 9858–9864. <https://doi.org/10.1039/c9cp00408d>.
61. Jiang, A.; Wang, X.; Gao, M.; Wang, J.; Liu, G.; Yu, W.; Zhang, H.; Dong, X. Enhancement of Electrochemical Properties of Niobium-Doped LiFePO₄/C Synthesized by Sol–Gel Method. *Journal of the Chinese Chemical Society*, **2018**, 65 (8), 977–981. <https://doi.org/10.1002/jccs.201700423>.
62. Kumar, A.; Bashiri, P.; Mandal, B. P.; Dhindsa, K. S.; Bazzi, K.; Dixit, A.; Nazri, M.; Zhou, Z.; Garg, V. K.; Oliveira, A. C.; Vaishnav, P. P.; Naik, V. M.; Nazri, G. A.; Naik, R. Optimization of Electrochemical Performance of LiFePO₄/C by Indium Doping and High Temperature Annealing. *Inorganics (Basel)*, **2017**, 5 (4). <https://doi.org/10.3390/inorganics5040067>.
63. Cho, Y. da; Fey, G. T. K.; Kao, H. M. Physical and Electrochemical Properties of La-Doped LiFePO₄/C Composites as Cathode Materials for Lithium-Ion Batteries. In *Journal of Solid State Electrochemistry*; Springer Science and Business Media, LLC, 2008; Vol. 12, pp 815–823. <https://doi.org/10.1007/s10008-007-0498-7>.
64. Gao, L.; Xu, Z.; Zhang, S. The Co-Doping Effects of Zr and Co on Structure and Electrochemical Properties of LiFePO₄ Cathode Materials. *J Alloys Compd*, **2018**, 739, 529–535. <https://doi.org/10.1016/j.jallcom.2017.12.313>.
65. Zhang, B.; Ma, X.; Hou, W.; Yuan, W.; He, L.; Yang, O.; Liu, Y.; Wang, J.; Xu, Y. Revealing the Ultrahigh Rate Performance of the La and Ce Co-Doping LiFePO₄ Composite. *ACS Appl Energy Mater*, **2022**. <https://doi.org/10.1021/acsaem.2c02035>.
66. Liu, Q.; Liu, Z.; Xiao, G.; Liao, S. Enhancement of Capacity at High Charge/Discharge Rate and Cyclic Stability of LiFePO₄/C by Nickel Doping. *Ionics (Kiel)*, **2013**, 19 (3), 445–450. <https://doi.org/10.1007/s11581-012-0775-z>.

67. Jiang, S.; Wang, Y. Synthesis and Characterization of Vanadium-Doped LiFePO_4/C Electrode with Excellent Rate Capability for Lithium-Ion Batteries. *Solid State Ion*, **2019**, 335, 97–102. <https://doi.org/10.1016/j.ssi.2019.03.002>.
68. Yang, Z.; Xia, J.; Zhi, L.; Zhang, W.; Pei, B. An Improved Solid-State Reaction Route to Mg^{2+} -Doped LiFePO_4/C Cathode Material for Li-Ion Battery. *Ionics (Kiel)*, **2014**, 20 (2), 169–174. <https://doi.org/10.1007/s11581-013-0974-2>.
69. Liu, Y.; Qin, W.; Zhang, D.; Feng, L.; Wu, L. Effect of Na^+ in Situ Doping on LiFePO_4/C Cathode Material for Lithium-Ion Batteries. *Progress in Natural Science: Materials International*, **2021**, 31 (1), 14–18. <https://doi.org/10.1016/j.pnsc.2020.10.006>.
70. Fey, G. T. K.; Yan, C. J.; Lin, Y. C.; Huang, K. P.; Cho, Y. da; Wu, P. J.; Sun, Y. sen; Kao, H. M. Calcium Doping Effects on the Electrochemical Properties of LiFePO_4/C Cathode Materials for Lithium-Ion Batteries. In *Advanced Materials Research*; 2012; Vol. 560–561, pp 499–505. <https://doi.org/10.4028/www.scientific.net/AMR.560-561.499>.
71. Wu, S. huang; Chen, M. S.; Chien, C. J.; Fu, Y. P. Preparation and Characterization of Ti^{4+} -Doped LiFePO_4 Cathode Materials for Lithium-Ion Batteries. *J Power Sources*, **2009**, 189 (1), 440–444. <https://doi.org/10.1016/j.jpowsour.2009.01.015>.
72. Wang, G. X.; Bewlay, S.; Yao, J.; Ahn, J. H.; Dou, S. X.; Liu, H. K. Characterization of $\text{LiM}_x\text{Fe}_{1-x}\text{PO}_4$ ($\text{M}=\text{Mg}, \text{Zr}, \text{Ti}$) Cathode Materials Prepared by the Sol-Gel Method. *Electrochemical and Solid-State Letters*, **2004**, 7 (12). <https://doi.org/10.1149/1.1819867>.
73. Gao, Y.; Park, J.; Liang, X. Synergic Titanium Nitride Coating and Titanium Doping by Atomic Layer Deposition for Stable- and High-Performance Li-Ion Battery. *J Electrochem Soc*, **2018**, 165 (16), A3871–A3877. <https://doi.org/10.1149/2.0671816jes>.
74. Chiang, C. Y.; Su, H. C.; Wu, P. J.; Liu, H. J.; Hu, C. W.; Sharma, N.; Peterson, V. K.; Hsieh, H. W.; Lin, Y. F.; Chou, W. C.; Lee, C. H.; Lee, J. F.; Shew, B. Y. Vanadium Substitution of LiFePO_4 Cathode Materials to Enhance the Capacity of LiFePO_4 -Based Lithium-Ion Batteries. *Journal of Physical Chemistry C*, **2012**, 116 (46), 24424–24429. <https://doi.org/10.1021/jp307047w>.
75. Shin, H. C.; Park, S. bin; Jang, H.; Chung, K. Y.; Cho, W. il; Kim, C. S.; Cho, B. W. Rate Performance and Structural Change of Cr-Doped LiFePO_4/C during Cycling. *Electrochim Acta*, **2008**, 53 (27), 7946–7951. <https://doi.org/10.1016/j.electacta.2008.06.005>.
76. Wang, Z. H.; Yuan, L. X.; Wu, M.; Sun, D.; Huang, Y. H. Effects of Na^+ and Cl^- Co-Doping on Electrochemical Performance in LiFePO_4/C . *Electrochim Acta*, **2011**, 56 (24), 8477–8483. <https://doi.org/10.1016/j.electacta.2011.07.018>.

77. Yang, L.; Deng, W.; Xu, W.; Tian, Y.; Wang, A.; Wang, B.; Zou, G.; Hou, H.; Deng, W.; Ji, X. Olivine $\text{LiMn}_{x}\text{Fe}_{1-x}\text{PO}_4$ cathode Materials for Lithium Ion Batteries: Restricted Factors of Rate Performances. *Journal of Materials Chemistry A*. Royal Society of Chemistry July 7, **2021**, pp 14214–14232. <https://doi.org/10.1039/d1ta01526e>.
78. Gupta, R.; Saha, S.; Tomar, M.; Sachdev, V. K.; Gupta, V. Effect of Manganese Doping on Conduction in Olivine LiFePO_4 . *Journal of Materials Science: Materials in Electronics*, **2017**, 28 (7), 5192–5199. <https://doi.org/10.1007/s10854-016-6175-9>.
79. Sreedeeep, S.; Natarajan, S.; Aravindan, V. Recent Advancements in LiCoPO_4 Cathodes Using Electrolyte Additives. *Current Opinion in Electrochemistry*. Elsevier B.V. February 1, **2022**. <https://doi.org/10.1016/j.coelec.2021.100868>.
80. Gao, H.; Jiao, L.; Yang, J.; Qi, Z.; Wang, Y.; Yuan, H. High Rate Capability of Co-Doped LiFePO_4/C . *Electrochim Acta*, **2013**, 97, 143–149. <https://doi.org/10.1016/j.electacta.2013.02.132>.
81. Örneek, A.; Bulut, E.; Can, M.; Özacar, M. Characteristics of Nanosized $\text{LiNi}_x\text{Fe}_{1-x}\text{PO}_4/\text{C}$ ($x=0.00-0.20$) Composite Material Prepared via Sol-Gel-Assisted Carbothermal Reduction Method. *Journal of Solid State Electrochemistry*, **2013**, 17 (12), 3101–3107. <https://doi.org/10.1007/s10008-013-2201-5>.
82. Chang, Z. R.; Lv, H. J.; Tang, H.; Yuan, X. Z.; Wang, H. Synthesis and Performance of High Tap Density LiFePO_4/C Cathode Materials Doped with Copper Ions. *J Alloys Compd*, **2010**, 501 (1), 14–17. <https://doi.org/10.1016/j.jallcom.2010.04.112>.
83. Yiming, W.; Giuli, G.; Moretti, A.; Nobili, F.; Fehr, K. T.; Paris, E.; Marassi, R. Synthesis and Characterization of Zn-Doped LiFePO_4 Cathode Materials for Li-Ion Battery. *Mater Chem Phys*, **2015**, 155, 191–204. <https://doi.org/10.1016/j.matchemphys.2015.02.023>.
84. Ma, Z.; Shao, G.; Wang, G.; Du, J.; Zhang, Y. Electrochemical Performance of Mo-Doped LiFePO_4/C Composites Prepared by Two-Step Solid-State Reaction. *Ionics (Kiel)*, **2013**, 19 (3), 437–443. <https://doi.org/10.1007/s11581-012-0768-y>.
85. Gao, Y.; Li, L.; Peng, H.; Wei, Z. Surfactant-Assisted Sol-Gel Synthesis of Nanostructured Ruthenium-Doped Lithium Iron Phosphate as a Cathode for Lithium-Ion Batteries. *ChemElectroChem*, **2014**, 1 (12), 2146–2152. <https://doi.org/10.1002/celec.201402247>.
86. Tong, D. G.; Luo, F. L.; Chu, W.; Li, Y. L.; Wu, P. Effect of Rhodium Substitution on the Electrochemical Performance of LiFePO_4/C . *Mater Chem Phys*, **2010**, 124 (1), 1–5. <https://doi.org/10.1016/j.matchemphys.2010.05.030>.
87. Talebi-Esfandarani, M.; Savadogo, O. Effects of Palladium Doping on the Structure and Electrochemical Properties of LiFePO_4/C Prepared Using the Sol-Gel Method. *Journal of New Materials for Electrochemical*

88. Arava, H.; Fang, H.; Zhang, L. L.; Hill, J. W.; Liang, G. Electrochemical Studies of Carbon Coated LiFePO₄ Doped with Tungsten. In *Proceedings of the IEEE Conference on Nanotechnology*; **2013**; pp 1050–1053. <https://doi.org/10.1109/NANO.2013.6720943>.
89. Kulka, A.; Braun, A.; Huang, T. W.; Wolska, A.; Klepka, M. T.; Szewczyk, A.; Baster, D.; Zając, W.; Wierczek, K.; Molenda, J. Evidence for Al Doping in Lithium Sublattice of LiFePO₄. *Solid State Ion* **2015**, *270*, 33–38. <https://doi.org/10.1016/j.ssi.2014.12.004>.
90. Hou, L.; Tao, G. A First-Principles Study of Bulk and Surface Sn-Doped LiFePO₄: The Role of Intermediate Valence Component in the Multivalent Doping. *Phys Status Solidi B Basic Res*, **2017**, *254* (10). <https://doi.org/10.1002/pssb.201700041>.
91. Li, Y.; Wang, L.; Liang, F.; Yao, Y.; Zhang, K. Enhancing High Rate Performance and Cyclability of LiFePO₄ Cathode Materials for Lithium Ion Batteries by Boron Doping. *J Alloys Compd*, **2021**, *880*. <https://doi.org/10.1016/j.jallcom.2021.160560>.
92. Fey, G. T. K.; Huang, K. P.; Peng, P. Y.; Lin, Y. C.; Cho, Y. D.; Kao, H. M. Effect of Antimony Doping on the Properties of a Green Energy Cathode Material LiFePO₄ for Lithium Ion Batteries. *Adv Mat Res*, **2013**, *742*, 152–157.
93. Okada, K.; Kimura, I.; Machida, K. High Rate Capability by Sulfur-Doping into LiFePO₄ Matrix. *RSC Adv*, **2018**, *8* (11), 5848–5853. <https://doi.org/10.1039/c7ra12740e>.
94. Radhamani, A. v.; Karthik, C.; Ubig, R.; Ramachandra Rao, M. S.; Sudakar, C. Suppression of FeLi• Antisite Defects in Fluorine-Doped LiFePO₄. *Scr Mater* **2013**, *69* (1), 96–99. <https://doi.org/10.1016/j.scriptamat.2013.02.015>.
95. Meng, Y.; Li, Y.; Xia, J.; Hu, Q.; Ke, X.; Ren, G.; Zhu, F. F-Doped LiFePO₄ @N/B/F-Doped Carbon as High Performance Cathode Materials for Li-Ion Batteries. *Appl Surf Sci*, **2019**, *476*, 761–768. <https://doi.org/10.1016/j.apsusc.2019.01.139>.
96. Liu, H.; Luo, S. hua; Yan, S. xue; Wang, Y. feng; Wang, Q.; Li, M. qi; Zhang, Y. hui. A Novel and Low-Cost Iron Source for Synthesizing Cl-Doped LiFePO₄/C Cathode Materials for Lithium-Ion Batteries. *Journal of Electroanalytical Chemistry*, **2019**, *850*. <https://doi.org/10.1016/j.jelechem.2019.113434>.
97. Zheng, J.; Yong, H. H.; Yang, W. Z. Synthesis and Characterization of LiFe(PO₄)(3–x)/3Brx/C as a Cathode Material for Lithium-Ion Battery. *Sci China Technol Sci*, **2015**, *58* (7), 1294–1298. <https://doi.org/10.1007/s11431-015-5809-0>.
98. Herrera, F.; Fuenzalida, F.; Marquez, P.; Gautier, J. L. Improvement of the Electrochemical Performance of LiFePO₄ Cathode by Y-Doping.

MRS Commun, **2017**, 7 (3), 515–522.
<https://doi.org/10.1557/mrc.2017.71>.

99. Yanwen, T.; Kang, X.; Liu, L.; Chaoqing, X. U.; Tao, Q. U. *Research on Cathode Material of Li-Ion Battery by Yttrium Doping*; **2008**; 26 (1).
[https://doi.org/10.1016/S1002-0721\(08\)60081-2](https://doi.org/10.1016/S1002-0721(08)60081-2).
100. Zhao, N.; Li, Y.; Zhi, X.; Wang, L.; Zhao, X.; Wang, Y.; Liang, G. Effect of Ce³⁺ Doping on the Properties of LiFePO₄ Cathode Material. *Journal of Rare Earths*, **2016**, 34 (2), 174–180. [https://doi.org/10.1016/S1002-0721\(16\)60011-X](https://doi.org/10.1016/S1002-0721(16)60011-X).
101. Meng, X.; Han, B.; Wang, Y.; Nan, J. Effects of Samarium Doping on the Electrochemical Performance of LiFePO₄/C Cathode Material for Lithium-Ion Batteries. *Ceram Int*, **2016**, 42 (2), 2599–2604.
<https://doi.org/10.1016/j.ceramint.2015.10.063>.
102. Pang, L.; Zhao, M.; Zhao, X.; Chai, Y. Preparation and Electrochemical Performance of Gd-Doped LiFePO₄/C Composites. *J Power Sources*, **2012**, 201, 253–258. <https://doi.org/10.1016/j.jpowsour.2011.10.096>.
103. Göktepe, H. Effect of Dy³⁺-Doping on Electrochemical Properties of LiFePO₄/C Cathode for Lithium-Ion Batteries. *Journal of the Chinese Chemical Society*, **2013**, 60 (2), 218–222.
<https://doi.org/10.1002/jccs.201200266>.
104. Altin, S.; Yolun, A. Fabrication and Electrochemical Performance of Ho-Substituted C/LiFePO₄: Improved Battery Performance. *Journal of Materials Science: Materials in Electronics*, **2021**, 32 (16), 21568–21578. <https://doi.org/10.1007/s10854-021-06665-0>.
105. Göktepe, H.; Sahan, H.; Ülgen, A.; Patat, Ş. Synthesis and Electrochemical Properties of Carbon-Mixed LiEr_{0.02}Fe_{0.98}PO₄ Cathode Material for Lithium-Ion Batteries. *J Mater Sci Technol*, **2011**, 27 (9), 861–864. [https://doi.org/10.1016/S1005-0302\(11\)60156-4](https://doi.org/10.1016/S1005-0302(11)60156-4).
106. Göktepe, H. Electrochemical Performance of Yb-Doped LiFePO₄/C Composites as Cathode Materials for Lithium-Ion Batteries. *Research on Chemical Intermediates*, **2013**, 39 (7), 2979–2987.
<https://doi.org/10.1007/s11164-012-0811-7>.
107. Tian, Z.; Zhou, Z.; Liu, S.; Ye, F.; Yao, S. Enhanced Properties of Olivine LiFePO₄/Graphene Co-Doped with Nb⁵⁺ and Ti⁴⁺ by a Sol-Gel Method. *Solid State Ion*, **2015**, 278, 186–191.
<https://doi.org/10.1016/j.ssi.2015.06.017>.
108. Gao, Y.; Pan, Z.; Sun, J.; Liu, Z.; Wang, J. High-Energy Batteries: Beyond Lithium-Ion and Their Long Road to Commercialisation. *Nano-Micro Letters*. Springer Science and Business Media B.V. December 1, **2022**. <https://doi.org/10.1007/s40820-022-00844-2>.
109. Binnemans, K.; Peter, •; Jones, T.; Torsten, •; Ller, M.; Yurramendi, L. Rare Earths and the Balance Problem: How to Deal with Changing Markets? **2018**. <https://doi.org/10.1007/s40831-018-0162-8>.

110. Yaroshevsky, A. A. Abundances of Chemical Elements in the Earth's Crust. *Geochemistry International*, **2006**, 44 (1), 48–55. <https://doi.org/10.1134/S001670290601006X>.
111. European Comission, *Critical raw materials*. , https://single-market-economy.ec.europa.eu/sectors/raw-materials/areas-specific-interest/critical-raw-materials_en (Accessed 18.01.2022)